Effects of Size and Coalescence on the Interfacial Dynamics of Nanoparticles: A Molecular Dynamics Study

by

Ying Yang

A thesis submitted in partial fulfillment of the requirements for the degree of

Doctor of Philosophy

in

Materials Engineering

Department of Chemical and Materials Engineering
University of Alberta

Abstract

Normally chemically inert materials such as Au have been found to be catalytically active in the form of particles whose size is about 1 nm. Direct and indirect observations of various types of metal nanoparticles (NPs) in this size range, under catalytically relevant conditions for fuel-cell operation and catalysis, have indicated that such ‘small’ particles can exhibit large spontaneous shape fluctuations and significant changes in shape and chemical activity in response to alterations in environmental conditions. NPs also normally exhibit facile coalescence when in proximity, and these agglomations impact their stability and reactivity in applications. Our molecular dynamics simulations first focus on Ni nanoparticles, a commonly used NP in catalytic applications and carbon nanotube growth, in the ≈ 1 nm size regime where large scale shape fluctuations have been observed experimentally. An analysis of the large scale shape fluctuations observed in our simulations of these ‘small’ NPs indicates that they are accompanied by collective migration motion of Ni atoms through the NP center and we quantify these dynamic structures and their impact on NP shape. In contrast, string-like collective atomic motion is confined to the NP interfacial region of NPs having a diameter greater than a few nm and, correspondingly, the overall NP shape remains roughly spherical, a case studied in our prior Ni NP simulations. Evidently, the large spontaneous NP shape fluctuations reflect a change in character of the collective atomic dynamics when the NPs become critically small in size. Meanwhile, we are aimed to investigate the NP sintering and coalescence phenomenon quantitatively to determine the string-like collective motions in the coalescence of ultra-small NPs and the crystallization process to form the crystalline nanoparticles. We identify the string-like collective motions accompany the evolvements of the local fcc structure, the local icosahedral structure and the liquid-like structure as well as the crystallization process, rather than the rotations of the NPs, in the coalescence of the multiple ultra-small NPs. The recognition of this phenomenon would help us understand the early stages of crystal growth and structural rearrangement of the relatively disordered ‘amorphous’ pre-nucleation clusters. Finally, we explore the NP behavior under the constraint of the graphene substrate as the supporting material. The results show that NP affected by the substrate has lower ratio of the local fcc structure than the single free NP, indicating that the substrate makes the NP more disordered and more active.

Preface

Some of the research conducted for this thesis is a part of an international research collaboration, led by Professor H. Zhang at the University of Alberta and Dr. J. Douglas at the NIST.

Chapter 3 of this thesis has been published as Y. Yang, H. Zhang and J. Douglas, "Origin and Nature of Spontaneous Shape Fluctuations in 'Small' Nanoparticles," *ACS Nano*, **8**, 7465-7477 (2014), where Dr. Zhang and Dr. Douglas both initiated the research, and I conducted the simulation, analyzed the data and wrote the manuscript. All other parts of this thesis are my original work.

Acknowledgements

When I start in school, in University of Alberta, this day seems so far away. Now it's here and I can't believe that time has passed so quickly.

First of all, I would like to express my great appreciation to my supervisor and career mentor Professor Hao Zhang. His profound knowledge and understanding of computational materials science especially Molecular Dynamics simulation has left a long-lasting impression on me and have helped me establish my own way of research. Thank Professor for having been insisting on meeting with me in English. I make sure that every time I challenge myself I try my best just to prove those winter's early morning meetings did me some good. My supervisor inspires, motivates, appreciates and loves the students – all of the above are not exaggerated compliments. I do have received the best education personally.

I would like to thank Drs. Natalia Semagina and Hongbo Zeng for sparing the time meeting with me. They have provided constructive suggestions on my first research topic of the interfacial dynamics for single nanoparticles.

I'm grateful to the professors whose courses I have taken. They are Drs. Dongyang Li, Tian Tang, Patricio F. Mendez, Thomas H. Etsell and Weixing Chen. I'm also grateful to the professors who care my study and research program here in Edmonton. They are Drs. Lianmeng Zhang, Qiang Shen, Chuanbin Wang and Fei Chen. The professors above have encountered my fluctuations and witnessed my growth during this four-year program.

I appreciate the help from the group members, Mr. Wenbo Xie, Ms. Arina Marchenko, Ms. Di Zhu, Mr. Yves Lai, Mr. Mohammad Khalkhali, Mr. Xuhang Tong, Mr. Xiao Xing, Ms. Min Wu and Mr. Bin Liu. The discussions with them are effective and enjoyable.

Apart from the study and research, on the personal level I'm much obliged to Ms. Lu Zheng. She has shared her life experience with me, lent and recommended books to me and introduced me to her friends and community, which help me to go through the ups and downs in life. Blessed is she.

It's hard to overstate the gratitude I feel for falling in love with Mr. Good Enough. Lest I forget that he has a beautiful personality; he makes me happy and talking to him makes my day. I think of him with respect and a lot of admiration, and am deeply grateful to him, not only for my learning from his greater judgement and knowledge of the world, but for his constantly enlightening me to help me discover my own potential and self-confidence. I would like to thank him and my entire family to help make this thesis a reality.

Last but not the least, the assistance provided by the examining committee is sincerely appreciated.

Indeed it's hard to bid goodbye, however saying farewell can also be bittersweet – that's why people call it commencement.

Table of Contents

List of Tables

List of Figures

1 Introduction

Ultra-small nanoparticles (NPs), which own high specific surface area and quantum size effect, have been playing an important role in the chemical industries, energy generations and environmental protections. Enormous efforts have been made to develop novel nanoparticle catalysts, for instance, and to explore the relationship between their structures and properties. The high interfacial mobility of the NPs, also called clusters, may be the key to the understanding of nanoparticle catalysis.

1.1 Spontaneous Shape Fluctuations in Single Small Nanoparticle

Nanoparticles (NPs) undergoing spontaneous shape fluctuations have been the focus of numerous recent experimental studies. Most of these observations come from the metallic NPs having relevance for catalysis applications such as Au,[1-4] Bi[5, 6], Pd[7], Pt[8, 9] Cu[10] and Ni.[11] For example, the colloidal Au nanoparticles[2] with the size of 6 nm shows surprisingly high catalytic activities for room temperature CO oxidation pertaining to the large surface heterogeneity. Marchak *et al.*[5] observed spontaneous NP shape fluctuations in individual Bi NPs and the associated NP property (band gap) fluctuations. Helveg *et al.*[11] investigated the surface reorganization of Ni NPs in the course of their observations on carbon nanotube growth catalyzed by these NPs. Continuous shape change of Au NPs having a radius of about 1 nm have been recorded by irradiation characterization using an incident electron beam[1]. Large shape changes have also been found in Pd NPs during CO/NO cycling of the environment around these NPs.[7]

1.1.1 Surface Melting of Nanoparticles

The observed sensitivity of NPs to their environment (e.g., hydrostatic pressure, alloying with other metals, the presence of solvents or even illumination) correlates with their high interfacial atomic mobility. The intuitive concepts of 'surface melting'[12] and 'quasi-liquid layer'[13, 14] have often been invoked to rationalize this phenomenon.

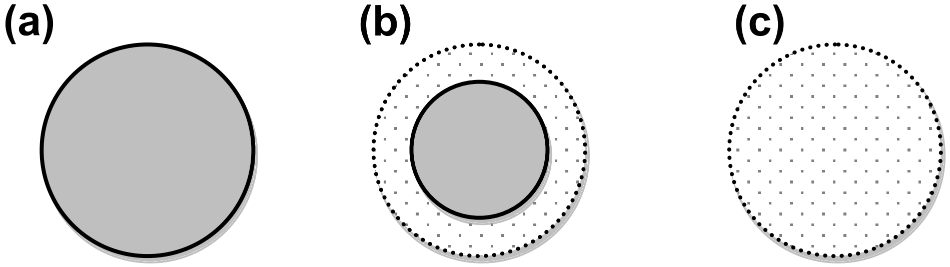

Figure 1.1 The three configurations demonstrating the melting process of nanoparticles: (a) solid particle, (b) solid particle with a surface-melted layer and (c) liquid particle.

Surface melting of NPs describes the situation that even far below the bulk melting point, some of the surface and interfacial atoms becomes randomly disordered, forming a liquid-like layer (or shell if the particle shape is spherical), while the core atoms are packed orderly as the perfect bulk crystal lattice. With the increment of the temperature, the melting of the NPs starts to take place. Generally, a liquid layer emerges on the surface and grows gradually. Figure 1.1 depicts the liquid phase formation and sequential growth till being fully melt.

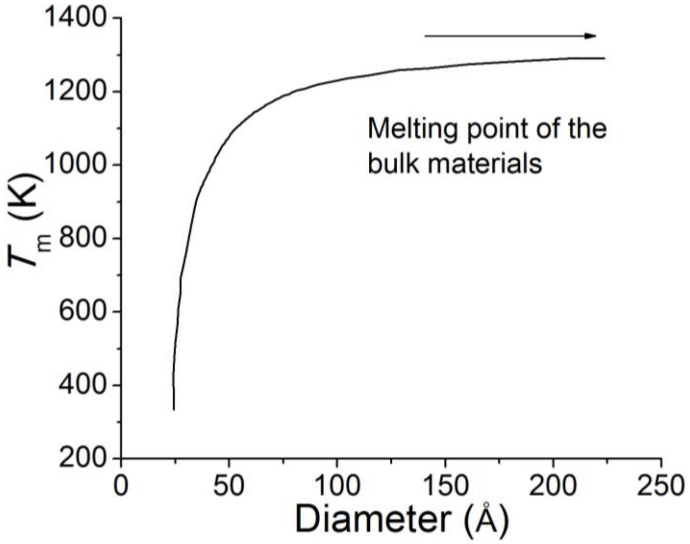

Figure 1.2 Melting curve for Au as a function of nanoparticle diameter by means of scanning electron diffraction method. Reprinted figure with permission from reference[15] as follows: P. Buffat and J. P. Borel, *Phys. Rev. A*, **13**, 2287-2298 (1976). Copyright 1976 by the American Physical Society.

Many researchers have carried out both experimental and theoretical studies to reveal that the melting temperature of NPs is strongly size-dependent. According to the Gibbs-Thomson equation, for an isolated spherical solid particle in its own liquid, the shifted melting point ΔT_m is proportional to $1/r$, where r is the radius of the particle, or $\Delta T_m \equiv T_m\ (N \rightarrow \infty) - T_m\ (N) \sim N^{-1/3}$, and N is the atoms number. Melting temperature depressing occurs for most of the cases, an example[15] seen in Figure 1.2, especially for small particles whose radius is less than 10 nm. Despite of the general tendency, a few exceptions still exist[16, 17], with the melting point above that of the bulk materials due to the completely different structure of the nanoscale, called “too small to melt”.

1.1.2 Experimental and Computational Research Work

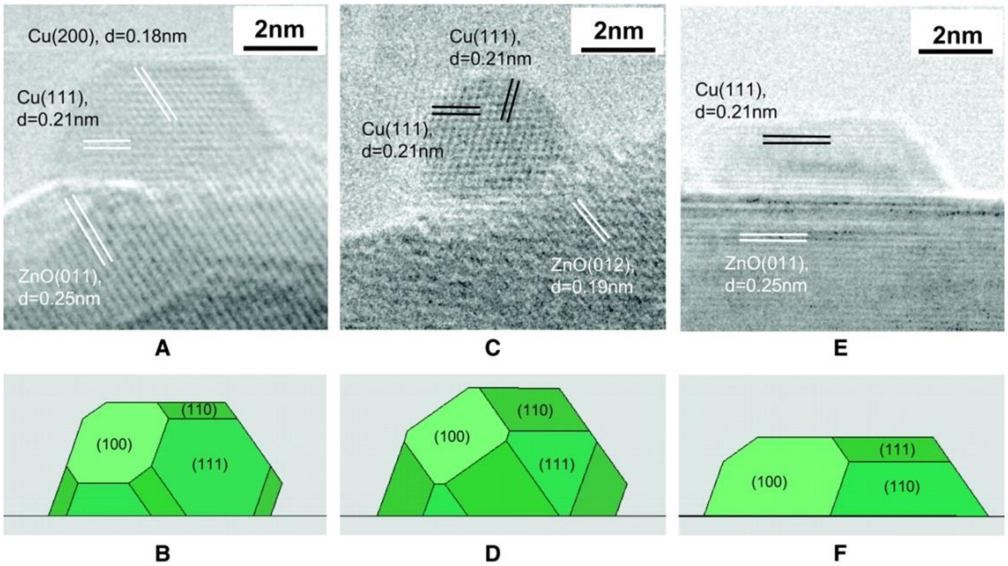

Figure 1.3 The dynamic shape changes for Cu NP in response of the different gas environment[10]. Reprinted with permission from AAAS (American Association for the Advancement of Science).

Preparations and characterizations of nanoparticles develop gradually with the advancement of the technology, providing opportunities to investigate the surface melting of nanoparticles experimentally. Various types of materials have been investigated, e.g.

Pb[18, 19], Sn[18, 20], Bi[18, 21], Ag[22], Cu[22], Al[23, 24], Ge[22] and In[19, 25, 26], by using the electron diffraction, *in situ* TEM, scanning nanocalorimeter, etc. to simultaneously obtain their microstructures and melting temperatures of the nanoparticles or clusters. The microstructures can be sensitive to the environmental conditions. For example, surface melting was visible for Sn clusters on SiO_2 using dark filed TEM technology[25]; Pb crystal structure fluctuation[27] was documented via high resolution electron microscopy. Figure 1.3 shows the dynamic shape changes of Cu NPs in response of the different gas environment. These NPs were used as the catalysts for the methanol synthesis and hydrocarbon conversion processes for fuel cells[10].

For most of the cases, the melting temperature is approximately inversely proportional to the particle radius r, which obeys the Gibbs-Thomson rule. These experimental results, with the materials, methods and some brief descriptions, are summarized in Table 1.1.

Table 1.1 A summary of experimental results for the size-dependent melting of nanoparticles[28], where the abbreviations are listed as ED (electron diffraction), TEM (transmission electron microscopy), STM (scanning tunneling microscopy), XRD (X-ray diffraction), SAED (selected area electron diffraction) and DSC (differential scanning calorimetry)

Metal particle	Synthesis method	Determination of particle size	Measurement of melting	Size (nm)	Description
Pb, Sn, Bi[18]	Evaporation	Particle size = the film thickness	ED	1 ~ 100	Melting point (m.p.) decreases with reducing particle radius (*r*)
Ag, Cu, Al, Ge[22]	Evaporation	-	ED	1 ~ 30	Abnormally large m.p. depression
Sn[20]	Evaporation	Electron micrograph, modified	ED	-	m.p. decreases nolinearly with 1/*r*
In, Pb[19]	Evaporation	Electron micrograph	ED	3 ~ 50	m.p. decreases with reducing particle size
In[26]	Evaporation	SAED	SAED	5 ~ 10	m.p. of individual In particle
Pb, Bi[21]	*In situ* evaporation	*In situ* TEM	Change of particle shape	30 ~60	m.p. vs *r* follows the melt skin model
Sn, In, Pb, Bi[29]	*In situ* evaporation	TEM micrograph	Dark field image	3 ~ 50	Near linear relationship of m.p. vs 1/*r*
In[25]	Self-essembled	STM	STM	5 ~ 100	Reduced slope for m.p. depression due to crystal shape
Sn[30]	Evaporation	Scanning nanocalorimeter	Scanning nanocalorimeter	5 ~ 50	m.p. vs *r* follows the liquid skin model; reduced latent heat with decreasing *r*
Pb[31]	Evaporation	*In situ* XRD	*In situ* XRD	about 50	The thickness of liquid skin is measured
Al[24]	Mechanical attrition; evaporation	TEM; XRD	DSC	-	m.p. decreases linearly with 1/*r*
Sn with carbon[32]	Evaporation	TEM micrograph	*In situ* TEM	10 ~ 60	Elevated m.p. relative to free particle due to pressure effect of the matrix
Sn/SiO_2[33]	Sputtering	TEM	DSC	10 ~ 200	m.p. lowering with decreased *r*
In, Sn, Bi, Cd, Pb/Al[34]	Ball-milling	TEM micrograph	DSC	-	Linear dependence of m.p. and latent heat with 1/*r*
Pb/Al_2O_3, SiO_2[35]	Sol-gel	XRD	DSC	-	m.p. lowering by 3-5 K for *r* ~ 10 nm
Sn, Pb, Ga[36]	Evaporation	*In situ* time-resolved TEM	*In situ* time-resolved TEM	-	Direct observation of liquid skin

Nonetheless, these *in situ* techniques have their own limitations. For instance, it is a difficult task to observe and understand how the surface atoms rearrange to yield the so-called ‘liquid layer’ via simply performing characterization measurements. Thus, the computational simulation becomes vital in terms of expoloring the properties of NPs from the atomic aspects. Figure 1.4 provides surface melting of Ni nanoclusters with the increasing of the temperature[37] using Molecular Dynamics simulation. The melting is determined, roughly or precisely, by a sharp change of potential energy or the root mean square displacement (MSD) fluctuation (which is related to the Lindemann index) with respect to temperature. Particle shape and the local structure change attract much attention and it is generally accepted[38, 39] that the icosahedron is favored at small sizes for different materials (like Ag, Cu and Ni) while FCC is expected for larger sizes. These computational results, with the materials, analytical methods, sizes and some descriptions, are summarized in Table 1.2.

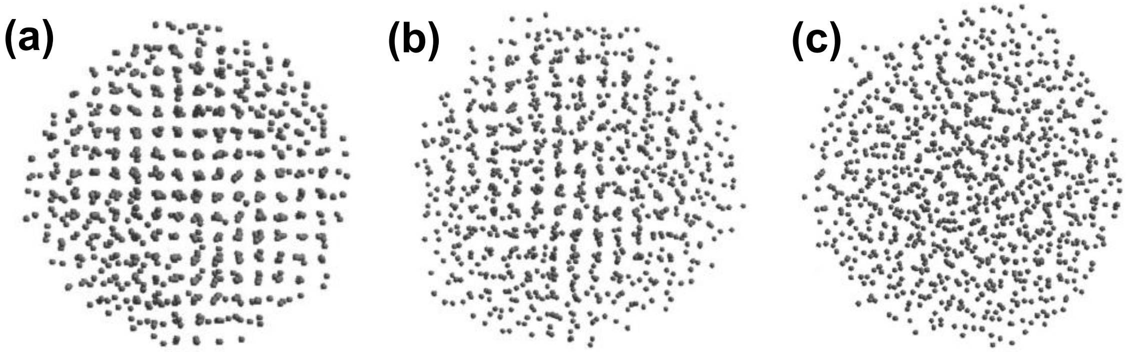

Figure 1.4 (a) The starting of surface melting of Ni_{1004} at 1000 K with a outlayer liquid skin, (b) at 1140 K with ordered inner core and (c) entirely melted cluster at 1180 K. Reprinted with permission from reference[37]. Copyright 2001, AIP Publishing LLC.

Table 1.2 A summary of computational results for the surface melting of nanoparticles, where the abbreviations and nomenclatures are listed as SC (Sutton-Chen), LJ (Lennard-Jones), EAM (embedded atom method), MC (Monte Carlo), RMSD (root mean square displacement), RDF (radial distribution function), CNA (common neighbor analysis), *Cp* (heat capacity), *U* (potential energy), *D* (diffusion constant), k_B (Boltzmann constant)

Nanoparticle	Simulation method and potential	Analytical method	Size	Description
Ni[37]	MD; Quantum SC	*Cp* (*T*),*U* (*T*), RMSD, Honeycutt–Andersen index	5.74 nm diameter	M.p. decreases linearly with $N^{-1/3}$
Al_N [40]	Microcanonical MD; *glue* potential	*Cp* (*T*),*U* (*T*), volume, RMSD	$N = 13$, 43, 55, 147	I_h-like structure is mostly favored except for Al_{43} as a glass cluster
Ar_N, Cu_{55} [41]	MD; LJ for Ar, EAM for Cu	Layer-by-layer MSD, *D*, free energy, density	$N = 40$ ~ 147	Collective motion of surface atoms is accompanied by ''floaters''
V[42]	MD; modified analytic EAM	RDF, mean atomic energy, radial mean square vibration amplitude	2 ~ 9 nm diameter	Firstly premelting and then an abrupt overall melting of the whole cluster
Au[43]	MD; Quantum SC	Bond-orientational order parameter	1.22 ~ 4.49 nm diameter	Complete surface premelting is size dependent and is not observed in very small nanoparticles
Al[44]	MD; EAM	*U* (*T*) and Lindemann index	$N = 55$ ~ 1000	M.p. is $1/r$ and $N^{-1/3}$ dependent
Au_N[45]	MD; EAM	*U* (*T*), *D*, CNA	$N = 75$, 146, 459	Structural transformations are precursors to the melting transitions below bulk m.p.
Na_N, Na^+_N [46]	MC improved by q-jumping method, MD	$C(T) / Nk_B$, Lindemann index, MSD	$N = 8$ ~ 139	Premelting is induced by diffusion processes
Fe[47]	Isothermal MD; tight binding model	Lindemann index	$N = 586$	The width of the surface molten layer increases with increasing temperature.

1.2 Coalescence of Multiple Small Nanoparticles

The ability to predict and control the size and structure of nanoparticles is of great importance for applications, as the arrangement of atoms, the diffusion and coalescence is the key determinant of the optical, electronic, and thermal properties of the nanoparticles, in the systems of the aerosols, colloids and thin film epitaxial growth. For example, the coarsening of island-like deposits has been extensively studied which is a critical step during the thin film deposition and other applications[48-50]. During this process, the diffusion and coalescence of atoms and clusters plays an important role in controlling the island sizes, which in turn affects the properties of the film.

Similarly, the studies of multiple NPs interactions also involves both experimental and computational methods. The high-resolution electron microscopic analysis, e.g., *in situ* TEM, is a typical technique that has been employed to characterize the coalescence of various metallic nanoparticles including Au[51, 52], Au-Pd, Pd[52], Ni[53] and Bi[54]. The 'surface melting' phenomenon has also been reported to play an essential role for this coalescence process. For example, José-Yacaman *et al.*[52] observed a clear surface "liquid layer" shell and the well-ordered cores when NPs merged. Analogous results showing the "surface layers" mobile character were also documented[53, 54].

In addition to the experimental examinations, computational studies have also been applied to investigate the surface melting and the structure transformation during the NP coalescence. In fact, there have been many reports using simulations focusing on NPs of Au[55-57], Fe[58], Ag[59, 60], Cu-Ni[61], Fe-Ni[62], Pd[63], Pb[64], Cu[65], Ta[66]and W[67]. The premelting was vital especially in the early sintering/coalescence stage[57] and the ordered faceting prohibits the coalescence to become slower than expected from the macroscopic theory[56]. Besides, the identical methodology was also extended to the studies of TiO_2[68, 69], ZrO_2, Al_2O_3[70] and LJ particles[71, 72]. Koparde *et al.*[68, 69, 73] has made extensive efforts to study the phase transformation during the NP sintering confirmeing that, the liquid-like structure facilitates the quick initial sintering-neck formation. And after the complete coalescence, the heat is released by recrystallization. Figure 1.5 shows the example of the result for constant-energy MD simulation of the coalescence of two nanoscale Pb clusters[64].

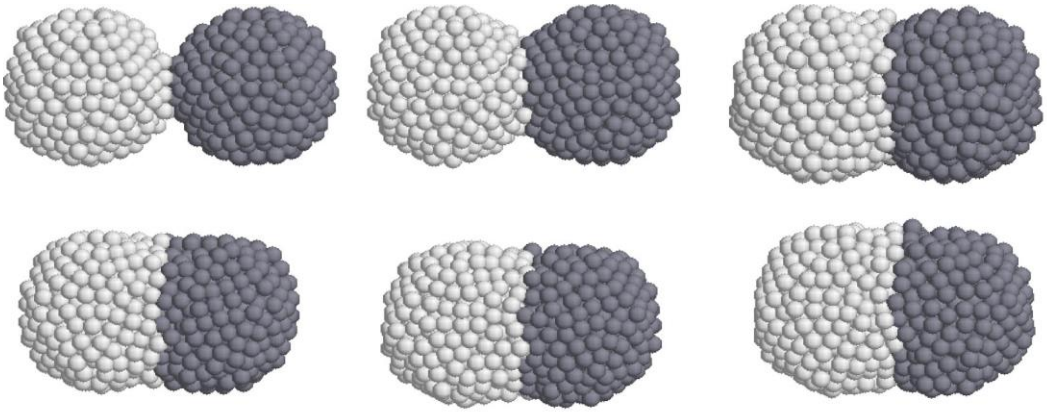

Figure 1.5 Coalescence of two Pb 565-atom icosahedra initially at 300 K. The sequences of snapshot at 3.75 ps intervals show the early growth of the neck after the initial contact. Reprinted figure with permission from reference[64] as follows: S. Hendy; S. A. Brown and M. Hyslop, *Phys. Rev. B*, **68**, 241403 (2003). Copyright 2003 by the American Physical Society.

Most of the unique properties of the NPs especially for the homogeneous nanocatalysts require the NPs not only sustaining the nano-size scale but also having a stable spatial dispersion. In order to avoid the agglomeration[74, 75] during the applications, researchers, nanocatalyst suppliers and manufacturers have been using different synthesis methods, utilizing reducing agents as well as the stabilizers for the NPs. For example, the commonly used reducing agent in the nanocatalyst is the protective gas[76-78], including the H_2, CO and H_2/CO with different ratios. To take a general view for the field of the nanocatalysts industry, the global top companies, which specialize in different areas, are listed below based on the alphabetical order of the company name[79]:

Argonide Corporation, BASF Catalyst LLC, BASF SE, Bayer AG, Catalyst Solution, Inc., Evonik Degussa GmbH, Genencor International, Inc., Headwaters Nanokinetix, Inc., Hyperion Catalysis International, Johnson Matthey PLC, Nanophase Technologies Corporation, NanoScale Corportation, NexTech Materials Ltd., Oxonica, PQ Corporation, Sachtleben Chemie Gmbh, Sud-Chemie AG, Unicore NV and Zeolyst International.

1.3 Single Small Nanoparticle on the Freestanding Graphene Sheet

In heterogeneous catalysis, the nanometric catalysts are commonly well dispersed on dissimilar substrates (supports). In chemical and petrochemical industries, supported catalysts are widely used for a wide spectrum of applications. Indeed, the supports do behave as spacers suppressing the agglomeration of NPs at elevated temperature. More importantly, the synergic effects between the support and the NPs, namely the metal-support interaction, enable further optimizations of the catalytic properties through tailoring the NPs' morphologies, electronic structures and active sites of chemisorptions. It therefore becomes of great significance to examine the surface melting behaviors of NPs on the support.

Much effort has been devoted to the investigations of conventional supported catalysts using both experimental and computational methods. Recently, graphene, the single layered graphite, has been shown with fascinating multi-functional properties including exceptionally high surface area, strength and electronic conductivity, along with quantum dots effects and great catalytic activity. Moreover, it does not corrode in acid or alkaline solutions and is flexible[80] making it a perfect support anchoring the NPs and other functional nanomaterials. In particular for electrochemical and electrocatalytical applications, owing to the strong affinity between the C and the NPs (for example, Pt[62, 63] NPs and Ni[81, 82] NPs), the nanocomposit could have the enhanced electron transport rate and greatly improved electrolyte contact area (hydrophobicity) by tuning the surface chemistry of graphene substrates[83]. Another example comes from the Pt NPs that can be used to replace the solid Pt film where the catalytic activity for oxygen reduction reaction in fuel cells was not deteriorated due to the quantum size effects[84, 85]. On the other hand, the interaction between the carbon and the metal NPs are also evidenced in non-electrocatalytic process. The Ni NPs[11] facilitated the carbon nanotube growth and CNTs decorated with noble-metal NPs are mostly used for producing highly efficient PEMs (polyelectrolyte multilayers)[86].

Nevertheless, there are still many unknown to be explored for grapheme-NPs interactions; recent researches also highlight the lack of fundamental understanding of the electrochemical interfaces at the nanoscale and the behavior of the NPs in the materials system[80]. Considering the investigation of the geometry, size, dispersion and contact details, the computational modelling and simulation will be of great importance in designing future electrochemical and electrocatalytic devices.

1.4 String-Like Collective Atomic Motion in NPs

1.4.1 Mobile Atoms and Immobile Atoms

Assuming the atomic motion in a perfect bulk solid, all the atoms try to seek their most stable position via vibration governed by the balance of the repulsive force and attractive force from the interactions with the surrounding atoms. Usually these positions are fixed and called the equilibrium position, in another word, the atoms are "immobile" and the lattice maintains both short- and long-range orders.

What about the atomic interaction in the liquid materials? Atoms would appear similar vibration motion but it is not the only thing – they do not have fixed regular position. In simple term, if a collision of two atoms takes place, the atoms involved may rebound and diffuse away, further than the bulk material spacing constant, get a new balanced position and start another motion again.

To make it convenient for discussion in the NPs, numerical expression is used to define the “mobile” atoms, that is, the threshold atomic displacement condition is $ar_0 < | r_i(t^*) - r_i(0) | < br_0$, where r_0 is the bulk material spacing constant and the coefficients a and b are determined based on specific cases. It refers that the mobile atoms are those particles whose displacement $r_i(t)$ exceeds ar_0 after a diffusive decorrelation time t^*, but is smaller than the distance defined by the br_0 value. The ar_0 is slightly larger than the typical amplitude of an atomic vibration and br_0 is generally much larger than the first nearest neighbor distance. Therefore, the atoms for the NP cores, only vibrating around the fixed distance which is smaller than the ar_0, are considered immobile thus making the NP core essentially defect-free.

1.4.2 String-like Motion

The mobile atoms may result in a peculiar permutational type of atomic motion rather than the simple diffusion motion, namely a cooperative motion in a string-like path[87]. This spatial relation of atoms involved in one string is that when one of the mobile atoms has moved, a second mobile atom occupied its position, seen in Figure 1.6a. The mathematical expression, for reference mobile atom i and its neighbor j considered to be within a collective atom displacement, is, $\mathbf{min}(| r_i(\Delta t) - r_j(0) | , | r_i(0) - r_j(\Delta t) |) < 0.43r_0$, where r_0 is the bulk material spacing constant.

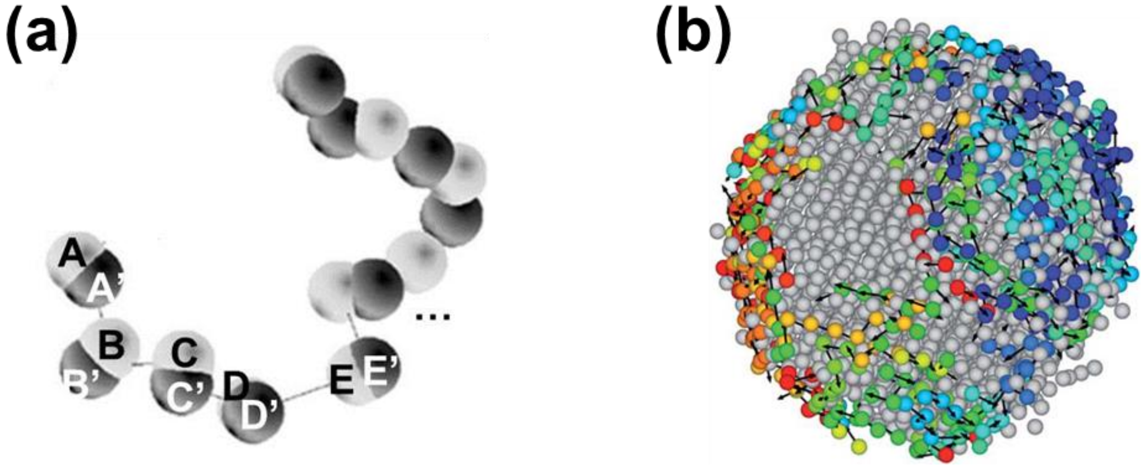

Figure 1.6 (a) An example of the string-like motion for reference mobile atom and its neighbors. Reprinted with permission from reference[87] as follows: C. Donati, J. Douglas, W. Kob, S. Plimpton, P. Poole and S. Glotzer, *Phys. Rev. Lett.*, **80**, 2338-2341(1998). Copyright 1998 by the American Physical Society. (b) The string-like motion in NP interfacial region. Adapted from reference[88] with permission from The Royal Society of Chemistry.

The string-like collective atomic motion is not only restricted in NPs[88], shown in Figure 1.6b, but prevails in all glass-forming (GF) liquids (including water, polymer fluids, metallic GF liquids, concentrated colloidal suspensions and even strongly driven granular fluids).

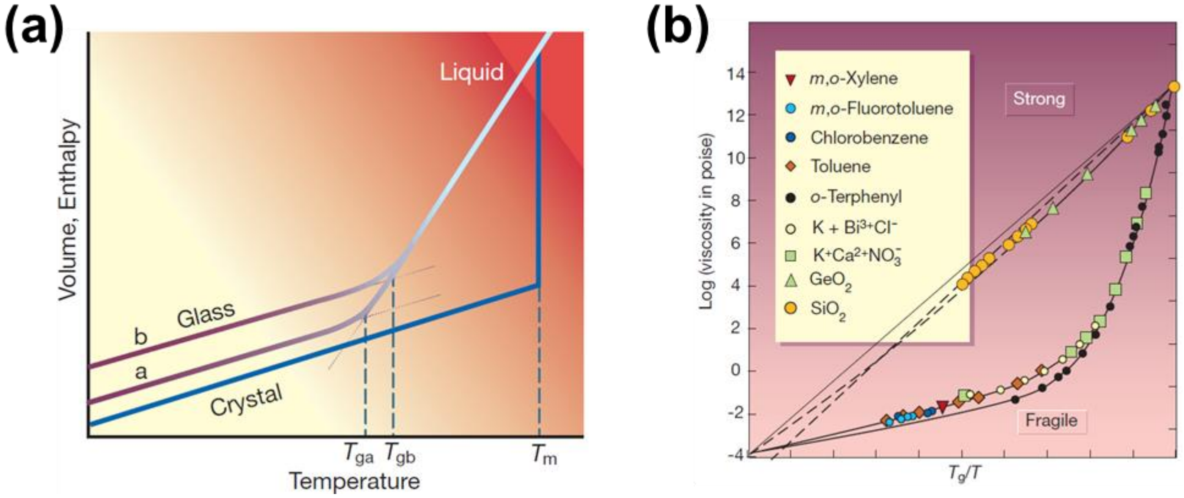

Figure 1.7 (a) temperature dependence of a liquid's volume or enthalpy at constant pressure; (b) viscosity of glass forming liquids as a function of rescaled temperature T_g/T. Two figures are from reference[89]. Reprinted by permission from Macmillan Publishers Ltd: *Nature*, advance online publication, 8 March 2001 (doi: 10.1038/35065704)

The Angell plot[90] gives the fragile-strong pattern of T_g-scaled Arrhenius representation of GF liquids which is illustrated in Figure 1.7. The "fragile" and "strong" property is not directly proportional to the mechanical properties, while fragility characterizes how rapidly the dynamics of a glass slow down as it is cooled toward the glass transition. T_g is the glass transition temperature[91, 92], which can be defined in two ways: the first is by viscosity η (T_g) = 10^{12} Pa·s, or 10^{13} P, and the second is by the temperature at which the average relaxation time in the equilibrium liquids is 100 s. In experiment, to characterize the "fragile" and "strong" property, the criterion is to see how the local slope of the η (T) curves are changed with the temperature. If the slope of the η

(*T*) curves of the glass-former depends on the temperture, it is called “fragile”, whereas it is “strong” for the one whose slope is independent of the temperature.

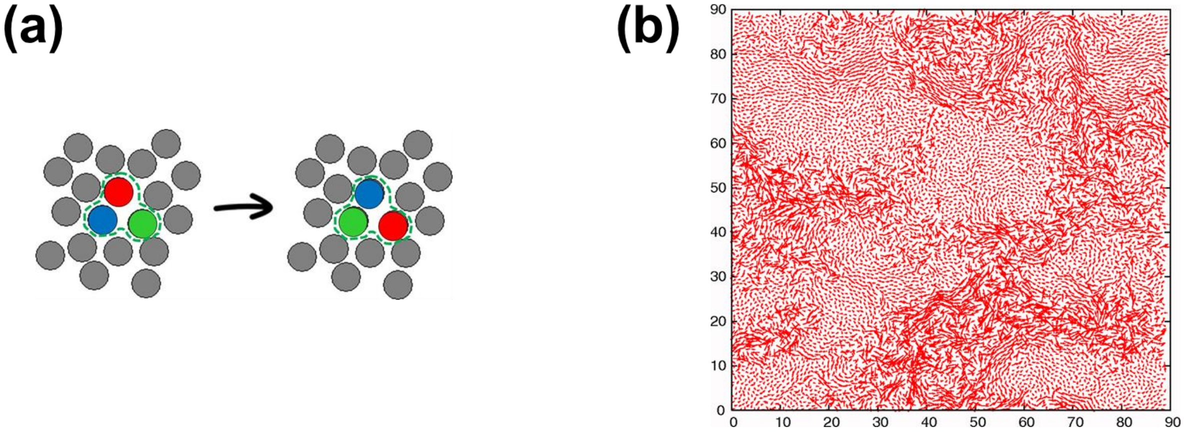

Figure 1.8 (a) Typical CRR (cooperative rearranged region) and (b) spatial map of single-article displacements in the simulation of a binary mixture of Lennard-Jones mixture in two dimensions. Arrows show the displacement of each particle in a trajectory of length comparable to the structural relaxation time. The map reveals the existence of particles with different mobilities during relaxation, but also the existence of spatial correlations between these dynamic fluctuations. Reprinted with permission from reference[93] as follows: L. Berthier and G. Biroli, *Rev. Mod. Phys.*, **83**, 587-645 (2011). Copyright 2011 by the American Physical Society.

Because of the thermal vibration reduction of the atoms upon cooling, the viscosity η (or equivalently, the relaxation time τ) of the GF liquids will increase by many order of magnitude. This strong activation energy dependence of temperature is due to a "cooperative rearrage region" (CRR) of many molecules, a terminology firstly introduced by Adams and Gibbs (AG) [94], with its illustration shown in Figure 1.8a. However, the knowledge to the size of this kind of regions is still inadequate[89]. In NP system, the string is the typical CRR (as in Figure 1.8b) when the whole particle undergoes thermal heating or cooling treatment, especially near T_g. Identifying the microscopic mechanism which gives rise to the dramatic slowing down of the relaxation dynamics is the most important challenge in the field of GF liquids.

1.4.3 Dynamic Interfacial Layer on the Surface of Ni NPs

One of the most practical methods for modifying the NP surface and interfacial structure is to alloy different types of metals with NPs, with the promise to create more effective catalysts. Metals reported, such as Au[95, 96], Pt[97], Ag[98] and Pt/Ru[99], are immiscible with Ni, so that they can just segregate to the outer surface layer of Ni NP. Besenbacher *et al.*[95] has verified by experiments that Au was alloyed into the first surface layer of Ni resulting in lowered surface energy of Ni, and the alloying effect helped to stabilize the steaming-reforming activity which would deactivate rapidly with time for pure Ni catalyst. Fu *et al.*[99] also has shown that Pt-rich shell coated Ni NP exhibited better catalytic activity and resistance to carbonaceous intermediate poison than pure NP. By alloying Ag, the reactive step sites of Ni(111) can be controlled by blocking the steps with Ag, thus affecting the bond-breaking selectivity and the reactivity of catalytic surfaces[98]. Based on our previous studies of GF fluids[88, 100] on which the molecular and nanoparticles additives can be expected to influence the collective atomic motions so that those observations give insights that the surface-segregated additives can be significant to understand the alloying effect to the NP interfacial dynamics.

1.5 Challenges, Objectives and Thesis Contents

Surface melting for NPs has been attracting tremendous attentions because of the closely related surface and interfacial mobility which underlies the unique properties of the NPs. Kang *et al.*[101] have alternatively described Al_{55} clusters as being 'half-solid' because of the high mobility of the surface atoms in these small NPs. Zhang *et al.*[102] have noted the existence of unexpected solid-to-solid structural transition below the melting temperature in Ni NPs having about 900 atoms, while the dynamics of NPs with more atoms could be characterized as 'surface pre-melting' on a solid crystalline core. Uppenbrink and Wales[103] investigated the clusters of 13 to 150 Lennard-Jones atoms and found the different capping could be crucial in the determination of the stability of cluster structure. Wales and Munro[104] further studied the morphology change between icosahedra, cuboctahedra, and decahedra in metal clusters with 13, 55 and 147 atoms (magic number) and found cooperative rearrangement of atoms were responsible the NP structural changes that this small NP regime. Interestingly, the rearrangements found in these studies occur via a single transition state, while those in larger NPs[105] studied later occurred through a sequence of transition state events. The exact nature of atomic motions in this liquid-like layer of NPs and the fundamental causes of the shape fluctuations in single and multiple small solid NPs has not been investigated before, either computationally or experimentally.

The previous study focuses on the structure and interfacial dynamics for relatively large NP, e.g. clusters having a size more than 369 Ni atoms and a particle diameter more than 2 nm. However, the local structure of ultra-small NP clusters with respect to the potential energy landscapes[106] will result in different stable configurations, and the dynamic properties haven't been touched yet. What's more, shape fluctuation and local structure changes may take place caused by the atomic motions rather than only for the interfacial region. So the small size range, 0.5 nm to 2.1 nm[47, 107], will be of great significance to some NP catalyst, i.e. used in the production of carbon nanotubes (CNT).

Here are two major objectives that are expected to achieve through this study:

Understand and quantify the atomic motions, especially the string-like atomic motions that govern the interfacial dynamics of NP during melting and crystallization, and the local structure changes for the single small NP, and the multiple small NP during the coalescence.

Further explore and investigate the atomic motions and the interfacial dynamics for single NP under the constraint from the graphene substrate.

Based upon the above objectives, the following content of this thesis is listed below:

In Chapter 2, I describe the overall methodology, which is MD (Molecular Dynamics) simulation, from the aspects of the potential, the temperature control, the boundary condition and the data analysis techniques. In Chapter 3, "spontaneous shape fluctuations in single small nanoparticle", I examine the NP shape fluctuations in a single isolated Ni NP having a radius, $r \approx 1$ nm, by looking into the fluctuations in the NP potential energy, Debye-Waller factor, and shape changes of the NP through determination of the radius of gyration tensor of the NP as a function of time. In Chapter 4, "coalescence of multiple small nanoparticles", I first investigate the relative shape anisotropy and the local structure that is characterized using the Honeycutt-Andersen (HA) index, and then examine the evolvements of the local fcc structure, the local icosahedral structure and the liquid-like structure. In Chapter 5, "single small nanoparticle on the freestanding graphene sheet", I create the model that the single Ni NP is interacted with the flat freestanding graphene sheet and then evaluate the interfacial dynamics of the NP, compared with the single NP without the graphene substrate as a constraint. In Chapter 6, I summarize my general conclusions, discuss some of the remaining open questions and recommend the directions for the future work in the NP research area with respect to the interfacial dynamics.

2 Methodology

Scientific researchers either do direct observations from the sample preparation in experiments, or establish analytical studies and numerical simulations to probe the scientific questions involving as small as the neutrons and the proton, and as large as the whole universe. In some fields in the materials science, however, the lack of real time observations is a serious problem for our understanding. Furthermore, the observations can't always to be all correct -- in fact, sampling limitations and measurement errors can result in ambiguous interpretation of the results which leads to the misunderstanding of the real physical process. Last but not least, another major restriction of observations is that high expense and operations, for example the complex sample preparation, easily stained purity and the huge challenges with the *in situ* characterization by scanning microscopy measurements, restrict the experiments that can be made. In these above cases, theoretical study and numerical simulation become extremely important.

2.1 Molecular Dynamics Simulation

MD simulation is one of the most effective and feasible methods to investigate the interfacial dynamics and kinetics of NPs both with clean "experimental" environment and good control of all "experimental" parameters. Meanwhile, it is suitable to observe the melting process of NPs directly on the atomic level in MD simulations. However, the length and time scale limitation in MD simulation will prevent it from the further application based on length- or time-dependent process. The typical times range from 10^{-13} second for local oscillations, requiring molecular simulation time steps of 10^{-14} second, up to seconds or hours for the diffusion time of a chain, and to much longer times for collective phenomena or relaxation in glassy regimes. The spatial scales range from a few angstroms (the size of an atom), to hundreds of atoms for a complete polymer chain, and to millimetres for collective phenomena taking place in a solution of polymer chains. Figure 2.1 shows the length scale with respect to atoms number and size, and this thesis involves the atoms number from about 10 to about 10^3. The timestep in this simulation is chosen to be no larger than one tenth of the Debye frequency, i.e., on the order of 10^{-15} second. Therefore, the time and length scale in MD simulation is enough for carrying out experiments in this thesis.

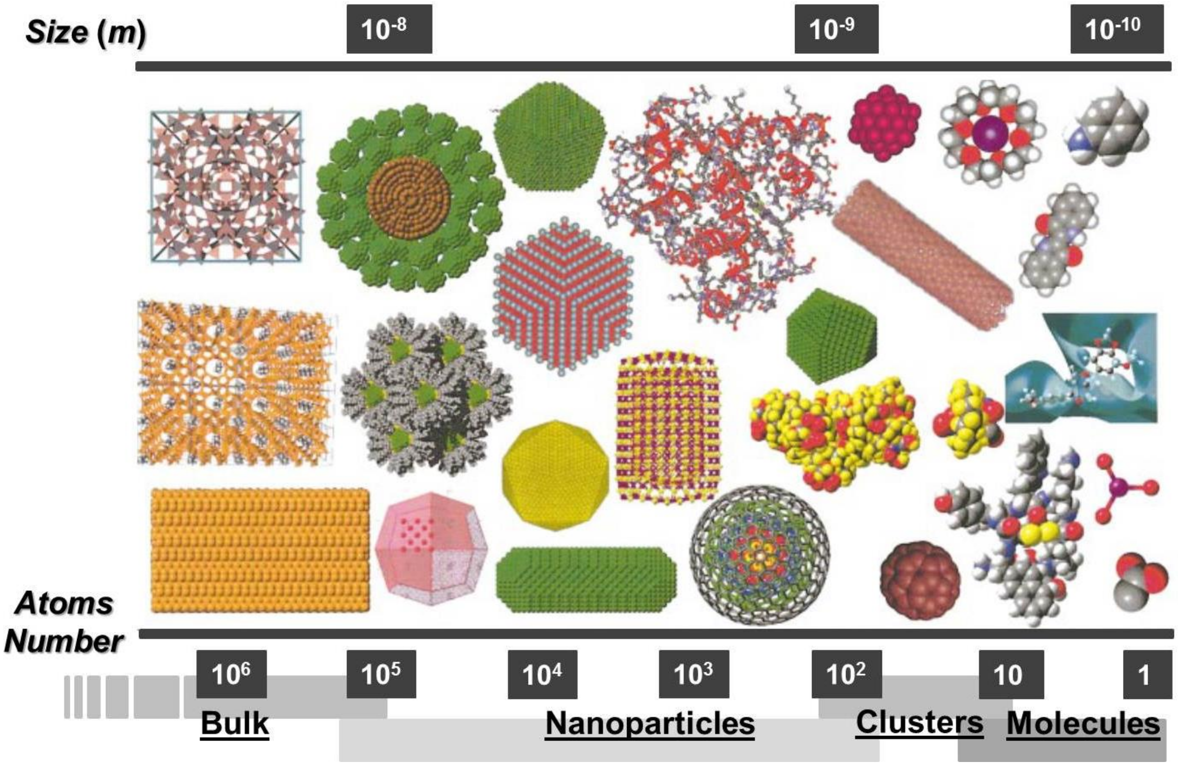

Figure 2.1 Diagram of different length scales with respect to atoms number and size. Reprinted with permission from reference[39]. Copyright 2001, American Vacuum Society.

In MD simulation, the numerical integration of Newton's equation is used to govern the motion for each particle, which is obtained as the gradient of material potential energy with respect to the position. Once the force is known and the initial position and velocity of each atom are given, the derived successive accelerations, velocities and positions of the whole process can be obtained by doing integration numerically, together with the related thermodynamic, structural or kinetic properties of the system. The calculation methodology is given as a flow chart in Figure 2.2.

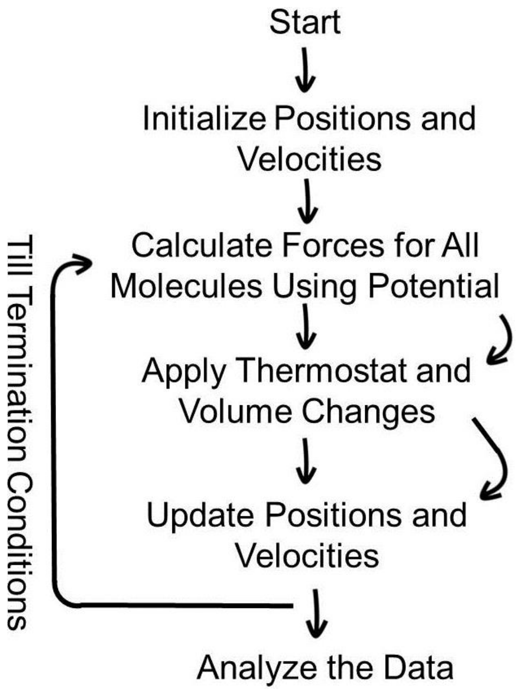

Figure 2.2 Flow chart of the MD simulation process

Another important aspect is that the statistical mechanics plays a key role in MD simulation. In statistical mechanics for a microscopic level, a system made of *N* particles is characterized by the position $\boldsymbol{r}_{\mathrm{i}}$ and momenta $\boldsymbol{p}_{\mathrm{i}} = mv_{\mathrm{i}}$. These ($\boldsymbol{r}_{\mathrm{i}}$, $\boldsymbol{p}_{\mathrm{i}}$) can take any values (or states), constrained by the external thermodynamic parameter, such as *T* and *P*. The subject of statistical mechanics is to link the microscopic parameters i.e. $\boldsymbol{r}_{\mathrm{i}}$ and v_{i}, with the macroscopic properties i.e. the temperature *T*, the volume *V* and the pressure *P*. The phase space $\boldsymbol{\Gamma}$ is the space in which all possible states of a system are represented. An ensemble then is regarded as a collection of points that a set of *N* particles could be arranged in the multi-dimensional phase space $\boldsymbol{\Gamma}$, where each point represents a complete *N* particle system. Thus, an ensemble is consisting of a large number of virtual copies (sometimes infinitely many) of a system, considered all at once, each of which represents a possible state that the real system might be in.

The ensemble average is obtained by summarizing the values of each representative point and normalized by the total number of the points. However, the ergodic hypothesis says that the time average is replaced by the ensemble average due to the fact that it's not feasible to get ensemble average for a macroscopic system ($N > 10^{23}$). The time average is taken over all states encountered in a dynamical trajectory of the system over a long period of time, which is considered simultaneously.

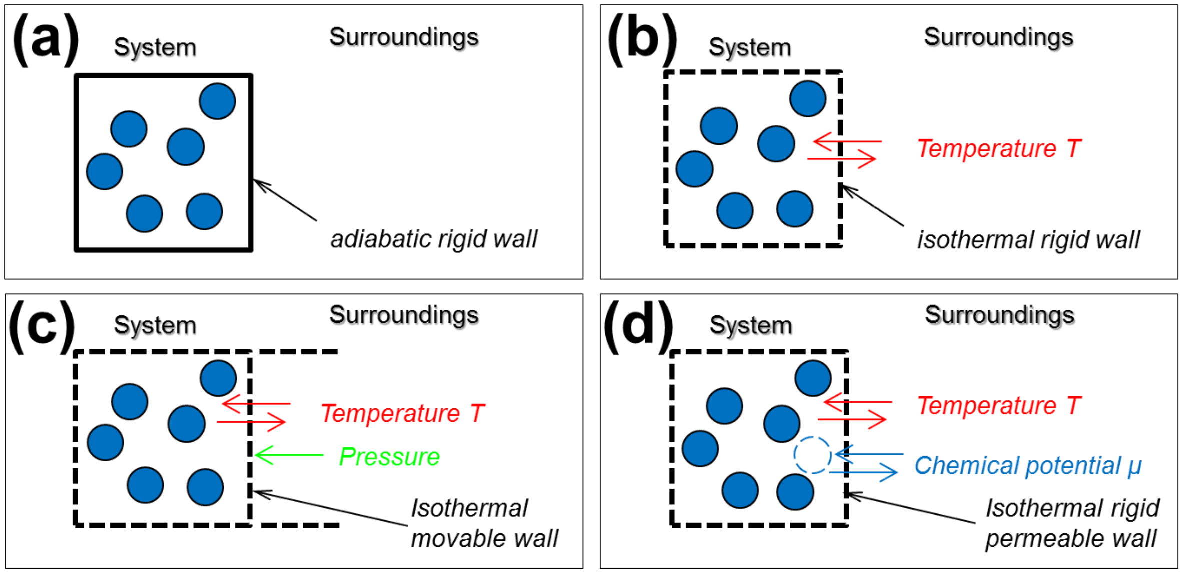

Figure 2.3 Schematic maps for different ensembles in statistic mechanics: (a) microcanonical *NVE* ensemble, (b) canonical *NVT* ensemble, (c) isothermal-isobaric *NPT* ensemble and (d) grand canonical μVT ensemble

Depending on which state variables (for example, the energy E, volume V, temperature T, pressure P, number of particles N and the chemical potential μ) are kept fixed, different statistical ensembles can be generated. Figure 2.3 shows four ensembles used in statistical mechanics, the microcanonical ensemble (NVE), canonical ensemble (NVT), isothermal-isobaric ensemble (NPT) and grand canonical ensemble (μVT). In all ensembles, the number of particles N is conserved. In the NVE ensemble, the total energy E, the number of particles N and the volume V are fixed. The system must remain totally isolated so it is unable to exchange energy or particles with its surrounding environment. In the NVT ensemble, the number of particles N, the volume V and the temperature T are fixed. The system exchanges heat with a heat bath and thus it's a closed system. In the NPT ensemble, however, the volume can be changed and the total pressure is fixed. In the μVT ensemble where neither the energy E nor particle number N is fixed, the system can exchange heat or particles with its surrounding environment, which is represented by the change of the chemical potential μ.

2.2 Potential

Potential used in the simulation is a function U (r_1, r_2, …, r_N) of the positions of the nuclei, representing the potential energy of the system when the atoms are arranged in a specific configuration. The expression for one of the simplest pair-wise potential is as follows, which can be utilized to describe the two-body bonding interactions for both the primary bonds (ionic bonds, covalent bonds and metallic bonds) and secondary bonds (van der Waals bonds and hydrogen bonds),

$$E_{tot} = \sum_{i,j} \left\{ 4\varepsilon_{ij} \left[\left(\frac{\sigma_{ij}}{r_{ij}} \right)^{12} - \left(\frac{\sigma_{ij}}{r_{ij}} \right)^{6} \right] + k_e \frac{q_i q_j}{r_{ij}} \right\} \tag{2-1}$$

In this equation, the total potential energy E_{tot} is the sum of the Lennard–Jones potential plus the Coulombic pairwise interaction between two atom i and j with the distance of r_{ij}, where ε is the depth of the potential well, σ is the zero-crossing distance for the potential, $k_{\text{e}} = 8.988 \times 10^9$ N m^2 C^{-2} is the Coulomb constant and q is the charge of the atom.

Apart from the Coulombic pairwise interaction term, the rest term the Lennard–Jones potential is an excellent model for noble gases, e.g. Ar, Ne and Xe. However, the pair potentials has its limitation for transferability, i.e. the parameters determined for molecules can't be used for crystals, and some parameters for specific types of crystals can't be used to describe the larger range of crystal structures. For example, the difference between FCC and BCC is not captured using a pair potential. Thus, more sophisticated potential type, e.g., the EAM potential and the Reaxff reactive force field potential are introduced based on the specific needs for this thesis studies.

2.2.1 Voter-Chen EAM Potential

The Embedded Atom Method (EAM)[108], as a many body potential is utilized in this study rather than pairwise interaction -- two body approximations because the summation over larger group of particles can provide more accurate results although it may cost more computer resource and time. EAM is ideal for metallic bonding and numerically efficient for billions of atoms. The introduction of a delocalized valence electrons moving between the nuclei generates a binding force to hold the atoms together in term to the total potential energy.

In this method, the energy of the metal is treated as the energy obtained by embedding the atom or nuclei into the local electron density provided by the remaining atoms of the system. The expression is as follows:

$$E_{tot} = \sum_i F_i(\rho h, i) + \frac{1}{2}\sum_i \sum_{j \neq i} \phi_{ij}(R_{ij}) \qquad (2\text{-}2)$$

and

$$\rho h, i = \sum_{i \neq j} \rho_j^{\alpha}(R_{ij}) \qquad (2\text{-}3)$$

where $F_i(\rho h,i)$ is the embedded energy of atom i, $\phi_{ij}(R_{ij})$ is the pairwise repulsion between atom i and j with the distance of r_{ij}, and $\rho h,i$ is the electron density at atom i, contributed by other atoms j. Like the Lennard-Jones, the EAM potential is a combination of short-range attraction and still shorter range repulsion[41]. The functional form for the embedding energies $F(\rho_{h,i})$ is obtained empirically by adjusting parameters to fit known bulk properties of the elements such as sublimation energy ΔH_s, lattice constants, elastic constants and vacancy formation energy. Thus the total energy E_{tot} is minimized by adjusting the lattice constants or atomic coordinates to find the configuration that yields the lowest possible energy. These calculations are usually performed at 0 K and do not include entropic contributions.

Table 2.1 Experimental and calculated properties of Ni[109, 110]

Properties of Ni	Experiments	Calculations
Equilibrium lattice constant a_0 (Å)	3.52	3.52
Cohesive energy E_{coh} (eV)	4.45	4.45
Bulk modulus B (10^{12} erg/cm^3)	1.81	1.81
Vacancy formation energy ΔE^f (eV)	1.60	1.60
Bond energy D_e (eV)	1.95	1.94
Bond length R_e (Å)	2.20	2.23

The Voter-Chen form[109] for pure Ni simulation are chosen as the EAM potential here. This potentials accurately reproduce the lattice constant, cohesive energy, elastic properties, and the vacancy energy[109, 110]. The related parameters are list in Table 2.1.

2.2.2 Reaxff Reactive Force Field Potential

For the applications of Ni NPs, they are usually used in the chemical environment thus may undergo chemical reactions involving the bond breakings and formations. In terms of the simulations, the simple pair potentials can't describe chemical reactions. Reactive potentials or reactive force fields overcome these limitations, and are widely used in simulations for the chemical reactions, catalysis, etc. The advantage of reactive force fields over conventional molecular mechanics force fields is that they can, with the same parameters, describe several different bonding states of an atom, and thus to some extent may be able to describe chemical reactions correctly. Because the reactive force fields can automatically determine whether a pair of atoms is bonded or unbonded[111] and is extremely subtle regarding the bond and energy, it is designed for more complex materials/chemistry, including σ bond, π bond and double π bond formation and breaking.

Reaxff Reactive Force Field is based on a bond-order model in conjunction with a charge-equilibration scheme and has been extended to hydrocarbons, proteins, metal systems, fuel cells and combustion and may other elements and compounds comprised of H/C/O[112], Si/SiO_2/SiC[113], Al/Al_2O_3[114], Pt/PtH/PtC (fuel cell anode)[115, 116], B/N[117], Y/Zr/Ba/O/H[118] and C/Ni/H[119-122], enabling the dynamics studies of reactions in material science.

The overall system energy for the reactive force field potential includes various partial energy contributions, as demonstrated by

$$E_{system} = E_{bond} + E_{lp} + E_{over} + E_{under} + E_{val} + E_{pen} + E_{coa} + E_{C2}$$
$$+ E_{tors} + E_{conj} + E_{val} + E_{H-bond} + E_{vdWaals} + E_{Coulomb} \tag{2-4}$$

The specific energy terms are described as follows. E_{bond} is the bond energy, the attractive term directly derived from bond orders; E_{lp} is the lone pair energy, penalty for breaking up lone pairs in O and N; E_{over} is the overcoordination energy, penalty for overcoordinating atoms; E_{under} is the undercoordination energy, stabilizing undercoordinated atoms; E_{val} is the angle strain, whose equilibrium angle depends on bond order central atom; E_{pen} is the penalty for 'allene'-type molecules (H_2C=C=CH_2); E_{coa} is the angle conjugation, stabilizing the $–NO_2$ groups; E_{C2} is the C2 correction, destabilizing C=C; E_{triple} is the triple bond related; E_{tors} is the torsion energy; E_{conj} is the torsion conjugation, describing general conjugation stability; $E_{\text{H-bond}}$ is the hydrogen bond; E_{vdWaals} is the van der Waals energy, calculated between every atom; E_{Coulomb} is the Coulomb interaction, calculated between every atom, polarizable charges get updated every iteration.

The key of reactive force fields is that the bond energy between atoms i and j does not depend on bond distance, Instead, it depends on bond order. The bond order for both the metallic and ionic bonds, the σ bond (sp^3), the π bond (sp^2), and double π bond (sp) is treated as 0, 1, 2 and 3, respectively.

The potential file for Reaxff Reactive Force Field developing for the carbon nanotube can be obtained from the supporting information from the reference[123].

2.3 Temperature Control

The natural MD simulation is a microcanonical ensemble (*NVE* ensemble) because the total energy is conserved. Nevertheless, because of rounding and truncation errors during the integration process, there is always a slight drift in energy. The temperature and pressure can change with the time. In order to make sensible comparison with the experimental work which is usually operated at a constant temperature, many methods have been tried to control the system temperature to be constant. Two methods are utilized in this thesis study, the Nosé-Hoover method and the Berendsen thermostat method.

The Nosé-Hoover method[124, 125] is by introducing a thermostat (heat bath that can exchange heat with the system) and creating an additional virtual coordinate in order to couple the system with the reservoir. In this case, isothermal MD (canonical *NVT* ensemble) can be applied in the simulation process.

In the Cartesian system, the Hamiltonian takes the summation form of the total kinetic energy *K* and potential energy *U*,

$$H = K(\mathbf{p}^N) + U(\mathbf{r}^N) = \sum \frac{|\mathbf{p}_i|^2}{2m_i} + U(\mathbf{r}^N) \qquad (2\text{-}5)$$

Nosé-Hoover method is to add two additional degree of freedom, the "position" s of an imaginary heat reservoir to which the system is coupled, and the conjugate "momentum" p_s of this imaginary heat reservoir. In addition, the effective "mass" Q associated with the s in also introduced, such that $p_s = Q\,\dot{s}$. Note that the dot above the s represents the "d/d*t*".

The new Hamiltonian for the previous system and the reservoir is then constructed as

$$H = \sum \frac{\left|\mathbf{p}_i\right|^2}{2m_i} + U(\mathbf{r}^N) + \frac{\xi^2 Q}{2} + 3Nk_B T \ln s \tag{2-6}$$

The added last two terms belong to the heat reservoir, for its kinetic and potential energy. And the ξ is a friction coefficient that replaces p_s. The time evolution of the particle positions and momenta is governed by the following equations,

$$\frac{d\mathbf{r}_i}{dt} = \mathbf{v}_i \tag{2-7}$$

$$\frac{d\mathbf{v}_i}{dt} = -\frac{1}{m_i}\frac{\partial U(\mathbf{r}^N)}{\partial \mathbf{r}_i} - \xi \mathbf{v}_i \tag{2-8}$$

$$\frac{d\xi}{dt} = \left(\sum m_i \left|\mathbf{v}_i\right|^2 - 3Nk_B T\right)\Big/ Q \tag{2-9}$$

$$\frac{d \ln s}{dt} = \xi \tag{2-10}$$

The magnitude of the heat bath mass Q determines the coupling between the reservoir and the real system therefore is an important parameter to be chosen. The small Q (inertia) causes oscillations; the large Q results in poor coupling and long thermilization time. Usually Q needs to be found by trial and error.

Berendsen thermostat[126, 127] is another method by applying a weak coupling for the system with an external heat bath, which is also known as proportional thermostat. Rather than assuming the velocities are completely scaled to the target temperature at each time step, a time scale is assigned for the updating of the velocities. One advantage of Berendsen thermostat is that it allows the temperature fluctuations, and the corresponding ensemble is the microcanonical ensemble.

In order to move the system dynamics towards the desired temperature, a certain factor, the velocity rescaling factor υ, is multiplied by the velocities to correct the deviations of the actual temperature T from the prescribed one T_0. And the coupling constant, or time scale of heat transfer, is τ.

$$\upsilon^2 = 1 + \frac{\delta t}{\tau}\left(\frac{T}{T_{inst}} - 1\right) \tag{2-11}$$

Here, δt is the time step in the MD simulations. Typically, τ is two orders of magnitude more larger than δt.

The differences between the Nosé-Hoover and the Berendsen thermostat is that, due to the true coupling with the system, Nosé-Hoover can result in slowly dampening oscillations and a relatively long thermal stabilization process. Thus, Nosé-Hoover thermostat drives the system much softer than Berendsen thermostat. Meanwhile, the Berendsen thermostat is more efficient.

2.4 Boundary Conditions

In a numerical simulation, it is either impossible and or unnecessary to simulate the whole materials system. Generally we choose a region of interest in which we conduct a simulation, which definitely has a certain boundary with the surrounding system or environment. Different boundary conditions may cause quite different simulation results. Improper sets of boundary conditions may introduce nonphysical influences on the simulation system, while a proper set of boundary conditions can avoid those technical problems. Therefore the boundary conditions are very important for the simulation setups.

Commonly there are several different types of boundary conditions, e.g., the fixed boundaries, the periodical boundaries, the flexible boundaries and the free surfaces.

Fixed boundary conditions are suitable for applying a mechanical constraint. If the physical process concentrates in the center of the simulation region and causes very little influence on the boundary; at the same time, the surrounding environment of the simulation region is stable, such that we can set the boundary to fixed boundary conditions.

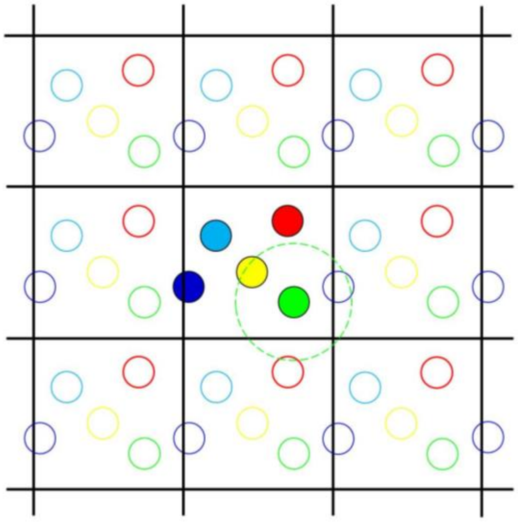

Figure 2.4 Two dimensional model for the periodical boundary conditions with the primitive unit and the surrounding cells. The dashed circle represents the interactions belonging to one specific particle

Periodic boundary conditions (PBC) are suitable for repeating systems. This treatment of the boundary condition corresponds to the physical assumption that, on the two sides of boundary, the same physical processes exist. The variable values at the same distance from the boundary at the two sides are the same. The function of such a boundary is that of a mirror that can reflect all the fluctuations generated by the simulation region. This kind of boundary condition fits for those environment values that do not change with time and physical processes well interior to the simulation region. The illustration for the PBC is shown in Figure 2.4.

Flexible boundary conditions are suitable for responsive systems, eg dielectrics, to avoid the use of rigid constrains. Free surfaces are suitable for the simulations regarding surface diffusion, adsorption etc.

In this thesis, the fixed boundary condition is applied in Chapter 3 for the single NP, where the entire system is the NP surrounded by the vacuum. The PBC is applied in Chapter 4 and 5 to all simulations where the the multiple NP particles as well as the graphene materials interact across the boundary and can exit one end of the box and re-enter the other end. Besides, the periodical length is selected based on different situations, for example, the single NP in this study has free surface in vacuum so that the large enough simulation box can satisfy the setup needs.

2.5 Simulation Initialization

For any numerical simulation, we need to have an initial state to begin the simulation. So we need to set the initial environment values at the beginning of simulation. The initial condition of a numerical simulation thus gives an initial state for the simulation region. The system evolution will start from this initial condition. The initial condition should be able to reflect the real physical environment; at least it should be an acceptable simplification of the real environment.

The initial configurations are more usual from a corresponded lattice structure. For example, the single Ni NPs are initiated from an approximately spherical shape and a perfect local fcc structure; the graphene sheet is extracted as a densely close packed hexagonal pattern with the desired chirality (*n*, *m*), length, width and bond length. The details of these initial configurations will be discussed as the specific cases in each following chapters.

According to the thermodynamics theory, each degree of freedom of a harmonic system contributes $1/2k_B\mathrm{T}$ to the kinetic energy in equilibrium, that is, where k_B is the Boltzmann constant and T is instantaneous temperature. The velocities are assigned with magnitudes conforming to the required temperature T and corrected such that the total momentum $\boldsymbol{p}$ of the system is zero, using the relation

$$\mathbf{p} = \sum_{i=1}^{N} m_i v_i = 0 \tag{2-12}$$

The velocity v_i, for a given atom, is assigned according to a Maxwell-Boltzmann distribution, which is a Gaussian distribution of speeds, which gives the probability $p(v_{ix})$ that an atom i has a velocity v_x in the x direction at the temperature T,

$$p(v_{ix}) = \left(\frac{m_i}{2\pi k_B T} \right)^{1/2} \exp\left(-\frac{m_i v_{ix}^2}{2k_B T} \right) \tag{2-13}$$

The temperature then can be calculated from the kinetic energy KE, using the equation,

$$KE = \frac{1}{2} \sum_{i=1}^{N} m_i v_i^2 \tag{2-14}$$

$$T = \frac{2KE}{3k_B} = \frac{1}{3k_B} \sum_{i=1}^{N} m_i v_i^2 \tag{2-15}$$

2.6 Data Analysis Techniques

The results of the dynamics and the system structure information for MD are characterized all by different parameters, which is one of the huge differences from those lab experiments. For example, one of the most typical parameter is the potential energy E, recorded as a function of simulation time, averaging over all the atoms. This information is very important to understand the status of the system. For example in the temperature dependence study, a sudden large increase of the potential energy would imply that the structure had become more disordered and possibly underwent melting or amorphisation. A sudden decrease might indicate a change of the more ordered structure, e.g., crystallizations. The potential change can reflect the degree of disorder at the beginning of the transformation.

2.6.1 Quantitative Analysis of the Local Geometry

Since fluctuations of NP shape are the primary concern here, we require a general measure of NP shape. The radius of gyration tensor provides an attractive choice for NP shape characterization and this quantity is often employed in the shape characterization of synthetic and biological macromolecules such as DNA and proteins.[128-130] The radius of gyration R_g is defined by,[131, 132]

$$R_g{}^2 = \frac{1}{N}\sum_i \left(r_i - r_{mass}\right)^2 \tag{2-16}$$

where r_{mass} is the center of mass and this quantity can be generalized by defining moments about different coordinate directions to define the R_g tensor.[133] The R_g tensor is symmetric in its components and can be diagonalized by rotating the particle to its principal axis orientation and the eigenvalues (λ_1, λ_2, λ_3) in the diagonal form of the R_g tensor then provide a basis for NP shape characterization. Following common practice in polymer physics,[131, 132] we define the NP asphericity b, acylindricity c and relative shape anisotropy k^2 as,

$$R_g{}^2 = \lambda_1^2 + \lambda_2^2 + \lambda_3^2 \tag{2-17}$$

$$b = \lambda_1{}^2 - \frac{1}{2}\left(\lambda_2{}^2 + \lambda_3{}^2\right) \tag{2-18}$$

$$c = \lambda_2^{\ 2} - \lambda_3^{\ 2} \tag{2-19}$$

$$k^2 = \frac{b^2 + (3/4)c^2}{R_g^{\ 4}} \tag{2-20}$$

The Honeycutt-Andersen (HA) index analysis[134] is used to characterize the local atomic structures for one pair of atoms either bonded or not, via categorizing the common nearest neighbors of these two atoms, which cannot be obtained by the conventional single-index parameter. Each atom pair (root pair) has a set of nearest neighbors, resulting in four numbers, namely (*klmn*), to be examined: (1) *k*, whose value is 1 when the root pair is bonded, otherwise is 2, (2) *l*, the number of neighbors common to both atoms, (3) *m*, the number of bonds between these common neighbors, and (4) *n*, the number to differentiate the local structures with the same *klm* but different geometries like the case of fcc and hcp. Here, HA index is simplified as *klm*. For example, in an fcc bulk crystal, each nearest-neighbor pair shares four common neighbors, among those common neighbors two bonds are found. Thus the signature of the atom pair is 142. Figure 2.5 shows more examples of the atomic configurations for HA index of 132, 143 and 155 structures. Since all 12 of the bonds of each atom in a fcc crystal are the same, we claim that the local environment of an atom with 12 nearest neighbors each of which has a 142 HA index signature is that of fcc bulk.

When only the bonded pairs are considered (*k* equals 1), the HA index can be divided into four categories[135-137], (1) the 142 bond type, characterizing the fcc structure, (2) the 155, 154 and 143 bond types, representing the icosahedral configurations, (3) the

120, 121, 130, 131, 132 and 133 bond-types, relating to the surface amorphous liquid-like state, and (4) the 144 and 166 bond types, relating to the bcc-like local structure. These four are named “fcc”, “icosahedral”, “others” and “bcc” throughout the entire discussions. It is especially suitable for this nanoparticle system, where a large number of the surface atoms are not fully bonded. In this discussion, the cut-off distance (3.09 Å) is used to determine the bonding. The fractions of various HA indices will be shown as the four categories described above.

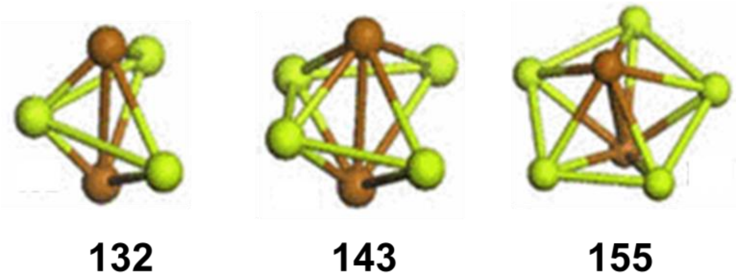

Figure 2.5 The Honeycutt-Andersen (HA) index for 132, 143 and 155 with the root pair atoms highlighted

2.6.2 Quantitative Analysis of the Global Structure

The structure of ordered solids and disordered molecular systems such as liquids can both be determined by radial distribution function (RDF), coordination number, etc.. The most commonly and used one is the RDF because it is effective to imagine the average structure by looking from the point of view of a single central reference atom, when all the atom positions change “randomly” within time. Figure 2.6 shows the sketch map how the RDF is obtained. The mathematical expression is $g(r) = n(r)/(\rho\ 4\pi\ r^2\ \Delta r)$, where $g(r)$ is the RDF, $n(r)$ is the mean number of atoms in a shell of width Δr at distance r, ρ is the mean atom density. This calculated average can be over time and over all atoms in the system.

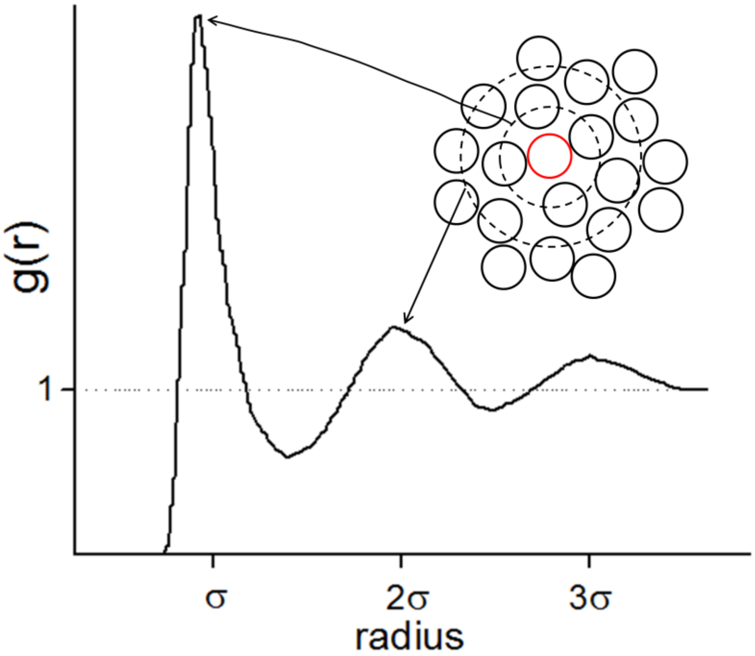

Figure 2.6 The radial distribution function on dependence of interatomic separation r. The inserted is the central atom (in red color) and shell distribution of the surrounding atoms.

Features in $g(r)$ for liquids and amorphous solids are due to packing (exclude volume) and possibly bonding characteristics. Firstly, at short separations (small r) the RDF is zero. This indicates the effective width of the atoms, since they cannot approach any more closely. Secondly, a number of obvious peaks appear, which indicate that the atoms pack around each other in shells of neighbours. The occurrence of peaks at long range indicates a high degree of ordering. Usually, at high temperature the peaks are broad, indicating thermal motion, while at low temperature they are sharp. They are particularly sharp in crystalline materials, where atoms are strongly confined in their positions. At very long range every RDF tends to a value of 1, which happens because the RDF describes the average density at this range.

2.6.3 Quantitative Analysis of the Dynamics

The dynamical features of glassy liquids can be studied via various types of time correlation functions. One of the simplest time correlation functions is the mean squared displacement (MSD) as $\langle \Delta r^2(t) \rangle = \langle (r_\mathrm{i}(t) - r_\mathrm{i}(0))^2 \rangle$ of a tagged atom.

Instead of simply being added together the distance of each step, the square of the distance of $\Delta r^2(t)$ are added so that it will always be added positive qualities to total. In this case, the sum will be always positive, which grows larger with every step. In a molecule system an atom or a molecule moves in three dimensions, but the same principle applies. Also since there are many molecules, the squared displacement should be calculated for all of them. The average square distance taken over all the molecules, gives us the MSD.

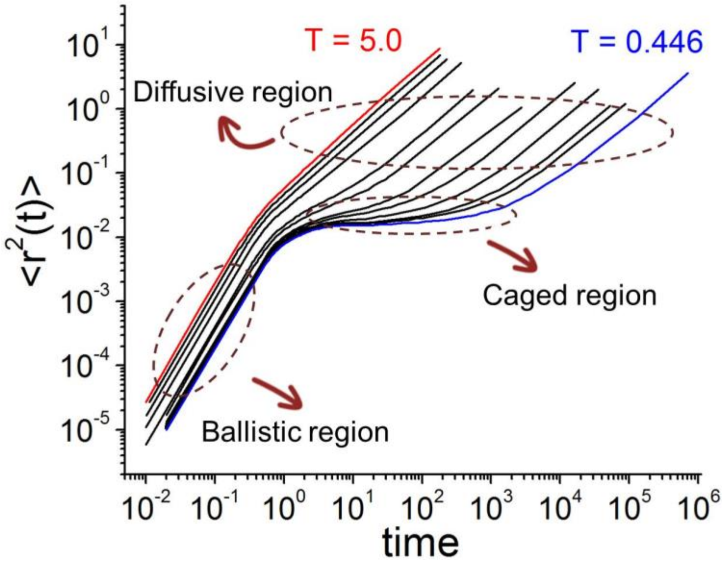

Figure 2.7 Time dependence of the mean squared displacement of A particles in a binary Lennard-Jones mixture. Reproduced from online document[138].

An example for its time and temperature dependence is shown is Figure 2.7. From high to low, the curves correspond to the temperatures $T = 5.0$, 4.0, 3.0, 2.0, 1.0, 0.8, 0.6, 0.55, 0.50, 0.475, 0.466. At high temperatures *two* regimes can be distinguished: one is the ballistic regime, the other is the diffusive regime.

The ballistic regime corresponds to short times, for example $t \leq 0.2$ in Figure 2.7. The curves present "linear" in Figure 2.7 because the log-log plot is applied, which makes the quadratic function have a slope of 2. This nonlinear feature of short times is due to the following fact. The path an atom or a molecule takes will be an approximate straight line until it collides with its neighbors. Only when it starts the collision process will its path start to resemble a random walk. Until it makes the first collision, we may say it moves with approximately constant velocity, which means the distance it travels is proportional to time,

$$v_i = \frac{dr_i}{dt} = constant$$

and its MSD is therefore proportional to the time squared, $\langle \Delta r^2(t) \rangle \propto t^2$. This constant of the proportionality, based on the Maxwell-Boltzman distribution, can be obtained immediately that $\langle \mid v_\mathrm{i}(0) \mid ^2 \rangle = 3k_\mathrm{B}T/(2m)$. Thus at very short time, the MSD is shown as a parabola and in the log-log plot has a slope of 2.

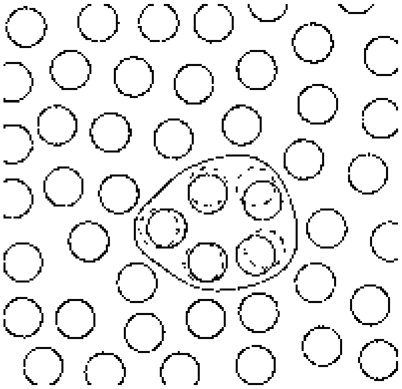

Figure 2.8 Schematic plot of the cage effect

At long times, when collision happens between the particles, the MSD enters the diffusive regime. This means the atoms or the molecules start to interact with their neighbors and therefore their motion is no longer ballistic. Especially at high temperatures these collisions make the velocities change quickly and randomly and consequently the MSD becomes a linear function. In the log-log plot the MSD has a slope of 1.

Table 2.2 Typical features of the MSD curves

	Name of the Regime	Curve Characteristics
Short Times	Ballistic regime	$\langle \Delta r^2(t) \rangle \propto t^2$, in log-log plot the slope is 2
Long Times	Diffusive regime	$\langle \Delta r^2(t) \rangle \propto t$, in log-log plot the slope is 1
Intermediate Times at Low *T*	Caged regime	The cage effect shows that with the decreasing *T* the dynamics slow down quickly since the length of the plateau increases.

At low temperatures the MSD has *three* regimes: the ballistic regime, the diffusive regime and the caged regime. As the "Cage region" pointed out in Figure 2.7, a plateau occurs, becoming larger with decreasing temperature and extending over several time decades at the lowest temperature. The plateau indicates that the MSD is basically constant at this time. That's because during this time, each moving atom is temporarily trapped in the "cage" formed by the surrounding neighbors, which is illustrated in Figure 2.8. Hence it cannot move beyond a length scale that is related to the nearest neighbor distance. As the temperature is lowered, the cage is becoming more and more rigid due to the increased viscosity, and only for larger times this cage starts to break up. Then the atoms begin to diffuse. The caged regime in fact is the only time regime which shows a noticeable *T*-dependence. The typical features of the different regimes for the MSD curves are listed in Table 2.2.

The non-Gaussian parameter α_2 is a measure of dynamic heterogeneity (DH), and the peak position of α_2 represents a characteristic time t^* of the DH. Previous works on glass-forming liquids[139, 140] and superheated crystals[141] have shown that t^* can be interpreted as a *diffusive relaxation time*. In three dimensions, α_2 is defined in terms of powers of the mean-square atomic displacement,

$$\alpha_2(\Delta t) = \frac{3\langle r^4(\Delta t)\rangle}{5\langle r^2(\Delta t)\rangle^2} - 1 \tag{2-21}$$

and this quantity is defined to equal zero for Brownian motion. The non-Gaussian parameter can also be defined in terms of a 4-point velocity function that measures fluctuations in the mobility[142, 143].

Generalization of the pair correlation function to a time-dependent correlation function provides displacement distribution function, or called van Hove correlation function, with its self-part as:

$$G_s(r,t^*) = \frac{1}{N}\sum_k \langle \delta(\vec{r} - [\vec{r}_k(t^*) - \vec{r}_k(0)])\rangle \tag{2-22}$$

which is proportional to the probability that a particle has moved a distance r in time t^*. The peaks in G_s (r, t) at successive nearest neighbour distances indicate a “hopping” motion of some of the atoms. The feature allows us to distinguish different kinds of atomic motions that contribute to G_s (r, t). The minimum in G between the maxima in G at $0.43r_o$ defines a well-defined cut-off scale for defining mobile particles and this scale arises in the quantification of the collective motion.

Cooperative particle dynamics is one of the most characteristic features of the dynamics of glass-forming fluids[87, 144, 145]. As a first step in identifying collective particle motion, we must identify the ‘mobile’ atoms in the system[87]. In glass-forming liquids, the ‘mobile’ atoms are defined by comparing the self-part of the van Hove correlation function $G_s(r)$ to an ideal uncorrelated liquid exhibiting Brownian motion where $G_s(r)$ reduces to a simple Gaussian function by the central limit theorem. The interacting fluid $G_s(r)$ has a long tail at large distances r, pointing to the existence of particles of relatively high mobility in the interacting particle system. A comparison of this kind generally to a crossing of the interacting and non-interacting $G_s(r)$ curves, and the mobile particles are then naturally defined as those atoms whose displacement exceeds the crossing point distance after a characteristic diffusive decorrelation time Δt. However, in the GB regions of a polycrystalline material or on the NP surfaces, the van Hove correlation function is no longer a single-peaked function, but rather has *multiple peaks* centering at successive nearest-neighbour distances. We then conclude from our observation of a multiple peaked $G_s(r)$ that the surface of the NPs is something like a polycrystalline material constrained to the surface of a spherical shell. Since 'mobile' atoms are essentially those particles moving a distance $r(t)$ larger than the typical amplitude of an atomic vibration after a decorrelation time Δt, but smaller than a particular distance, we mathematically identify these particles by a threshold atomic displacement condition, $ar_0 < | r_\mathrm{i}(\Delta t) - r_\mathrm{i}(0) | < br_0$, involving the first nearest neighbor distance r_0, and coefficients a and b can be determined from the van Hove correlation function.

The identification of correlated atom motion requires a consideration of the *relative displacement* of particles. Collective atom motion means that the spatial relation between the atoms is preserved to some degree as the atoms move. Specifically, the reference mobile atoms i and j are considered to be within a collective atom displacement string if they remain in each other's neighborhood and we specify this proximity relationship by, $\mathbf{min}(\,|\,r_i(\Delta t) - r_j(0)\,|\,,\,|\,r_i(0) - r_j(\Delta t)\,|\,) < 0.43r_0$. The criterion of $0.43r_0$ is selected because it is slightly smaller than the midway of the nearest atom distance. Atomistic simulations of glass-forming liquids indicate that the distribution of string lengths $P(n)$ is an approximately exponential function of n, $P(n) \sim \exp(-n / <n>)$.

3 Spontaneous Shape Fluctuations in Single Small Nanoparticle[*]

3.1 Introduction

Previously,[88] we focused on relatively large Ni NPs having a diameter of about 4 nm (N = 2899 Ni atoms) where large-scale NP shape fluctuations were not conspicuous. For these larger NPs, we found that the interfacial dynamics (at elevated catalytically relevant temperatures) was characterized by the formation of a 'pre-melted' NP interfacial layer having a relatively high atomic mobility, while the crystalline NP core retained the ordering of a crystal. Although the structure of the interfacial layer of these surface-melted NP can be characterized as 'amorphous', the dynamics of this 'liquid-like' layer was found to be highly heterogeneous, closely resembling the dynamics of glass-forming liquids[87, 144] and the grain boundaries of crystalline materials.[100] In particular, the molecular dynamics of the interfacial layer of the NPs, and other 'glassy' materials involving strongly interacting and disordered materials, is characterized by string-like

---

[*] Materials in this chapter has been published.

Reproduced by permission from Y. Yang, H. Zhang and J. Douglas, *ACS Nano*, **8**, 7465-7477 (2014). Copyright 2014 American Chemical Society.

Most of the content in the article remains in this chapter, while some research background is included in Chapter 1, some content about the EAM potential in the 'Simulation Methodology' is included in Chapter 2, "2.2 Potential" and the content of the 'Conclusion' is included in Chapter 6, "6.3 Suggestions for the Future Work".

The direct link for the published article is http://pubs.acs.org/doi/pdf/10.1021/nn502767t correlated particle movements, i.e., 'strings'. [142, 143] A recent study provided similar evidences for the collective atomic dynamics in raft-like lipid membrane[146], with the thickness of 5 nm. In our previous work, we also found that the 'fragility' of the amorphous interfacial layer dynamics, a measure of the relative strength of the temperature dependence of diffusion and relaxation processes,[143, 145, 147] could be tuned by altering NP size and by alloying the Ni NP with other metallic species such as Au, Ag, Pt, etc.,. The recognition of these excitation structures provides insight into how the interfacial dynamics of NPs can be modulated with additives and by varying the geometrical structure of the nanomaterial. We note that this type of collective particle motion has been directly observed experimentally, e.g., in ultrahigh resolution images of amorphous metal films of Ge,[12] particle tracking measurements on colloidal hard sphere suspensions, [148, 149] and by imaging the grain boundaries of colloidal crystals.[150, 151]

In the present work, we explore NP shape fluctuations in a single isolated Ni NP having a radius, $r \approx 1$ nm. In particular, we find that Ni NPs having $r = 0.8$ nm undergo considerable shape fluctuations over an appreciable temperature (T) range near the melting temperature (T_m), while larger NPs ($r > 1$ nm) fluctuations show little departure from an average spherical particle shape. We examine T_m and other basic properties of the NPs before investigating their surface, interfacial and inner NP core dynamics in the vicinity of T_m. Specifically, we investigate fluctuations in the NP potential energy, Debye-Waller factor, and shape changes of the NP through determination of the radius of gyration tensor of the NP as a function of time. We find that shape fluctuations are accompanied by large displacements of the central atoms within the NP that trigger the large-scale particle shape fluctuations. These shape fluctuations are facilitated by string-like collective motion taking a novel form, the migration of atoms through the *center* of the NP. In other words, when the NPs become critically small in size the string-like collective molecular motion observed in the interfacial region of larger NPs (See Figure 2 of Zhang *et al.*[88]) no longer remains localized to the NP interfacial region. Instead, the strings 'short-circuit' by passing through the NP center -- a phenomenon that is highly disruptive to NP shape.

3.2 Simulation Methodology

We utilize the Voter-Chen EAM potential for Ni NP simulations since it yields the correct elastic constants, vacancy formation energy, cohesive energy, lattice parameter, interatomic spacing (properties to which it was fitted) and reasonable interface properties for Ni[152], for example, the calculated surface energy for (100), (110), and (111) are 1760 mJ/m^2, 2002 mJ/m^2 and 1632 mJ/m^2, respectively, compared to experimental value for average face is 2280 ± 300 mJ/m^2. More importantly, the tendency of surface energy variation based on the specific surfaces, i.e., γ (110) > γ (100) > γ (111), is in good agreement with results of other EAM potentials[153]. In addition, the surface relaxation simulation using this potential also shows that the percentage changes in interlayer spacing are in reasonable agreement with both LEED data and theoretical data[154]. Therefore, it is expected the Voter-Chen EAM potential for Ni is able to yield reasonable results on nanoparticle with large surface-to-volume ratio.

The Ni NPs were initiated from an approximately spherical shape and a perfect local fcc structure. The NPs were first relaxed at room temperature for 1.5 ns with zero angular and linear momentum values. Note that while we start the NP with the fcc crystal structure of the bulk crystal, the NP for $N = 55$ quickly transforms to an icosahedral solid, which is the equilibrium structure of these smaller NPs.[37, 155-158] In contrast, the crystal structure is maintained in the NP core for relatively large NPs.

The NPs were heated at a rate of 100 K / ns from room temperature ($T = 300$ K) until the NPs melted. Correspondingly, the melted NPs, obtained from the above heating history, were cooled down also at a rate of 100 K / ns from their melting conditions to room temperature. Although this rate of heating/cooling is relatively slow from the standpoint of molecular dynamics simulation, it is orders magnitude higher than the rates normally encountered in experimental studies. In order to probe kinetic processes that cannot be observed while heating at a continuous and high rate, we also performed 'isothermal' heating studies. Isothermal simulations were performed where T was changed from 950 K to 1250 K in discrete jumps of 50 K where T was held constant for 3 ns after each T-jump.

We monitor the total potential energy E_{tot} for two purposes: (1) it provides a criterion for determining the transition between solid and liquid states; (2) it is an important property for characterizing the dynamics of the NPs because T_m, estimated from the T dependence of E_{tot}, allows us to define a reduced temperature T / T_m for comparison of NPs having different sizes.

We consider standard measures of dynamic heterogeneity in glassy materials such as non-Gaussian parameter α_2. The radius of gyration R_g is defined by,[131, 132]

$$R_g^{\ 2} = \frac{1}{N}\sum_i \left(r_i - r_{mass}\right)^2 \tag{3-1}$$

where r_{mass} is the center of mass and this quantity can be generalized by defining moments about different coordinate directions to define the R_g tensor.[133]

The simulations of the NP dynamics below reveal a basic event in the NP dynamics of significance in understanding the dynamics of these particles. At intermittent times, particles at various initial positions within the NP first emerge at the NP boundary and we define a dimensionless variable ρ allowing for the identification of these events,

$$\rho = \frac{1}{r_0}\left|r_i - r_{mass}\right| \tag{3-2}$$

where r_i is the position of specified atom i, r_0 is the initial radius, and r_{mass} is the center of mass of the NP. If $\rho \to 0$, the i^{th} atom occupies the central position within the NP, while $\rho = 1$ indicates that this particle has emerged at the NP surface.

3.3 Results and Discussion

3.3.1 Initial Qualitative Look at 'Small' Nanoparticle Shape Fluctutaions

In previous work,[88] we studied Ni NPs having an average particle diameter > 4 nm and found no large scale NP shape fluctuations for such large particles at any T. Figure 1a illustrates this type of NP as a reference point in our discussion below. We see that while there are small-scale NP fluctuations in the interfacial layer thickness, the overall NP shape does not change appreciably from a roughly spherical shape. The melting temperature T_m for this reference 'large' NP equals $T_m = 1500$ K, which can be compared with $T_m = 1624$ K for a bulk Ni crystal[159] ($N \rightarrow \infty$), based on this potential.[88] The Voter-Chen potential is evidently not optimized to reproduce the bulk T_m since the observed T_m for Ni is almost 100 K higher than our simulation estimate, $T_m(\text{bulk}) = 1728$ K. We do not expect this discrepancy to affect our qualitative conclusions regarding the nature of shape fluctuations in small NPs, however.

We now contrast the shape fluctuations dynamics of these relatively large NPs to those of a 'small' NP having a radius < 1 nm (Such NPs might be better termed 'clusters' rather than NPs, but this is within size range found in catalytic applications of NPs). It is apparent from Figure 1b that our 'small' Ni NPs indeed exhibit large-scale shape fluctuations reminiscent of those found previously for Ar atomic clusters by Berry and Wales, where the Ar interaction was described by a simple LJ potential.[160, 161] Given the insensitivity of this fluctuation phenomenon to the type of intermolecular interaction, we expect these NP shape fluctuations to be a *generic* phenomenon, extending perhaps to organic nanoparticles, i.e., proteins.

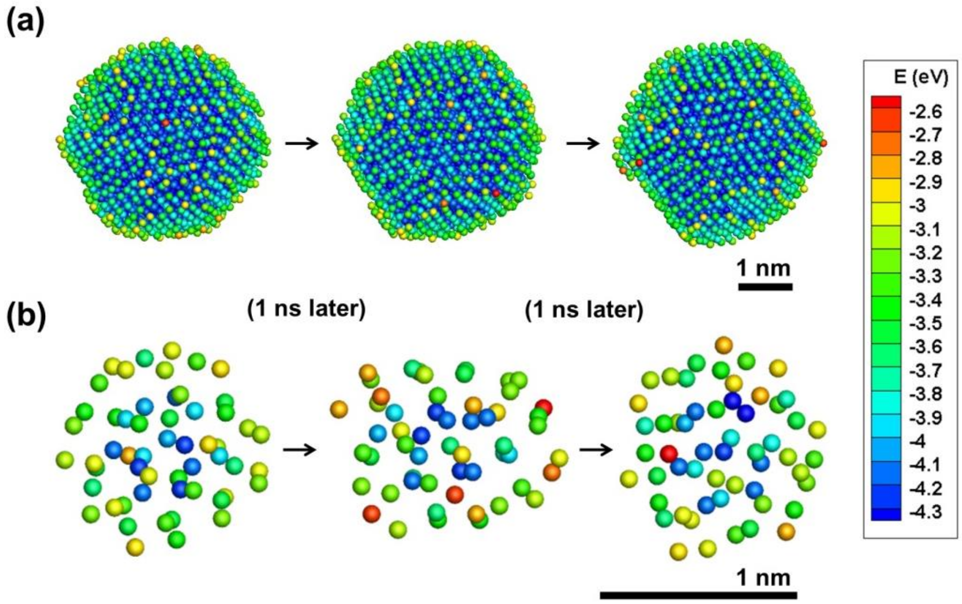

Figure 3.1 NP shape evolutions for (a) $N = 2899$ at 1200 K (0.8 T_m) and (b) $N = 55$ Ni NPs at 1200 K (0.98 T_m). The shape fluctuations and string-like collective atomic motion are largely confined to the interfacial layer in the large NP. In contrast, large shape fluctuations arise at equilibrium in the smaller NP associated with coordinated displacements of the Ni atoms through the center of the NP. Atoms are colored by potential energy.

The shape fluctuations in these small NPs apparently involve significant collective atomic motion within the center of the NPs so their dynamics is *qualitatively different* from larger NPs (Figure 3.1a) where collective motion in the form of strings (the atoms move sequentially in this illustrative case, but string-like motion does not generally have this character in glass-forming liquids and we expect that the coherence of collective motion depends on temperature generally) was prevalent in the 'pre-melted' NP interfacial layer (See Figure 2 of Zhang *et al.*[88]). This singular form of collective motion was also noticed in earlier simulations of the dynamics of small Ar clusters,[162] Au clusters[104] and some other transition-metal clusters[105] (i.e., Ag, Au and Ni) where the cooperative motions was found to have a sequential nature. The principal focus of the present work is the quantification of the shape fluctuations and its relation to string-like atomic cooperative motion within small NPs, where the detailed nature of the collective motion, sequential or otherwise, is not considered because this will require many further computations. This first effort requires a characterization of the NP thermodynamic state so that comparisons of NPs having different size can be made at the same absolute temperature, 1200 K, which to $N = 2899$ is of its 0.8 T_m, and to $N = 55$ is of its $0.98T_m$ (the T_m will be detailed below).

3.3.2 Nanoparticle Melting Temperature T_m

All of our NPs are simulated starting from a particle having a bulk Ni fcc lattice structure, but with specific cut-off radius where the surrounding is a vacuum. The current study considers NPs with 55 atoms (with diameter $d = 1.07$ nm), 123 atoms ($d = 1.40$ nm), 135 atoms ($d = 1.45$ nm) and 369 atoms ($d = 2.03$ nm), but we particularly focus on the small Ni NP having 55 atoms. Although we started our simulations with particles having an fcc lattice structure, the small NPs quickly transformed into icosahedral solid structures when $N < 170$ atoms. The observation that small metal NPs adopt low icosahedral or other non-crystallographic symmetries has been discussed in numerous experimental and computational studies. The reason is that the potential energy in this type of particle packing is lower than the fcc packing of the bulk crystal. Bulk crystals simply cannot exist in such dense packings and at some point ordered form must make a transition from icosahedral to thermodynamically ‘acceptable’ crystal packing, which is fcc for Ni and many other metal atoms. For instance, Davis *et al.* [163] showed that 13-particle Ar clusters possess icosahedral symmetry below melting temperature. Sun and Gong [40] have demonstrated that small Al cluster exhibit magic number clusters, i.e., Al13, Al55 and Al147, in which an icosahedral-like symmetry describes the lowest energy structure; however, an octahedral symmetry can be a stable structure for other non-magic number metal atom clusters. In addition, we expect the starting fcc crystal structure has limited effect on our simulation results. Although in the ‘small’ NP size regime (e.g., $N < 200$ atoms), a local fcc structure has a relatively high energy and is energetically unfavorable compared to the Mackay icosahedra[103, 104], the thermal energy is high enough in the regime (T in the range from 0.8 T_m to T_m) we study to quickly overcome the energy barrier between the fcc and icosahedra structures, which brings the system from the highly non-equilibrium fcc state to equilibrium or near-equilibrium state. However, the starting structure effect must certainly become relevant at lower T where the probability of getting trapped in a non-equilibrium state is much higher.

We next determine T_m to facilitate the comparison of the dynamics of NPs having different sizes. The NP potential energy changes upon heating, as illustrated in Figure 3.2a, and T_m is determined as the point where the NP becomes completely liquid, signaling a transformation from an ordered solid to a disordered liquid. The loop-like potential energy curve obtained from a heating and cooling cycle provides evidence for ‘dynamic coexistence’ in these small NPs, a phenomenon investigated previously.[164-168] While this coexistence phenomenon occurs for several cases considered (N =135, N = 369), for N = 55 and N = 123, the heating and cooling curves continuously go up and down within the transitional T range. Under these conditions, the differentiation of the solid and liquid states becomes ambiguous, motivating the introduction of the term ‘overlapping’ regime to describe this ‘twilight zone’ NP state. With a decrease of NP size, the melting and cooling curves change from dynamic coexistence to the ‘overlapping’ regime. NP configurations corresponding to N = 55 are shown in Figure 3.2b, where we see an odd form of melting in which the NP transforms from a crystal having icosahedral symmetry solid to a disordered liquid during heating and freezes into an icosahedral symmetry solid upon cooling. Meanwhile, the change from dynamic coexistence to phases in contact has been analyzed in detail in previous work and is well understood[169]. In small systems the energetic cost of the interface is too large, and dynamic coexistence results, which is also characterized by an S-bend in the microcanonical caloric curve[169].

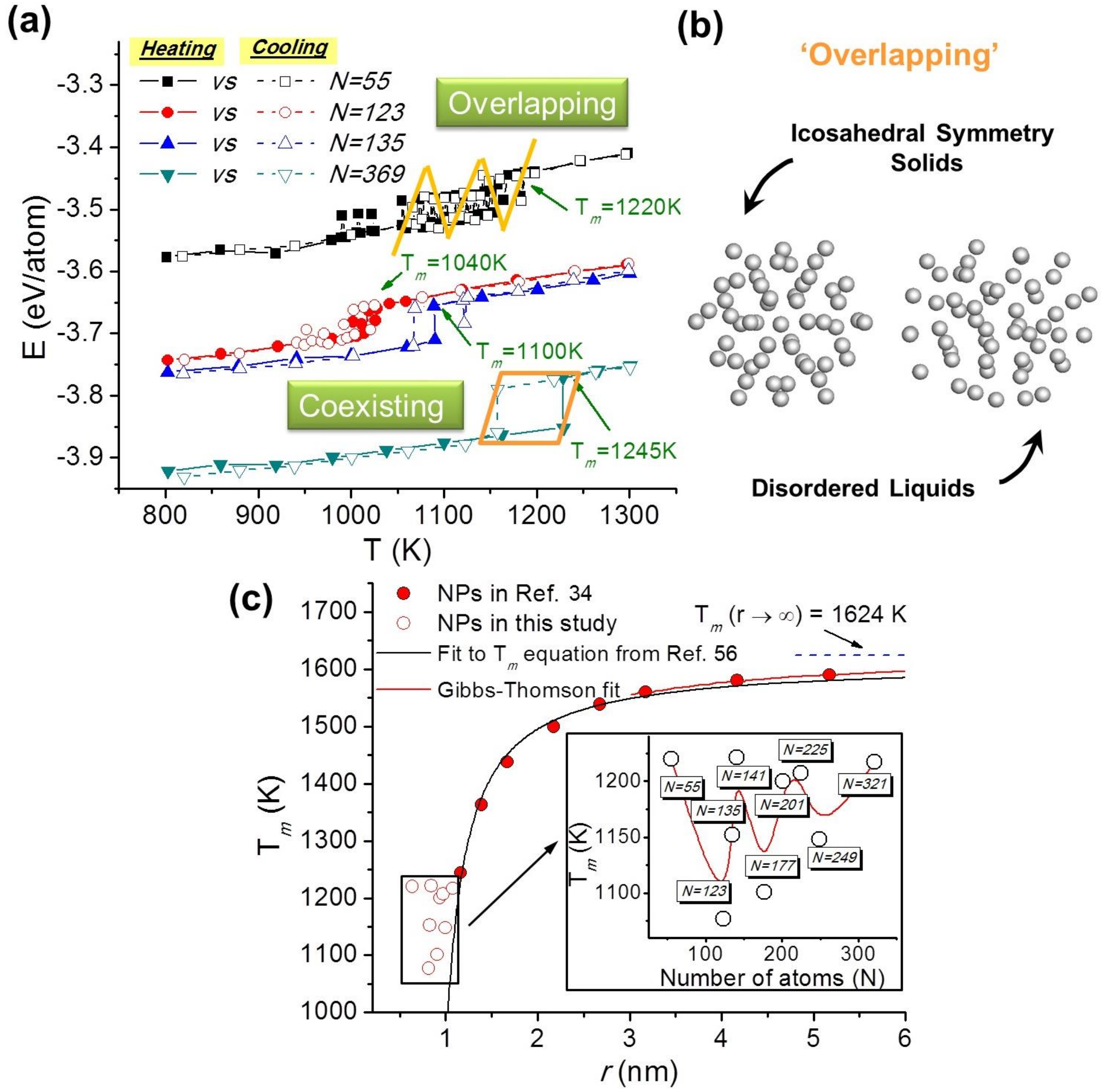

Figure 3.2 (a) Ni NP potential energy dependence on *T* for *N = 55, N = 123, N = 135* and *N = 369*; (b) NP configurations corresponding to solid and liquid states (c) Melting point as a function of NP size.

Our previous studies of T_m as a function of NP size indicated that ΔT_m varies approximately inversely with the NP radius when the NPs are relative large ($N > 10{,}000$ or

6 nm), conforming to the expectations of the Gibbs-Thomson relationship.[88, 170] However, even this earlier work indicated deviations from continuum theory estimates of T_m when the NPs became relatively small ($N < 700$ or 2.5 nm), but these deviations were left unexplained at the time (See Figure 1 of Zhang *et al.*[88]). Here these T_m plots of T_m are updated (Figure 3.2c) to include data for smaller NPs.

To gain an insight into the onset of this non-continuum NP regime, we first plot the previous Gibbs-Thompson curve in Figure 3.2c for reference. Then we attempt a fit of our extended T_m estimates to a melting model that addresses observed NP size-dependent changes in the amplitude of the Debye-Waller factor[28], in conjunction with the Lindemann melting criterion,[171] to estimate T_m. This model indicates a modified scaling for the T_m shift with NP radius., $T / T_m \sim \exp(A / (r - R_\mathrm{c}))$, where A is a constant and R_c is a 'critical NP radius' and recovers the continuum limit scaling of T_m (r) when the NPs are larger than $N = 141$ or 1.5 nm. Although this modified model of T_m also breaks down when the NPs become very small, the critical radius R_c obtained from a numerical fit of our T_m data to this model corresponds closely to the scale at which large NP shape changes become prevalent in our simulations.

The inset of Figure 3.2c shows the more complicated changes in T_m with the number of Ni for NPs around R_c. In particular, T_m oscillates for 'small' NPs ($N < 369$), revealing a 'magic number' phenomenon associated with appreciable changes of the NP free energy with the addition of individual atoms.[172] This is a generic feature of small NPs[173] that is seen both in experiments and simulations[172, 174]; the peaks in the T_m values normally occur close to the atomic number N values (13, 55, 147, 309, …) at which the NP form highly stable Mackay icosahedron structures at low T.[155, 175] These magic number T_m values are thus the consequence of the formation of well-packed small clusters at low temperatures for particular numbers of atoms.[173]

3.3.3 Potential Energy and Debye-Waller Factor

Figure 3.3 shows fluctuations in E_{tot} (Figure 3.3a) and $<u^2>$ (Figure 3.3c) as a function of t and for a range of T. At relatively low T, e.g., 950 K (0.78 T_m) and 1000 K (0.82 T_m), the fluctuations in E_{tot} and $<u^2>$ are small, reflecting the stability of the NP. At relatively high T, e.g., T = 1250 K and $T / T_m = 1.02$, E_{tot} and $<u^2>$ both exhibit large fluctuations. These fluctuations can be seen more clearly in Figure 3.3b, with the representative configurations illustrated for solid and liquid states. In the coexistence range, which is between 1050 K (0.86 T_m) and 1100 K (0.90 T_m), E_{tot} and $<u^2>$ fluctuate between two distinct energy states in the T regime as the NP undergoes significant shape changes. Some intermittent transformations between these solid and liquid like dynamic states occurs at almost all T simulated. We next consider how these shape fluctuations are related to fluctuations in E_{tot} and $<u^2>$.

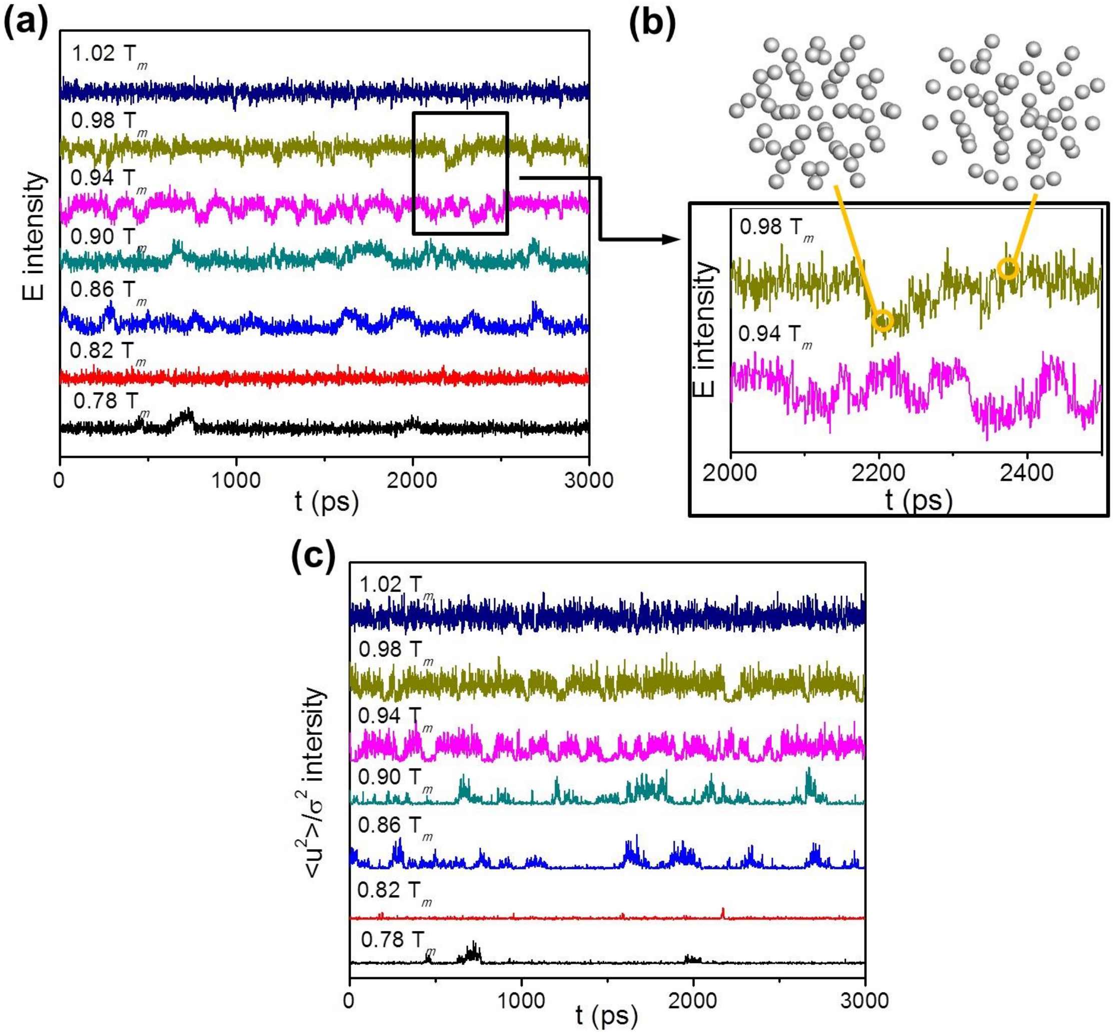

Figure 3.3 (a) Ni NP potential energy, (b) magnified region and (c) reduced DWF $\langle u^2 \rangle$ / σ^2 on dependence on T for $N = 55$.

3.3.4 Correlation of Nanoparticle Shape and Energy Fluctuations

We focus on the representative temperature 0.86 T_m for the $N = 55$ Ni NP in the overlapping regime. In Figure 3.4, we observe two-level E_{tot} (t) fluctuations that are directly correlated with the particle displacement fluctuations and with fluctuations in the NP radius of gyration, R_g^2. The baseline values of these properties are symptomatic of the solid state while the peak values of these properties are characteristic of the NP 'liquid state'.

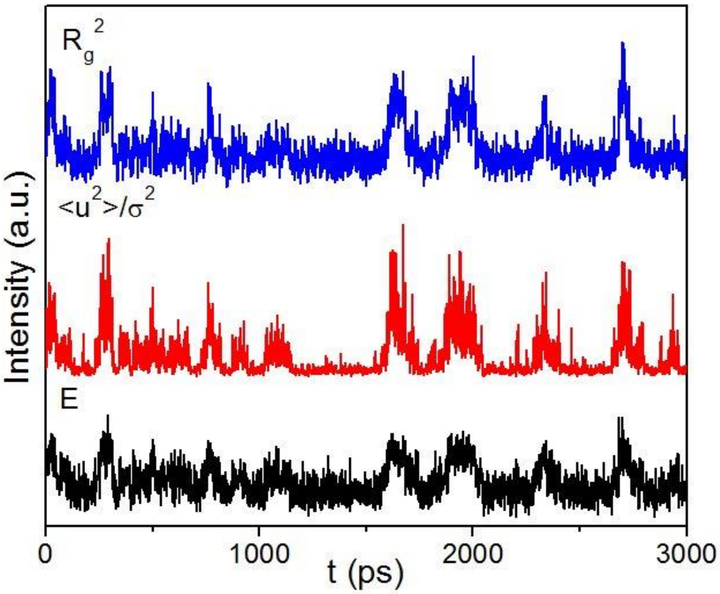

Figure 3.4 Potential energy, relative $\langle u^2 \rangle$ and R_g^2 as a function of t for $T = 0.86\ T_m$ and $N = 55$.

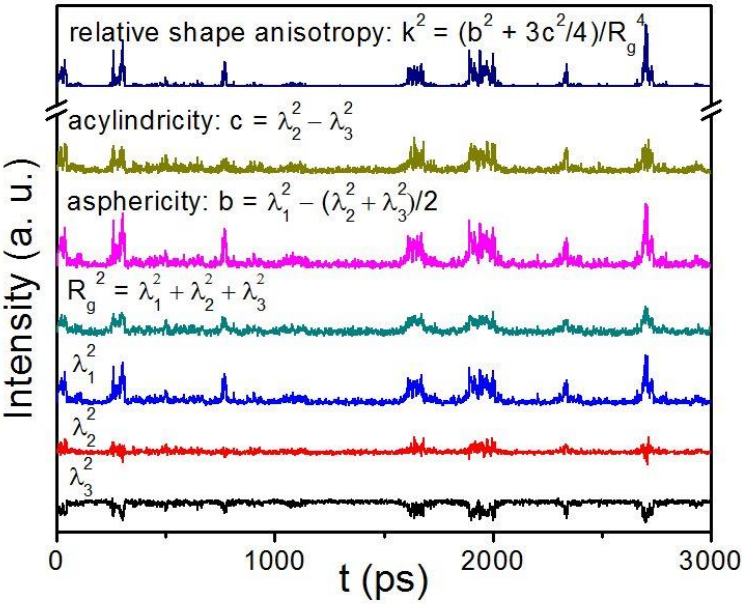

Figure 3.5 Dependence of R_g and shape factors of a Ni NP on *t* for $T = 0.86\ T_m$ and $N = 55$.

We quantify the NP shape fluctuations accompanying NP state changes through consideration of the NP shape parameters *b*, *c*, and k^2 defined above and these properties are shown in Figure 3.5. At particular time events at which the particle starts changing its shape, the λ_i along each direction (i = 1, 2, 3) suddenly become unequal. Baselines in *b* and *c* then occur when the NP returns to its original near-spherical shape. The shape factor k^2 quantifies the NP shape anisotropy that accompanies these 'quake' events. Evidently, the shape fluctuations are directly correlated with the NP energy and DWF fluctuations.

3.3.5 Molecular Dynamic Origin of Nanoparticle Shape Fluctuations

Now that we have established that small NPs undergo striking shape changes below their melting temperature, it is natural to consider what role collective atomic motion might play in this process. This leads us to focus on the central position of the NP for N = 55 where the scale of atomic motion can be peculiarly large for small NPs[176] (Jellinek observed that $<u^2>$ in the center of the particle can actually be *maximal* in the dynamic coexistence regime, reflecting the fact the central particle is constantly being kicked out of the cluster center[177]). As explained in the methodology section, we calculate the mean first-passage time for atoms to reach the surface of the NP. The value of ρ for any given atom provides information on the relative rate at which particles within the NP emerge on the NP surface as a function of various starting points within the NP.

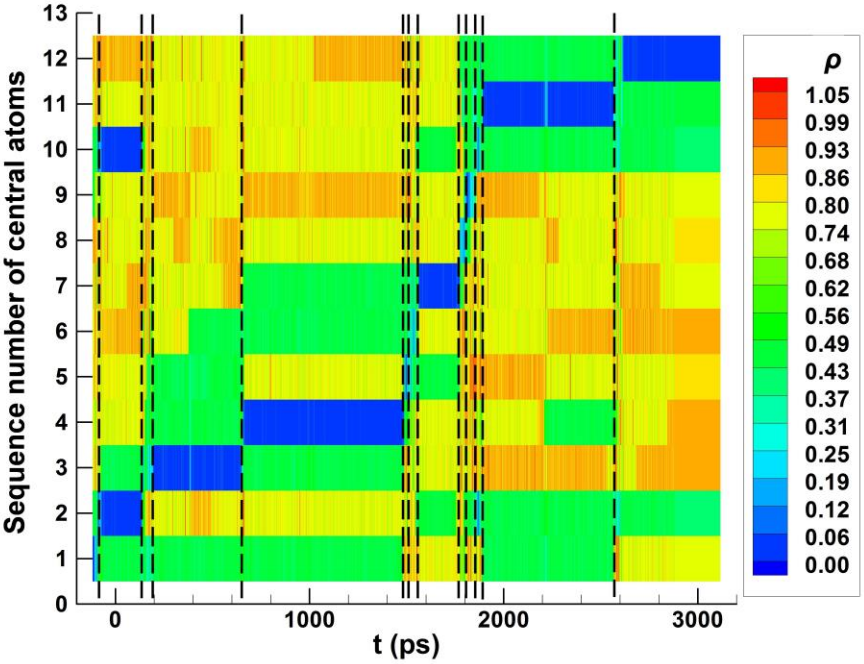

Figure 3.6 Dynamic atomic positions of sequential central atom positions as a function of *t* for 0.86 T_m and $N = 55$.

Within the time period of 3000 ps, we show in Figure 3.6 the evolution of the atomic position of the central particle as it makes its way to the NP surface. The central atomic position changes 12 times in this time period and these events are labelled 1 to 12 in Figure 3.6. Note "2" and "10" are the actually the same atom, meaning this atom moves in this way twice so there is some back and forth motion of the atoms. The displacement instants are marked by a dashed line.

To clarify how the NP shape change are synchronized with the displacement of the central NP atoms, we created an animation of the NP evolution for the time period between 1800 ps to 1900 ps. In the movie, the central atoms labelled as "7", "8" and "9" are based on the corresponding numbers in Figure 3.6. This visualization shows the colored atom “7” initially at the NP center and then “8” and “9” follow its movement to the NP surface, followed by a dramatic shape change.

3.3.6 String-like Collective Motion

What kind of atomic motion underlies the NP shape fluctuations? Are they moving incoherently, coherently like a crystal or does the motion has some ‘in-between’ or ‘mixed’ character as in former simulations of the interfacial dynamics of larger NPs where the motions had a string-like form? To answer these questions and to quantify the collective nature of the motion in these NPs we look for string-like collective motion, a characteristic mode of molecular displacement in strongly interacting disordered materials. Previous studies also considered the precise nature of the string-like "correlated" motion, where two extremes seem to exist, sequential or concerted movement, and these can be distinguished by suitable analysis of the pathways[178]. It indicates that highly cooperative large-scale changes of shape that correspond to single transition states break down into a series of transition states with intervening local minima for larger systems. As in our former studies, this analysis requires the determination of the non-Gaussian parameter α_2 and van Hove correlation function $G_s(r, t)$ before the extent of collective motion can be inferred and these details for the present system are repeatedly described in Chapter 2 as has been described in previous publications.[88, 141, 143]

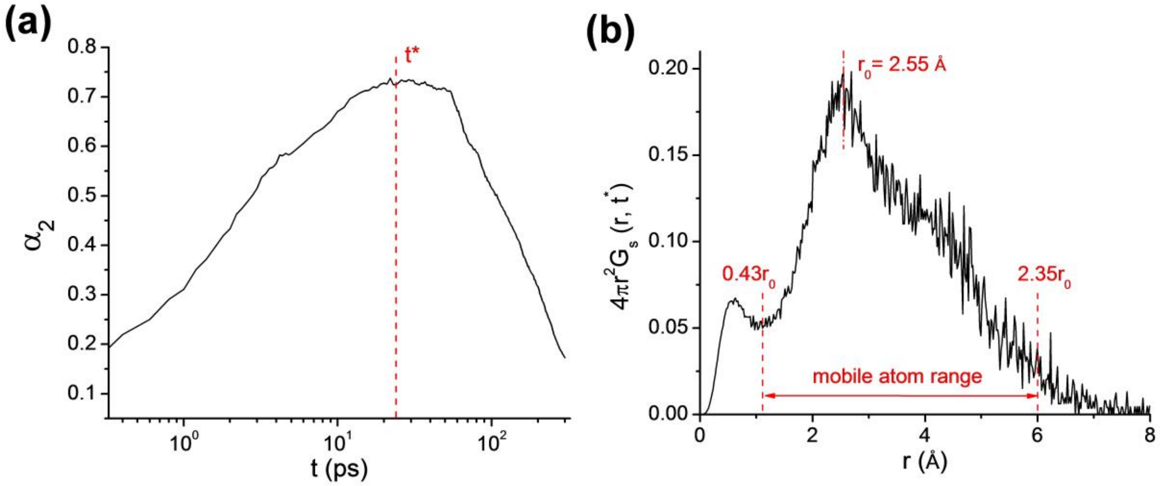

Figure 3.7 (a) Non-Gaussian parameter NGP (α_2) and (b) van Hove function G_s (r, t^*) for $N = 55$ at $T = 0.86$ T_m.

The non-Gaussian parameter α_2 and G_s (r, t) for the $N=55$ NP at 0.86 T_m are shown in Figure 3.7. The peak position of α_2 occurs at 24 ps and substituting t^* into G_s (r, t) reveals a classic hopping peak at 2.55 Å. There is then clear evidence of dynamic heterogeneity in the dynamics of the Ni atoms in these small clusters. The “mobile” atom range is fixed by the dashed line and ranges from 0.43 r_0 to 2.35 r_0.

If mobile atoms in the form of string-like cooperative atomic rearrangements are responsible for the peak in α_2 and the hopping peak in G_s (r, t), as in previous studies of larger Ni NPs, then we should see particles moving, but staying within proximity of each other rather than wandering off on their own. The extent of string-like collective motion is then determined and the results of this analysis are shown in Figure 3.8. The majority of collective motion events observed in the current study is sequential, but we need to be careful in drawing general conclusions about the nature of the collective motion from these limited observations. As can be seen, the relative shape anisotropy, the number of mobile atoms, the number of atoms involved in the string, and the string length peak positions all match each other rather well. String-like collective motion clearly accompanies the NP shape changes.

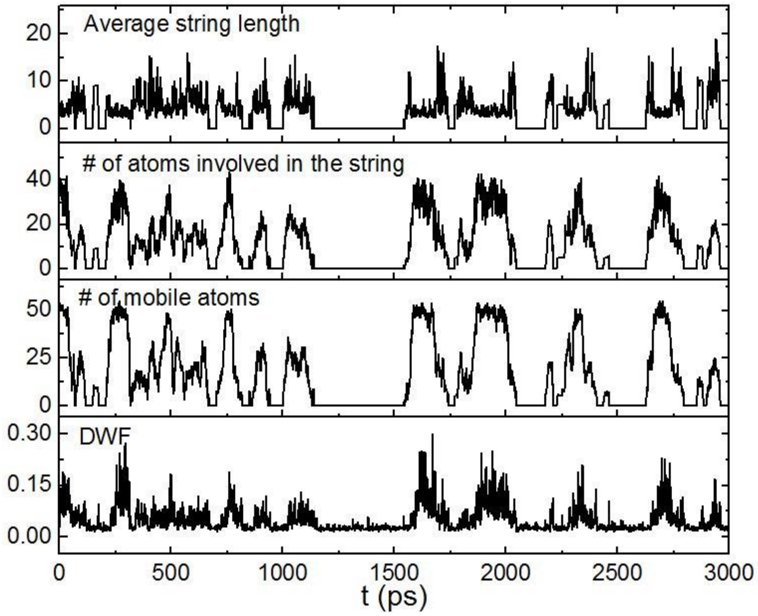

Figure 3.8 Numbers of mobile atoms, string atoms and string length compared with $<u^2>$ as a function of t for $N = 55$ and $T = 0.86\ T_m$.

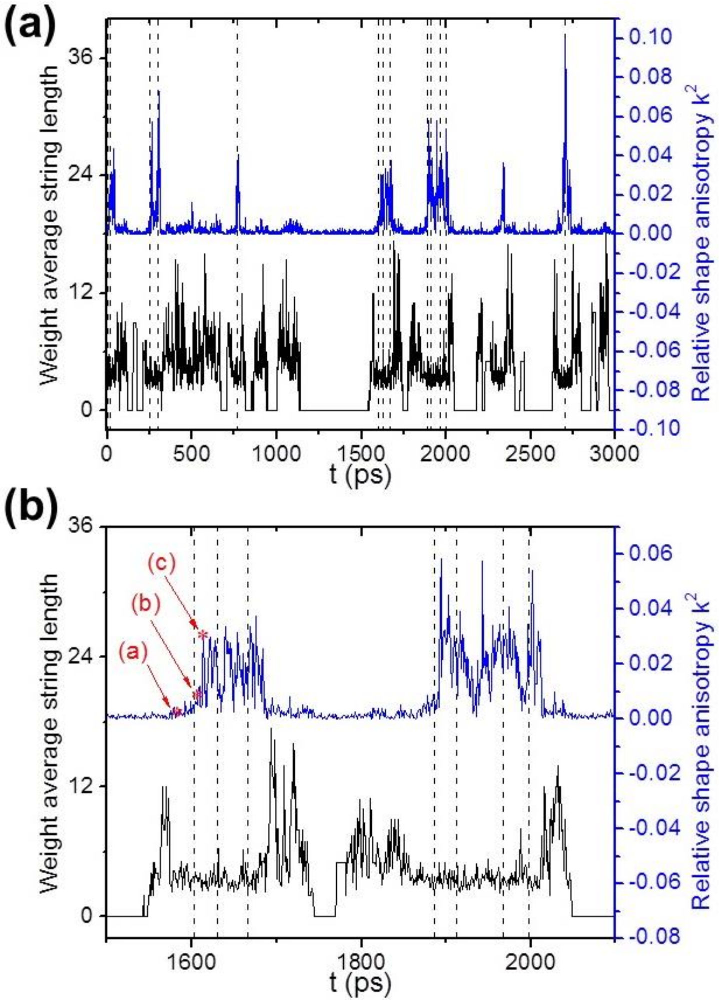

Figure 3.9 (a) Comparison of string length *L*, central atom displacement and shape anisotropy, k^2 and (b) details of those from 1500 ps to 2100 ps.

Further comparison for the string length with fluctuations in the shape anisotropy (shown by dashed line in Figure 3.6) is presented in Figure 3.9a. Apparently these events of coordinated atomic movement do not happen at exactly the same time as the shape fluctuation events. Instead, we see that the longest strings appear just before and after the peaks in the NP. Short strings occur without large-scale particle shape fluctuations. Further, there is little string activity when the particles are in their solid state, as found in our previous paper on larger NPs.[170] The longer strings having an erratic fluctuating length and are strongly correlated with the NP shape fluctuations. These longer strings are highly reminiscent of fluctuating strings found the interfacial region between ordered and ordered particle regions of a larger Ni NPs (≈ 2 nm radius; N = 2899) under *non-equilibrium* melting or freezing conditions.[141] The string-like collective motion apparently facilitates the local state transformation from the 'liquid' or dynamically 'mobile' and the 'solid' to 'dynamically immobile' particle states.

A more detailed examination of this interconversion process in the time regime between 1500 ps to 2100 ps is shown in Figure 3.9b. Meanwhile, in order to make a clearer demonstration for this process, a comparable video shows that after long strings form in an initially solid-like NP configuration no shape change arise, while the number of atoms involved in the string can have a large value as large as 40. The central atom displacement occurs only when the number of atoms involved in the string is large, but the string length is relatively small, pointing to a particular significance for intermediate size strings in the shape transformation process. The shape anisotropy parameter k^2, step by step, reaches a maximum in three stages corresponding to 1583 ps, 1607 ps and 1614 ps. These events are labeled as (a), (b) and (c) in Figure 3.9b.

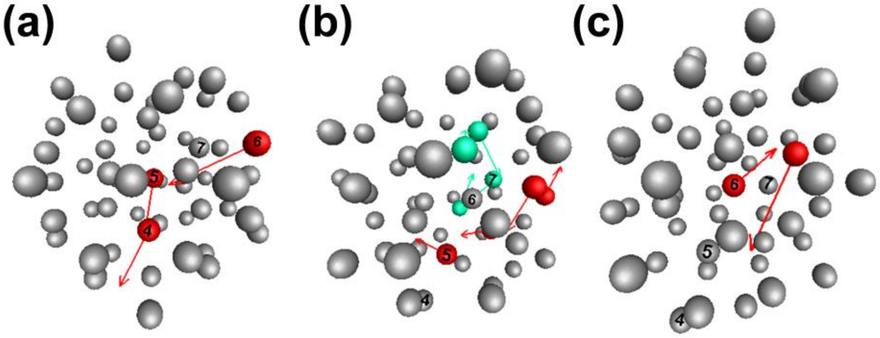

Figure 3.10 Configurations of $N = 55$ Ni NP at $T = 0.86\ T_m$ for (a) 1583 ps, (b) 1607 ps and (c) 1614 ps.

We can now effectively describe how the string motion actuates the cluster shape changes. Figure 3.10 shows those three configurations at the three stages of time development mentioned above. This perspective view helps us distinguish atoms at the front and at the back of the NP. Different colors represent different string clusters involved in the collective motion where only the strings include central atoms are highlighted. The three central atoms are labeled "5", "6" and "7" subsequently, with another string atom labeled "4", according to the number depicted in Figure 7. In the first window, "6" is on the outer surface, preparing to replace atom "5" and this exchange is orchestrated by a string collective displacement, the positions and configuration of which are shown in the second time window at 24 ps (the time t^* at which the non-Gaussian parameter peaks). In this snapshot, atom "5" initiates another string movement and atom "7" starts then participates in a string action. In the third time window, where we observe the largest shape change, the central atom "6" moves through the initiation of a new string and similar string motions and shape changes occur during other time periods. The string motion is apparently 'initiated' by activating particles in regions of high mobility and presumably high local instability; in practice, this can mean regions of *high density* and *low free volume* rather than regions of low density and high free volume. Free volume is not a general correlate with mobility on a local scale, a point made before in glass-forming liquids.[87, 144, 178, 179]

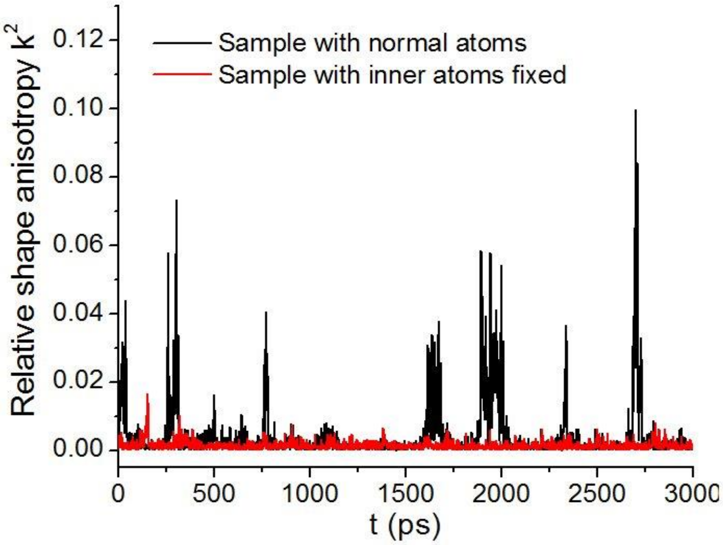

Figure 3.11 Comparison of relative shape anisotropy for unconstrained Ni NP having N = 55 and $T = 0.86\ T_m$ and a core-constrained NP.

Finally, to confirm that the shape changes are directly related to the large displacement of the central atom of the NP, we carried out another simulation where the 5 atoms in the center of the NP are fixed in position by setting their temperature to 0 K and representative simulations of this experiment are shown in Figure 3.11. Almost no shape anisotropy arises in the NPs when the core is fixed in this way. The shape changes reflect the disruptive effect of the central atom migration to the surface in our small NPs.

3.4 Conclusions

We investigate NP shape fluctuations in a single Ni NP having a radius smaller than 1 nm using molecular dynamics simulation. Our representative small (0.8 nm) Ni NP undergoes considerable shape fluctuations in a wide temperature range near the melting temperature T_m. An examination of fluctuations in the NP potential energy, Debye-Waller factor, and measures of NP shape suggest that the shape fluctuations are accompanied by large displacements of the central atom within the NP that trigger the large-scale particle shape fluctuations. Once triggered, the coordinated atomic motion driving atoms from the NP core to the surface drives the large-scale shape fluctuations of the NPs.

4 Coalescence of Multiple Small Nanoparticles

4.1 Introduction

The sintering and coalescence of nanoparticles (NPs) becomes the challenge for the applications of the catalysis. Once the NPs are merged together as a whole, the catalysis efficiency is largely decreased. As mentioned before in Chapter 1, the ‘surface melting’[12] and ‘quasi-liquid layer’[13, 14] has been played an essential role for the NP sintering and coalescence. However, the atomic motions in the liquid-like layer, and the fundamental local structure change as well as the crystallization during the coalescence process have not been investigated.

In the present chapter, we look at sintering process for several *N55* NPs, how the inherent fluctuation is reduced and what the dominant interfacial dynamics becomes for the NP coalescence process. We first investigate the relative shape anisotropy and the local structure that is characterized using the Honeycutt-Andersen (HA) index. The evolvements of the local fcc structure, the local icosahedral structure and the liquid-like structure are discussed. Then, the cluster formation process for the crystallization of the pure fcc structure is observed. Finally the atomic movement during the sintering process is discussed.

4.2 Simulation Methodology

The *NVT* ensemble was employed, where the constant temperature was maintained by Nosé-Hoover method[124, 125]. The periodical boundary condition was utilized. The simulations of coalescence of multiple NPs were performed in the cases of 4, 6 and 8 well-equilibrated *N55* NPs, in which the NPs were initially located at the corners of tetrahedral, octahedral and cubic geometry, respectively. The nearest separation distance between the entire NPs is 3Å, which was slightly smaller than the valley distance of 3.09 Å between the first-nearest neighbor and second-nearest neighbor. The orientation was the same for each NP.

The initiation of the single NP could be found in our previous study[180]. Those individual Ni NPs were relaxed for 3 ns at different temperatures of 900K, 950K, 1000K and 1050K. Accordingly, the simulations of coalescence of NPs were kept at the same temperature as an isothermal sintering process. In addition to the sintering of multiple NPs, the isothermal processes for single NPs of *N225* and *N321* were also investigated to compare with the sintering of NPs which consist of the similar number of atoms.

The HA index, which is characterized according to the atom root pairs and bond types, is divided into four categories, each representing the "fcc" (the bond type of 142), "icosahedral" (the bond type of 155, 154 and 143), "others" (the bond type of 120, 121, 130, 132 and 133) and "bcc" (the bond type of 166 and 144) atoms. Those has been stated in Chapter 2.

The clusters are defined as fcc atoms bonded together within the distance of 3.09 Å, which is the valley distance between the first-nearest neighbor and second-nearest neighbor. At a particular time during the sintering, there may exist several clusters. The cluster size is counted as N_i, which is the number of those atoms involved. Each cluster has a mass center r_i, which is the averaged position for each atom. A parameter of r is obtained as the following, which quantifies the averaged cluster position at that time, $r = \frac{1}{\sum_i N_i} \sum_i \left[N_i \left(r_i - r_{mass} \right) \right]$, where r_{mass} is the center of mass of the entire NP.

4.3 Results and Discussion

4.3.1 Shape Anisotropy for Multiple NPs during the Sintering Process

The relative shape anisotropy k^2 is firstly discussed to provide a quantitative view on how the NPs are sintered. Figure 4.1 shows the shape anisotropy variations for the coalescence of four (*4-N55*), six (*6-N55*) and eight (*8-N55*) single *N55* NPs, respectively, within the first 3 ns. Four different temperatures are considered, which are notified as 900 K, 950 K, 1000 K and 1050 K. The initial configurations as the tetrahedron, octahedron and cube are inserted correspondingly. The shape anisotropy values for the three cases are at the same scale for comparison.

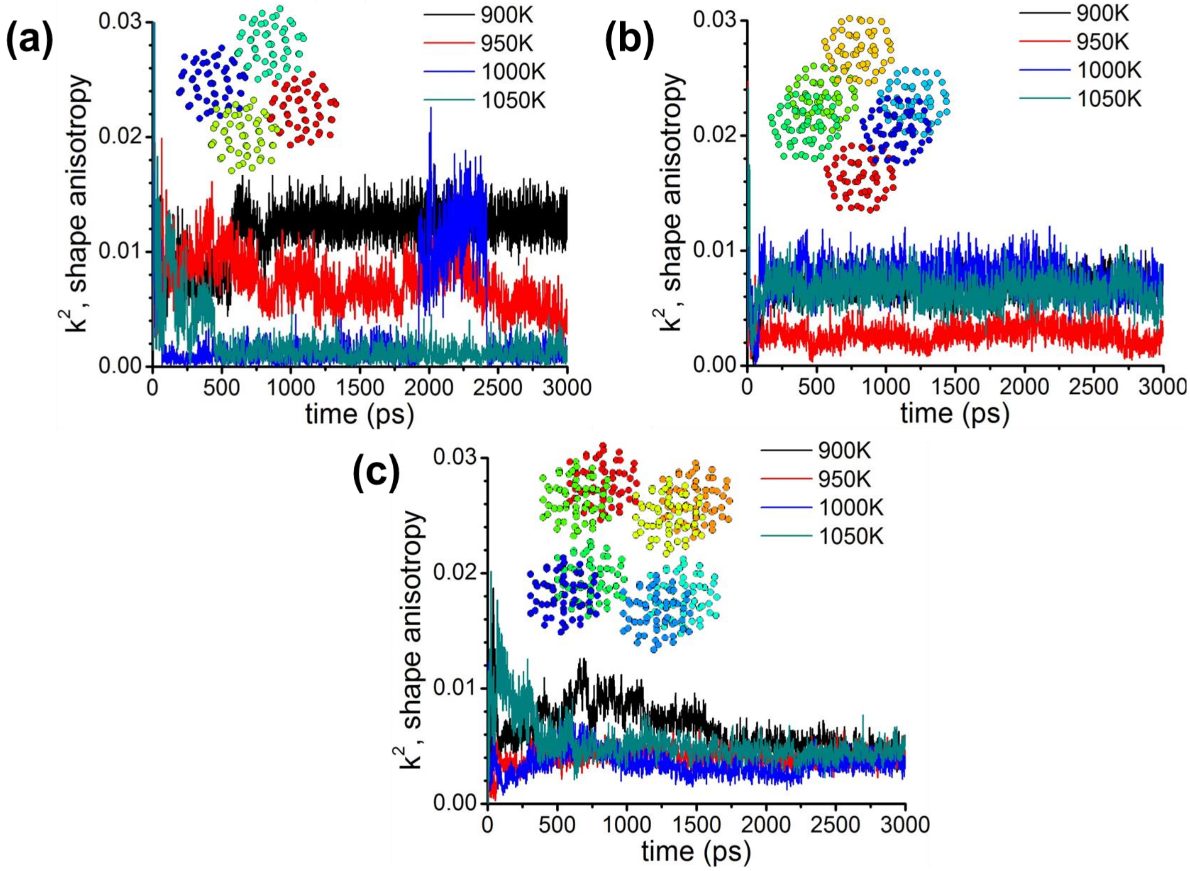

Figure 4.1 Shape anisotropy for (a) 4-*N55,* (b) 6-*N55* and (c) 8-*N55* Ni NPs at different temperatures. The initial configurations as the tetrahedron, octahedron and cube are inserted correspondingly.

The first thing to consider for this sintering model is the coalescence time of the multiple NPs, on the basis of the atomic number ranging from 220 (four *N55* NPs) to 440 (eight *N55* NPs). Generally, for example, the suitable time for the necking investigation of *4-N55* is around 1000 ps.

In Figure 4.1 it also shows that the *4-N55* has the largest initial k^2; however at high temperatures of 1000 K and 1050 K, the shape anisotropy is much smaller indicating the NPs at these temperatures become more spherical than the initial configurations. For the *6-N55* and *8-N55* cases, the shape anisotropy also tends to decrease at high temperatures. This suggests at low temperatures, the cluster does not reach equilibrium so that the merged NP is more likely to facet, while at high temperatures the entire NP becomes more homogenous thus having a low value in terms of the shape anisotropy. Overall, the k^2 value varies only below 0.02 for almost all cases, so different temperatures don't influence the shape change quite much to a large extent. Regardless of the initial shape, the dramatic shape changes take place at the very beginning of the coalescence, lasting for less than 100 ps. Then it takes more than 1 ns for the shape to become stable. After the NPs fully merge together, there are small fluctuations indicating the current NP shape is stable.

4.3.2 HA Index for Multiple NPs at Different Temperatures

The HA index for 4, 6 and 8 NPs are obtained when the coalescence of NPs are stable, i.e., after they are kept for 10 ns. The HA index to characterize the "fcc", "icosahedral", "others" and "bcc" atoms, is shown in Figure 4.2. The single *N225* NP and the *N321* NP are analyzed to compare with *4-N55* (220) and *6-N55* (330), respectively.

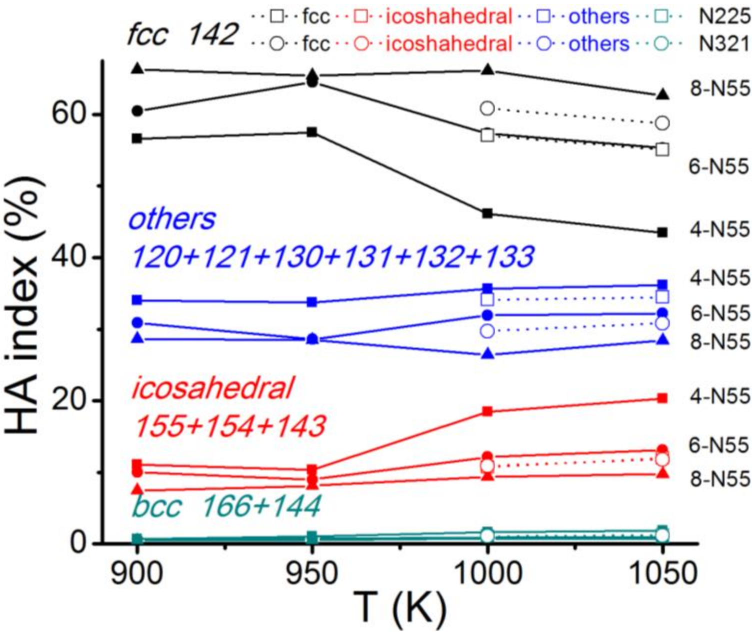

Figure 4.2 HA index ratio for multiple NPs and two NPs with size *N* = 225 and =321 at different temperatures.

The dominant structure for all the four types we investigated in this study is fcc, indicating the crystalline character for NPs when the atom number exceeds 170, as concluded in our previous study[180]. Figure 4.2 also generally suggests that the more total atoms of the NPs before coalescence, the larger percentage of the final fcc atoms and the smaller fraction of the final "others" type, which represent the surface amorphous liquid-like state.

One the one hand, the four structures according to HA index are temperature dependent, for instance, the fraction of fcc differs by over 10% in *4-N55* over the temperature range. However, it seems no significant correlation between the fractions of

HA index in equilibrium and the shape anisotropy variations in Figure 4.1. On the other hand, the structure difference between the coalesced NPs and the single NP with the similar atom number is not large, especially when NP gets larger. For example, the fraction of the fcc structure for the *6-N55* and *N321*, which two are differed by the noticeable disparity of 9 atoms, diverges by 5% at 1000 K and 1050 K. That for the *4-N55* and *N225*, differed by 5 atoms, has the deviation larger than 10%.

4.3.3 Comparison between Shape Anisotropy k^2 and HA Index

Based on the similar patterns for the shape anisotropy and HA index variations concerning the initial tetrahedral, octahedral and cubic shape, *4-N55* is taken as an example to represent the sintering for the multiple ultra-small NPs for the rest part in our discussions.

The temperature of 900K and 950K are taken to investigate the HA index as a function of the sintering time, that is the isothermal HA index variations. Figure 4.3a and 4.3c shows that in the two cases, both have sharp jumps within the first 50 ps. At the beginning, the “others” type of atoms for the four separated *N55* NP has the largest fraction, which is because of the nature for the high ratio of surface atoms of each single *N55* NP. And then after 50 ps the fcc structure gradually dominates.

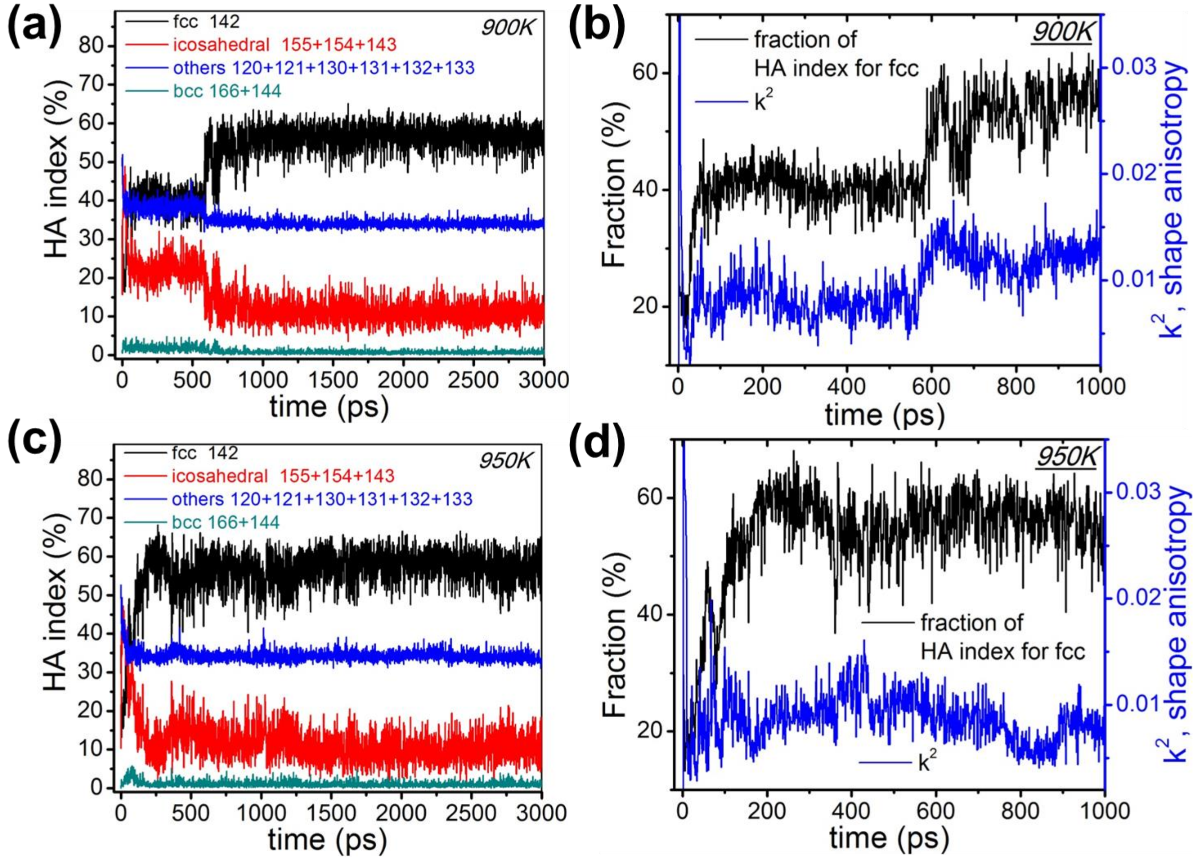

Figure 4.3 HA index ratio for the isothermal sintering processes of *4-N55* and the related shape anisotropy.

The shape anisotropy change is correlated with the HA index change, shown in Figure 4.3b and 4.3d, respectively, which are compared to Figure 4.3a and 4.3c in a magnified range at the right hand side of each figures. It takes about 700 ps for the merged NPs gets stable at 900K, while about 200 ps at 950K. So for example, at 900K in Figure 4.3b, for the beginning 10 ps, the shape anisotropy is relatively large and the fcc fraction is lower than 30%. Both the fcc fraction and the k^2 value has a sharp jump and then form a flat curve before 600 ps and finally jump up again. So that the visualized shape change for NP coalescence process, which is characterized by the shape anisotropy, is well related with the local atomic structures, e.g., the fcc fraction.

4.3.4 Atom Movement in the Central Region

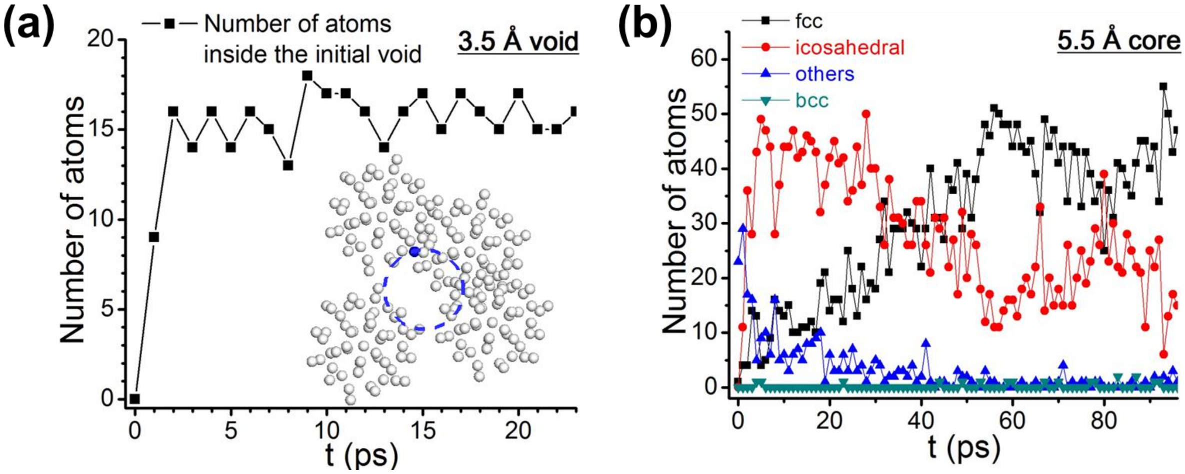

Figure 4.4 (a) Number of atoms inside the initial void for *4-N55* at 950 K. The inset is the initial configuration, where the blue dashed line circle out the void with a radius of 3.5 Å. (b) Number of different types of atoms inside the 5.5 Å core.

Since we initially place the NPs at the corners of tetrahedron, there exists a void with the radius of 3.5 Å in the sintering of 4 NPs, which is shown in the inset of Figure 4.4a as the initial configuration. Figure 4.4a shows the number of atoms entering into the 3.5 Å void is counted as a function of time. At time zero, there is no atom inside the void; at 1 ps, there are 9 atoms moving in. After 2 ps, the number of atoms keeps stable around

15, meaning the initial void has been occupied by atoms. This suggests all the structure changes and the atomic dynamics after 2 ps will be the localized atomic rearrangement.

To investigate the types of atoms in the central region, a larger core with the radius of 5.5 Å is considered. The number of atoms inside this core and their local atom type is shown in the Figure 4.4b. At time zero, there are 1 fcc, 0 icosahedral, 23 “others” type atoms counted inside. And then the icosahedral atoms will firstly increase to about 50 and then decrease. The surface atoms will have a slight increase and then decrease to totally 0. The fcc atoms will gradually increase and finally dominate this central region. The stable number for atom occupying this 5.5 Å core is around 60. This suggests in the core area exists dynamic exchanges in terms of the atomic types, no matter from “other” atoms to the fcc structure, or between the fcc structure and the icosahedral structure.

4.3.5 Spatial Distributions of the FCC Clusters

In order to have a global view at how the atoms are rearranged especially for the change of the fcc structure, the atom type at a specific moment is compared with its initial type in Figure 4.5. The type transitions related with fcc type are shown in the figure.

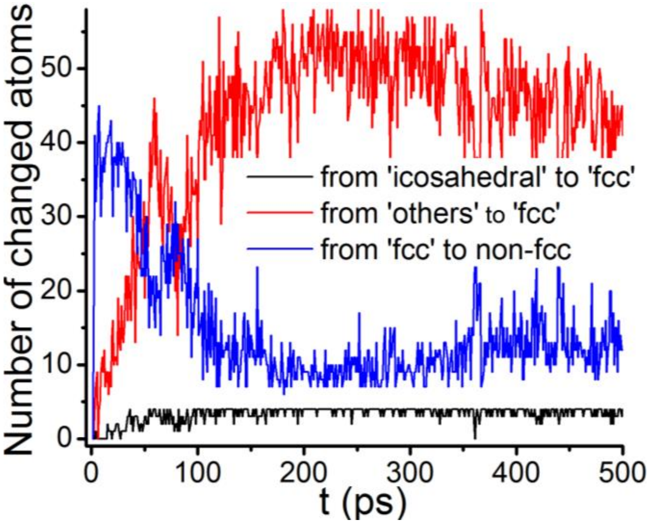

Figure 4.5 Number of atoms changed between different types regarding the fcc type for the entire *4-N55* NPs case.

First and foremost, from fcc to non-fcc type, the number firstly increase to its peak of 45, and then gradually decrease, resulting in the change back of fcc atoms. Since the number of the fcc atoms for the initial configuration is 48, which distributes as four separated 12 fcc cluster for *4-N55* NPs, it suggests that the initial fcc cluster for each single *N55* NP will break down upon coalescence at the beginning. Secondly, from others to fcc type, it grow steadily, which means the initial "other" atoms (those mostly on the initial surface) count the most for the transferred fcc atoms. Last but not least, from icosahedral to fcc type, the initial four icosahedral atoms, which occupy each center of the single *N55* NP, totally changed to fcc.

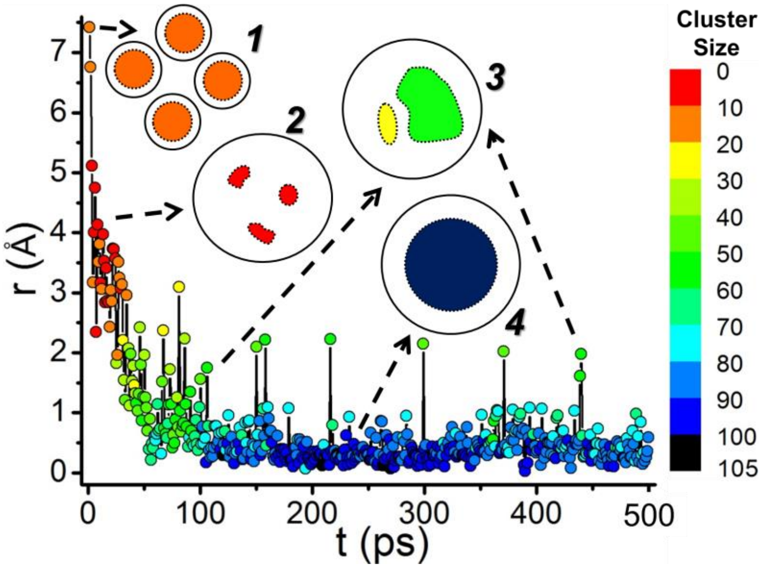

Figure 4.6 Cluster size and spatial distributions for 4-*N55* sintering process and sketch map of the fcc cluster formation and growth process.

Figure 4.6 shows the averaged r for those individual clusters, where r_i measures the distance between one's own mass center and the mass center for the total 220 atoms, as well as the averaged cluster size N. Firstly as the time increasing, the cluster becomes larger indicated by the representing color changing from red to blue and black. Meanwhile, the value of the r decreases from 7 to almost 0, indicating the spatial distribution of the fcc clusters. The averaged fcc mass center moves from the outer shell (which is counted as 7) to the NP core (which is counted as 0).

It would be better for us to imagine the initial configuration being each cluster with atom number of 12 for each single *N55* NP, which is illustrated as the inserted picture (1). And then, as mentioned above, the large fcc clusters break down, while some smaller separated clusters originate at a distance of 3 ~ 5 Å from the entire center, shown as the inserted picture (2). The distance gradually decreases with the increase of the cluster size, meaning more and more fcc atoms form cluster near the central position, which is illustrated as picture (3). Finally, picture (4) shows the fcc atoms tend to form one entire cluster locating right in the center. The sketch map from (1) to (4) inserted in Figure 4.6 roughly demonstrates the fcc cluster growing process. In addition, the intermediate entire fcc cluster doesn't guarantee there won't be any fluctuations later on – the cluster size can become a little smaller and the clusters can deviate from the center, which is evidenced by the spikes on the curve in Figure 4.6.

4.3.6 String-like Collective Motions for the Sintering Process

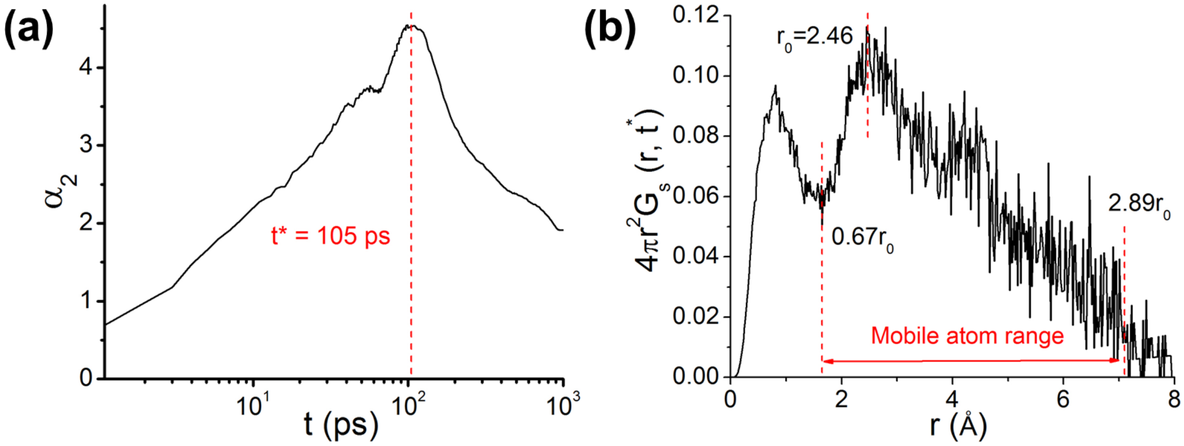

Figure 4.7 (a) Non-Gassian parameter and (b) Van Hove function for *4-N55* case.

The examination of the string-like atomic movement is carried out to check if this type of motion exists in the sintering process. Two essential parameters are investigated before-hand, α_2 and $G_s(r, t)$ which has been explained in the Chapter 2.

In Figure 4.7a, the value for t^* obtained from the peak of the non-Gaussian parameter is 105 ps. By substituting t^* into van Hove function, the mobile atoms range is defined from the lowest between the first peak and the second peak, to the downward tail, as seen in Figure 4.7b.

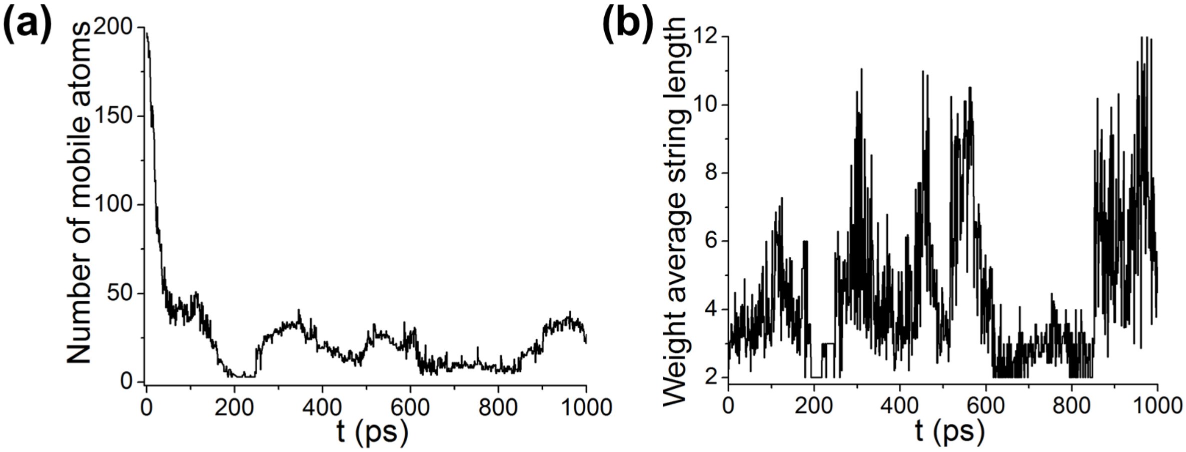

Figure 4.8 (a) Number of mobile atoms and (b) string length for the sintering process for *4-N55* at 950 K.

Figure 4.8a shows the calculation results for the number of mobile atoms and the weight averaged string length. At the beginning, nearly 200 out of the total 220 atoms are found as the mobile atoms. It manifests that at the beginning of the coalescence, almost all the atoms are considered as mobile, indicating a strong dynamics for the entire system.

The number of mobile atoms sharply decreases upon coalescence. After about 250 ps, it begins to rise and fluctuate around less than 30. Accordingly, the weight averaged string length before 250 ps is relatively small, while it becomes as large as 10 afterward, as shown in Figure 4.8b, suggesting an equilibrium melting and freezing processes[170] where long strings only appear on the surface of the entire NP.

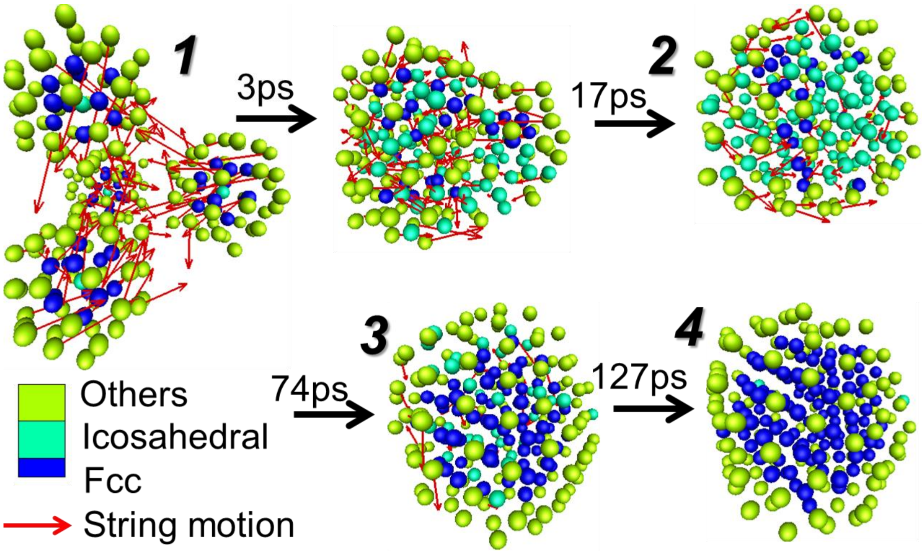

Figure 4.9 String configurations for the sintering process for *4-N55* at 950 K.

Figure 4.9 demonstrates some snapshots for the sintering process highlighted with different local structures and the string-like motion colored in red arrows. It shows that at the beginning of the coalescence, the number of atoms participating in the string motion is large and all the string-like motions tend to point to the 'void' between the single NPs. it means that there is the inward rotation movement for each single *N55* NP. After 3 ps of the occupation for the central void, the atomic strings are still crowded a lot and there are plenty of atoms in the inner core engaged in the strings. As time goes on, this phenomenon for the inner core atom engaged string motion gradually eliminates and most strings only appear at the surface and interfacial region of this merged NP. The string length at this time is still small. At the later stable stage, the strings are only also found at the surface of the large NP, whose length is long, compared with those previous snapshots. The labelled configurations from (1) to (4), where the blue atoms represent the fcc atoms, also correspond to the sketch map of the fcc clusters in Figure 4.6.

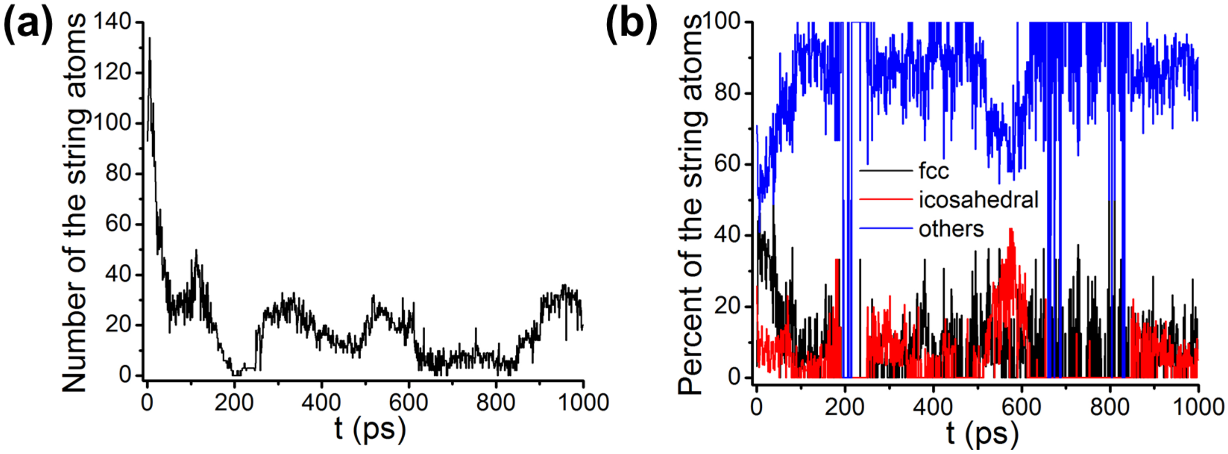

Figure 4.10 (a) number of string atoms on dependence of time. (b) variations of different types of string atom on dependence of time.

To further investigate the string motion in relation to the local structure change for the coalescence of the ultra-small NPs, the string atoms are also divided into three categories, fcc, icosahedral and others, based on the HA index analyses. Each part is rescaled by the total number of string atoms, so the information of the relative ratios is provided, as shown in Figure 4.10b. It can be noticed that, the surface atoms, which refer to the “others” type, are always more than half of the string atoms. In the beginning of approximately 200 ps, treated as the border to form a completely entire NP, the phenomenon of the increase of “others” atom ratio and the decease of icosahedral atom ratio is obvious, indicating the gradual sintering process. And then after 200 ps, despite of some fluctuations, almost all string atoms are the “others” atom type although the total number is less than 30 seen from Figure 4.10a. It means the string motion facilitates the process for the previous surface atom to transfer into the icosahedral or fcc atom type, which helps the crystallization of the ultra-small NPs after coalescence.

4.4 Conclusions

Instead of studying the sintering mechanics dominating different sintering periods, we examined the coalescence of multiple ultra-small *N55* NPs with the focus of the local structure rearrangement and crystallization of the fcc structures. The results of the relative shape anisotropy k^2 and the Honeycutt-Andersen (HA) index provide us with the evidences that the two factors are strongly correlated. The evolvements of the local fcc structure, the local icosahedral structure and the liquid-like structure is a dynamic transferrable process, where the initial fcc cluster for each single *N55* NP breaks down upon coalescence, and the initial liquid-like surface atoms contribute the most for the final pure fcc structure. The reduced inherent fluctuation for the sintering process is facilitated by the growing of the fcc clusters, accompanied with the string-like atomic motions.

5 Single Small Nanoparticle on the Freestanding Graphene Sheet

5.1 Introduction

The catalytic nature of the nanoparticles is well established. Concerning the applications for the NPs in the real world, where they no longer stand solely in the vacuum, it's vital to control the NPs in the real experimental conditions for the interactions with the supporting materials. Therefore, the single-atom-thick graphene is considered as an ideal substrate[181, 182]. The graphene is not only a promising but an effective substrate materials to support the NP for use as a catalyst. Many earlier studies have reported the enhaced mechanical poperties[183] and electrolyte properties[83, 84, 184] for the NP-graphene composite materials. However, the interfacial atomic motions for the NP above the graphene substrate has not been examined. Based on our previous studies of the interfacial dynamics for the single NP, our focus is to try to find out what the changes take place by the introduction of the graphene to the Ni NP. In this chapter, we utilized the Reaxff potential for the single Ni NP with the graphene substrate and investigate the simulation results for the interfacial dynamics of the NP, compared with the single NP without the substarte as a external constraint.

5.2 Simulation Methodology

In order to study the interaction between the Ni NP and the graphene substrate, the NP with the atomic number of 369 is initiated, which is marked as *N369*. The initiation process is the same as in the previous two chapters.

Two types of the potential energy, both the Voter-Chen EAM and the Reaxff force field methods, are selected for the NP. The NP is first relaxed at room temperature for 1 ns with zero angular and linear momentum. Next, the NP is heated up at a rate of 500 K/ns from the room temperature (T = 300 K) until the NP melts (around 1250 K). Experimentally, the nanoscale Ni element and the graphene system can undergo as high as 1000°C with the protection of the reductive gas[81, 82](H_2, Ar and/or CH_4). In order to probe the kinetic processes that cannot be observed while heating at a continuous and high rate, the isothermal heating at temperatures of 1000 K, 1100 K and 1200 K. At each temperature the NP is kept for 3 ns.

On the other hand, the simulation for the bare graphene substrate is based on the Reaxff potential only. Basically the graphene sheet with a roughly square shape is selected. In order to be compatible with the *N369* NP with diameter d = 2.03 nm, the graphene sheet can't be too small, e.g. with the edge length l less than 3 nm. Also considering that computation resources taken by the whole system, the graphene sheet doesn't necessarily to be too large, e.g. with the atom number of more than 1200. Therefore, the graphene substrate is selected with the edge length l = 5 nm, and the atom number of 960. It is generated using the software 'Nanotube Modeler'[185].

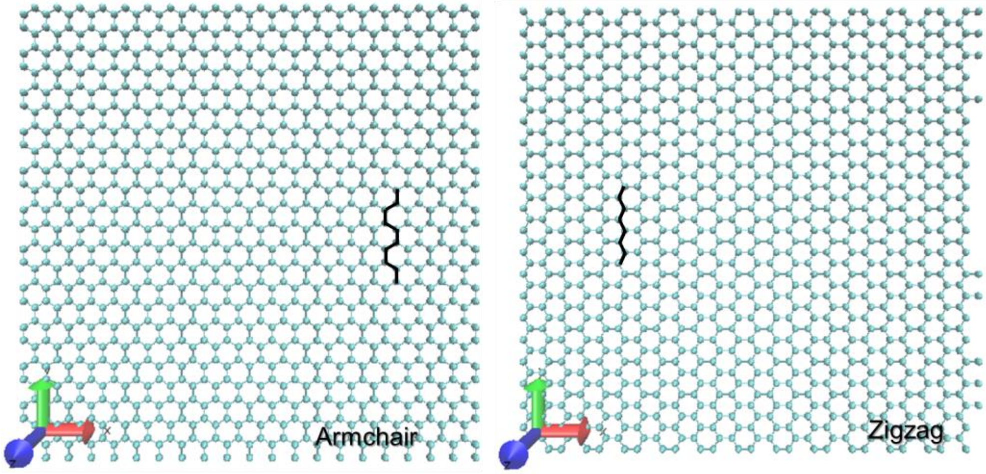

Figure 5.1 Armchair and zigzag type of the graphene sheet and their atomic bonds along the folding *y* direction

Based on the chirality indices (*n*, *m*), which define the rolling-up direction for the graphene sheet, different sheets all with the atom number of 960 can be generated according to the different (*n*, *m*) values. Those sheets are included two extreme type, the armchair (where $n = m$) and the zigzag (where $m = 0$), and the normal chiral type (where *n* and *m* have different non-zero values). Figure 5.1 shows the armchair ($n = 12$, $m = 12$) and the zigzag ($n = 20$, $m = 0$) graphene sheet both with the edge length $l = 5$ nm, and the atom number of 960. For the properties of the carbon nanotube folded up by different types of graphene sheet, which is also known as chirality, the armchair type tends to be more metallic and the zigzag type tends to be more semiconducting. Nevertheless, in this thesis we only use the flat graphene sheet. The difference between the armchair and the zigzag type is only a matter of directions, which can be seen in Figure 5.1. Because the NP is three-dimensional symmetric, both these two type will not have much differences with the interactions with the NP based on the chirality. Thus, the armchair (n = 12, m = 12) type, which is more square rather than rectangle, is selected finally.

The default length of the C-C bond in the software is 1.41 Å. If the graphene with this bond length is directly used at high temperature, e.g. above 1000 K, large ripples arise because the thermal expansion of the C-C bond is restricted in the limited simulation box concerning using the periodic boundary conditions. In order to get the relatively flat graphene sheet as the supporting substrate for the Ni NP, the graphene sheet generated with different C-C bond length, from 1.42 Å to 1.45 Å, is first relaxed at different temperatures, from 800 K to 1200 K with the increase of every 100 K, to see the pressure P fluctuations. The pressure of the system can represent the relative forces that the sheet undergoes, therefore it's used to determine whether the sheet is stretched ($P > 0$) or the sheet is compressed ($P < 0$). And then the proper C-C bond length for the graphene sheet at a particular temperature is determined if the simulation shows the averaged pressure P over time is near zero. For example, at 1200 K, the suitable C-C bond length is 1.4446 Å to make sure the sheet undergoes no external forces. Once the bond length for each temperature is determined, the isothermal-isobaric (*NPT*) ensemble (see the details in chapter 2) is used to fully relax the sheet and get a final box size, which is at last used as the constant volume for the initiation box in the simulation, referring to either the microcanonical (*NVE*) ensemble or canonical (*NVT*) ensemble.

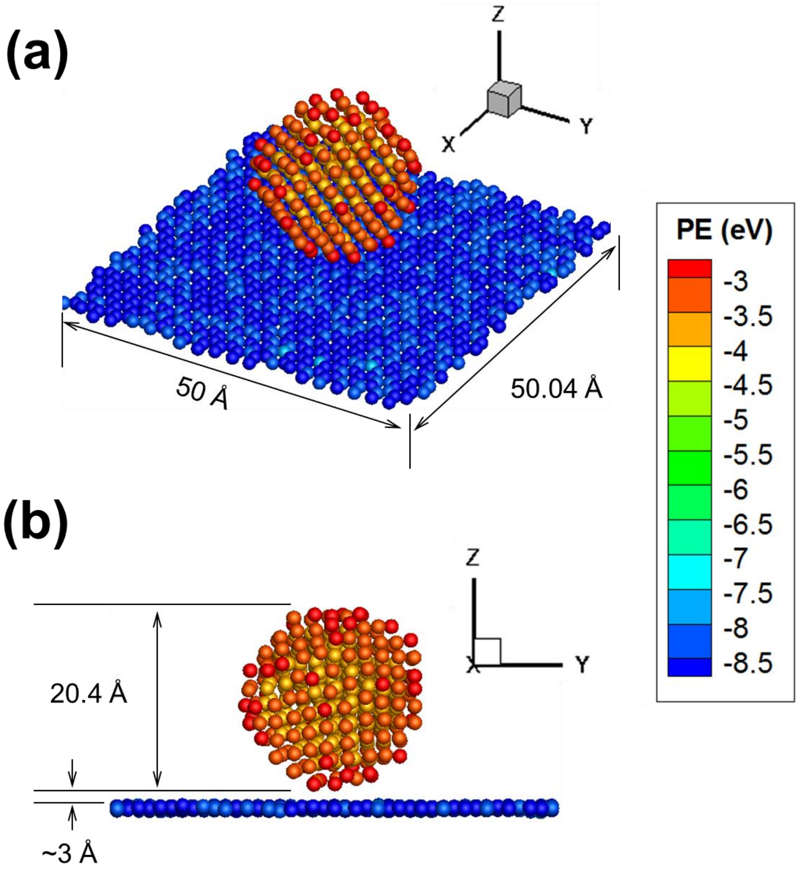

Figure 5.2 Schematic maps from (a) a normal view and (b) <*yz*> plane view for the initial configuration of *N369* NP and the graphene substrate at 1000 K

The NP and the graphene sheet at the same absolute temperature are selected together to create the initial configuration for the simulations, which is shown in Figure 5.2. The NP is then put at the center of the graphene sheet both along the x and y direction, and for the nearest distance for the atoms along the z direction above the substrate being 3 Å, as indicated in Figure 5.2b. This distance is selected to be less than the cutoff distance for C and Ni in the potential file and not too close to cause expulsion for the Ni atoms and C atoms.

In order to compare the influences of the substrate on the NP, three sets of simulations are carried out. They are the single free *N369* NP, the *N369* NP with the center fixed and the *N369* NP (center fixed) with the substrate. The berendsen heat bath is used together with the microcanonical (*NVE*) ensemble in order to maintain the total energy of the whole system for the NP and the substrate. All the sets then undergoes isothermal heat treatment at 1000 K, 1100 K and 1200 K, each for a 3 ns relaxation process.

5.3 Results and Discussion

5.3.1 Dynamic Differences for Ni NP between the Use of the Reaxff and the Voter-Chen EAM Methods

The NP shape fluctuations are firstly investigated for the single Ni NP having a radius of about 2 nm using both the Reaxff force field and the Voter-Chen EAM method, as shown in Figure 5.3. The reduced temperatures are used here for comparison. For the NP using Reaxff the reduced temperature is at 0.8 T_m and for the NP using Voter-Chen EAM method is at 0.78 T_m. It shows that the NP using the Reaxff has larger fluctuations in the shape anisotropy than the NP using the EAM method. However, that the average values for both the Reaxff and the EAM methods are around 0.005, which indicates the surface and interfacial dynamics for the Reaxff is generally at the same level with the previous Voter-Chen EAM simulation work.

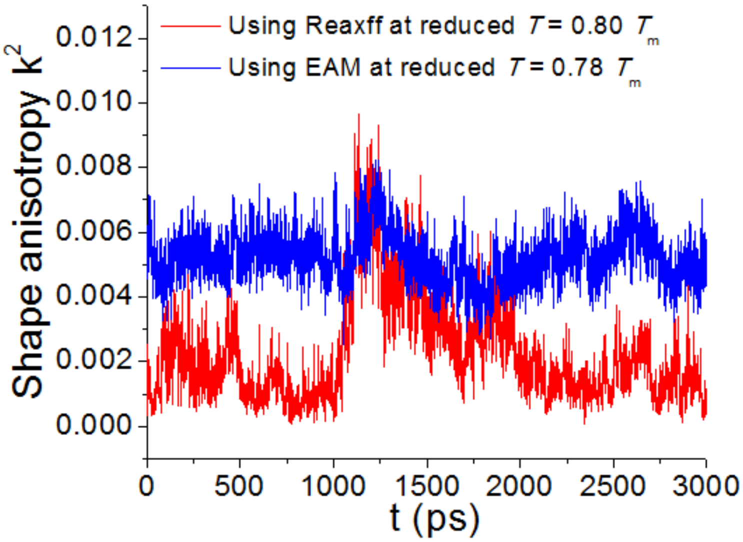

Figure 5.3 The shape anisotropy for *N369* with the Reaxff force field and with the Voter-Chen EAM method at approximately equal reduced temperature

Compared with the peak shape anisotropy value $k^2 = 0.1$ for *N55* in Chapter 3, the shape anisotropy for the NP of *N369* there is significantly small, $k^2 = 0.005$. It shows the shape variation is only 5% of the NP of *N55* having a diameter of 0.8 nm. There is no need to consider the atomic dynamics affecting the shape anisotropy for the *N369* NP, even applied with different force fields. Thus, for the rest of this chapter, the experiments are all using Reaxff.

5.3.2 Local Geometry of the *N369* NP with the Substrate

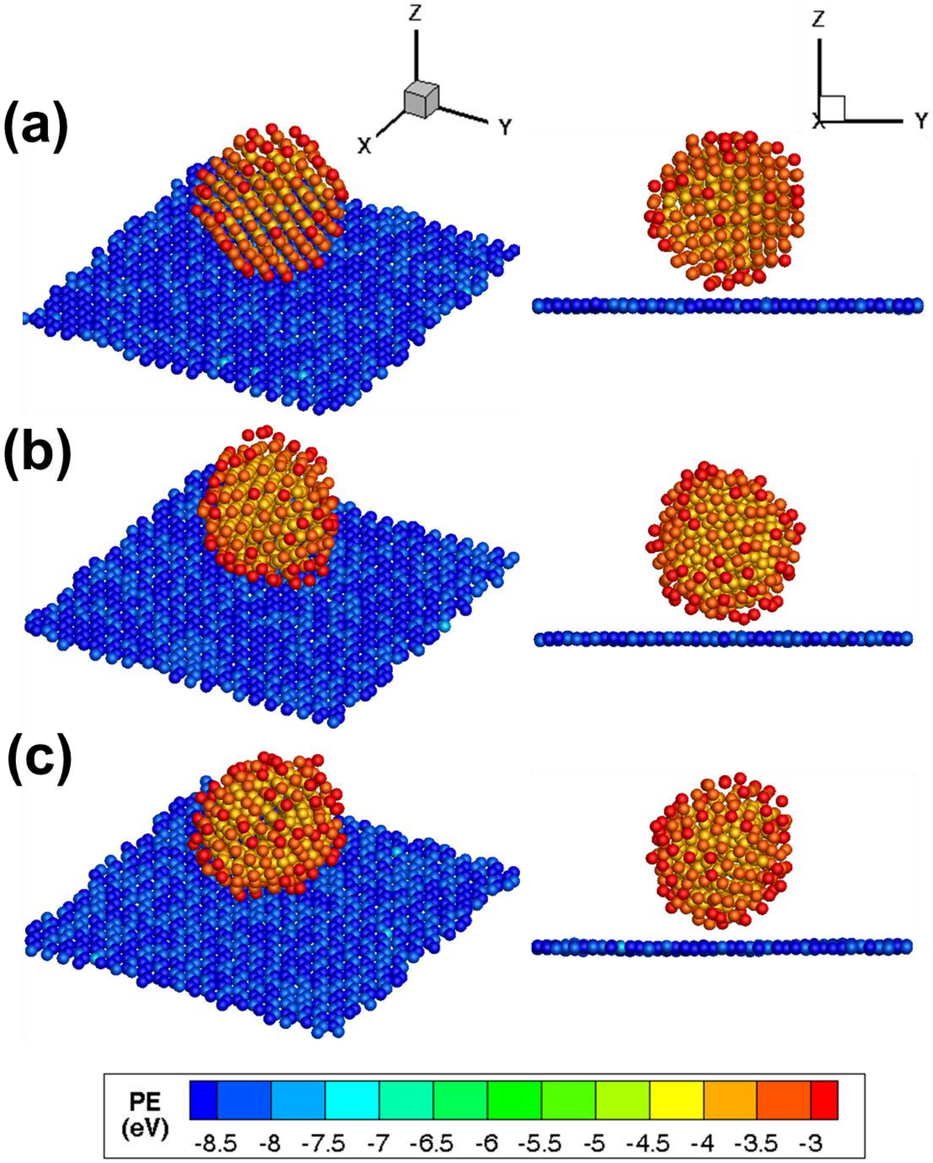

Figure 5.4 The initial configurations of *N369* NP with center fixed standing on the graphene substrate at different temperatures of (a) 1000 K, (b) 1100 K and (c) 1200 K

A quick look is provided for the initial configurations *N369* NP with center fixed standing on the graphene substrate at different temperatures in Figure 5.4. It is obvious that the graphene sheet has little temperature dependence regarding the configurations; the noticeable difference on temperature dependence is the distribution for its potential energy *PE*. With the increase of the temperature, the color scales for the graphene sheet change from dark blue to light blue indicating the increase of the total potential energy.

In terms of the Ni NP, the temperature dependence of the configuration is relatively more obvious. At low temperature, both the surface and the inner core of the NP are with ordered lattice. The faceting is also observed. With the increase of the temperature, the surface of the NP becomes more disordered with high *PE* value. However, the inner core of the NP remains the organized arrangement with low *PE* value.

To take a qualitatively look at how the local structure for the NP are revolved when it is placed above the graphene sheet, the HA index analysis is carried out for the (I) single free *N369* NP, (II) the *N369* NP with the center fixed and (III) the *N369* NP (center fixed) with the substrate. The results are shown in Figure 5.5.

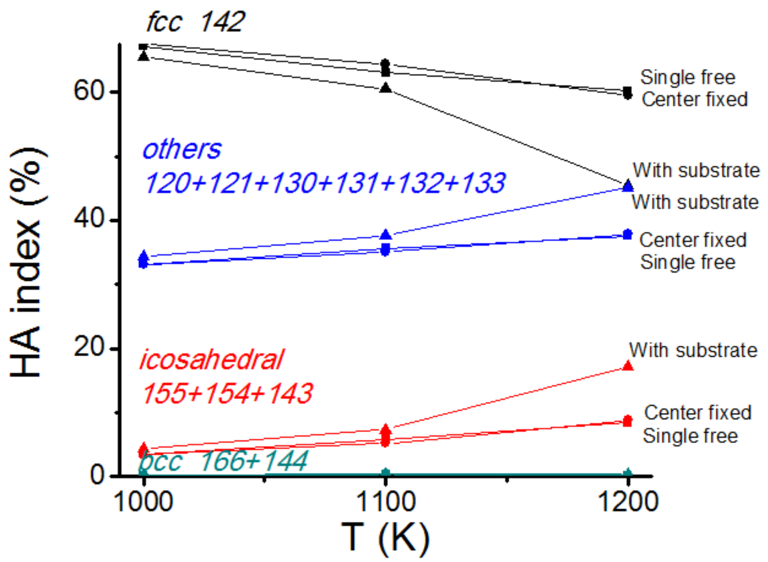

Figure 5.5 HA index ratio for the single free *N369* NP, the *N369* NP with the center fixed and the *N369* NP (center fixed) with the substrate on dependence of temperature

The detailed description for the categories of the HA index is included in Chapter 2, “2.6.1 Quantitative Analysis of the Local Geometry”. The dominant structure for the NP is still fcc, no matter in which situation the NP is initiated for the above three cases. Generally, the ratio of the fcc structure decreases when the temperature goes higher. It indicates the larger heat provides more energy for the NP to become disordered, which confirms the configurations in Figure 5.4 and is consistent with the study of NP melting in the previous chapters of this thesis.

What’s more, for the single free NP and the single NP with center fixed cases, the HA ratios is almost the same for all three temperatures. It means that the fixation of the center atoms doesn’t affect the local structures of the NP since the inner core itself basically stays the same ordered structure. It makes no difference whether or not fix the center of the NP. Thus we treat the analysis is the same for the free NP and the center fixed NP. Take the center fixed NP as an example, Figure 5.6 provides its HA index ratios on dependence of time at different temperatures.

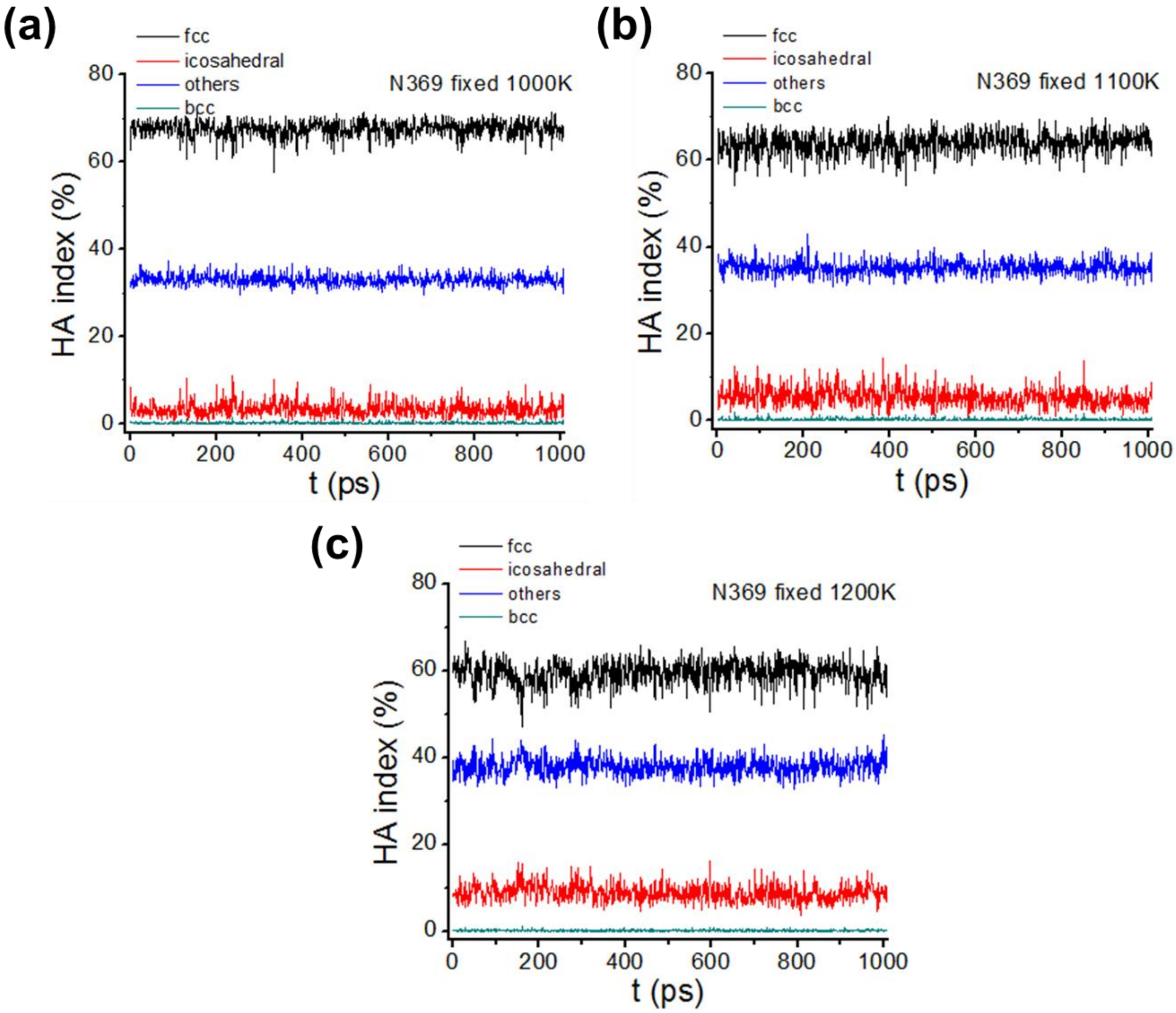

Figure 5.6 The detailed HA index ration for the isothermal study of *N369* NP with the fixed center at (a) 1000 K, (b) 1100 K and (c) 1200 K

Meanwhile, upon placing the NP above the substrate, it does matter whether the NP is totally free or with the center fixed. Here, the discussion of the substrate effect is only focused on the *N369* NP with its center fixed. Back to Figure 5.5 for the "with substrate" case, the variation for the local structure is much more temperature dependent; for example, the fcc ratio declines to a larger degree compared with the single NP. Last but not the least, the level crystallization of the NP affected by the substrate is always lower than the single NP according to the smaller fcc ratios at all temperatures. It means the substrate makes the NP more disordered and more active.

Further, for the NP with the influence of the substrate, Figure 5.7 provides the detail HA index ratios on dependence of time at different temperatures. By comparison with Figure 5.6 for the single NP, several differences can be found out. Firstly, the amount of fcc is less than the free NP. Secondly, with the increase of the temperature, the curves become more fluctuate, that is more 'noisy' than at the lower temperature for itself as well as the free NP in Figure 5.6. And finally, at 1200 K, at the beginning 1.2 ns, the NP seems 'melting' because the ratio of the fcc and the icosahedral structure alternatively go up and down, while the "others" type meaning the amorphous structure counts the most of the local structure. However, after this time region, the fcc structure becomes the largest part, indicating the NP returns the crystal structure. These phenomenons only occur because of the introduction of the underneath graphene sheet.

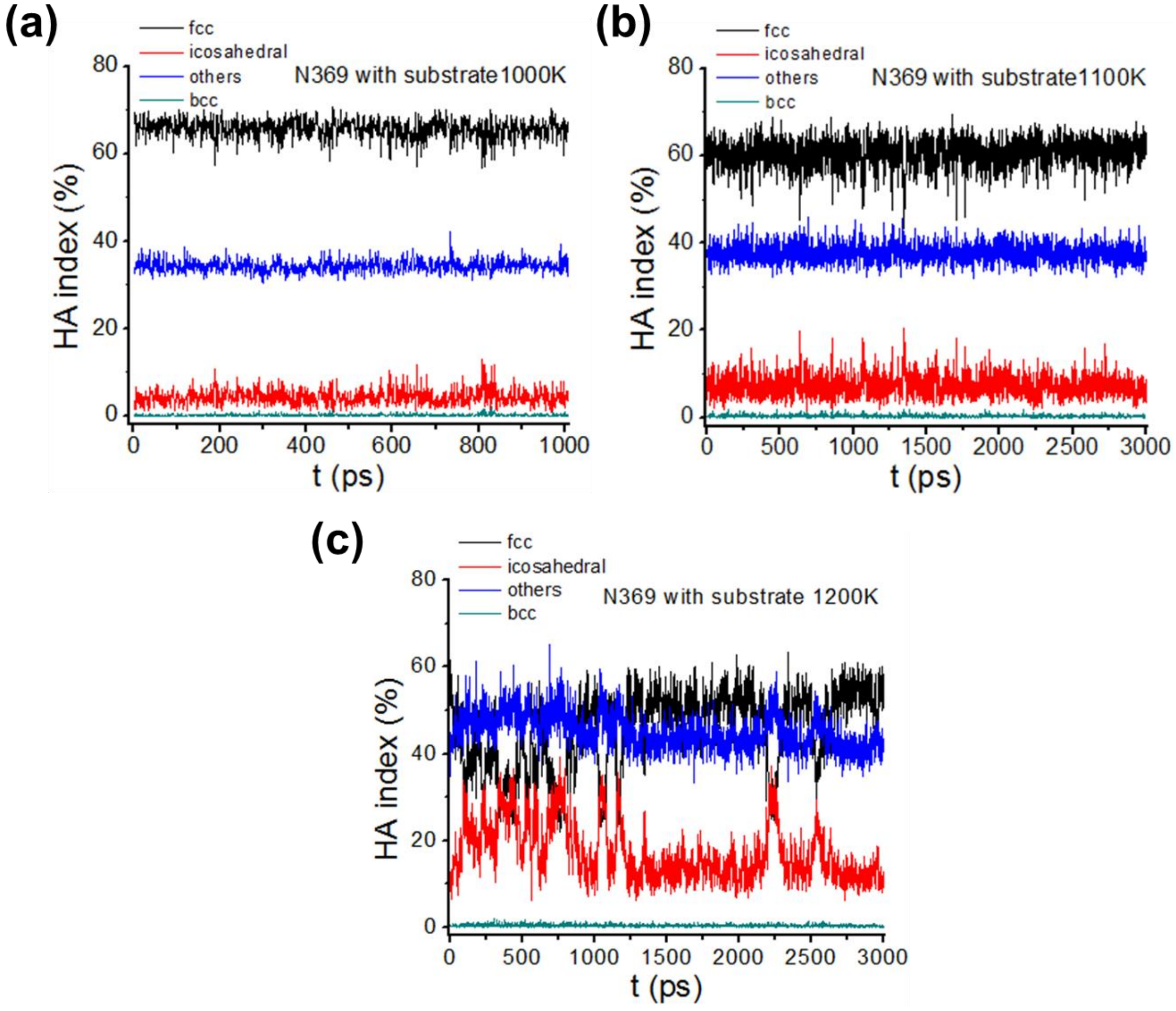

Figure 5.7 The detailed HA index ration for the isothermal study of *N369* NP (center fixed) with the substrate at (a) 1000 K, (b) 1100 K and (c) 1200 K

5.3.3 Dynamics for *N369* NP with the Substrate

In order to understand what's the dynamic process that the NP is involved with the influence of the substrate, the non-Gaussian parameter and the van Hove function are considered to determine the dynamics of the NP. The details for these two parameters are fully included in Chapter 2.

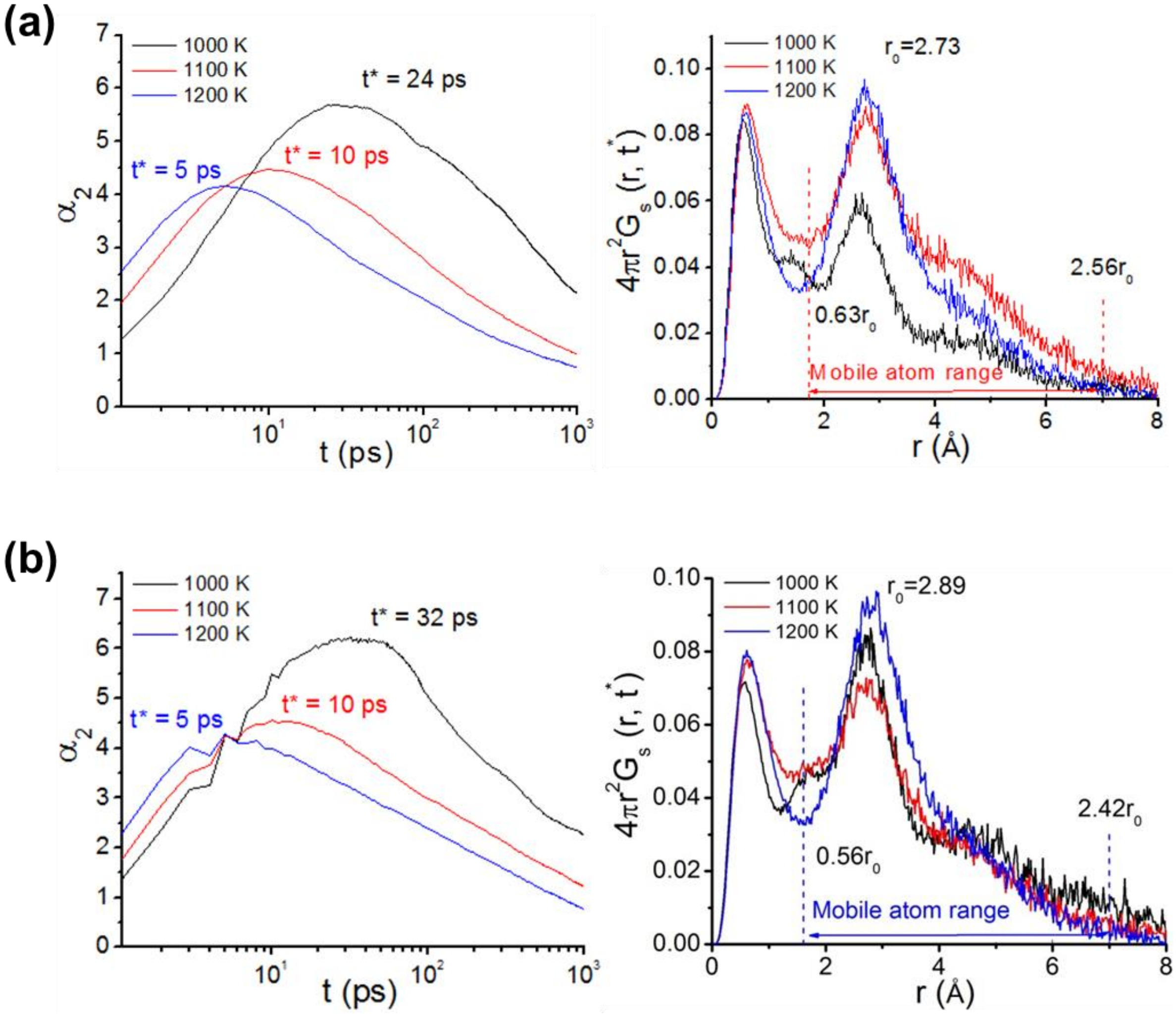

Figure 5.8 The non-Gaussian parameter and the van Hove function for (a) free *N369* and (b) *N369* NP with center fixed at different temperatures

The free *N369* NP and that with the center fixed are investigated at the beginning as the basis to analyze more complex NP with substrate case. As shown in Figure 5.8, the t^* for the single free *N369* is 24 ps at 1000 K, 10 ps at 1100 K and 5 ps at 1200 K. Accordingly, that for the NP with the center fixed is 32 ps at 1000 K, 10 ps at 1100 K and 5 ps at 1200 K. By substituting each t^* into the van Hove function, the mobile atom range are determined for different temperatures. Again, it's clear that the results for the NP with or without center fixed type are almost the same at all three temperatures.

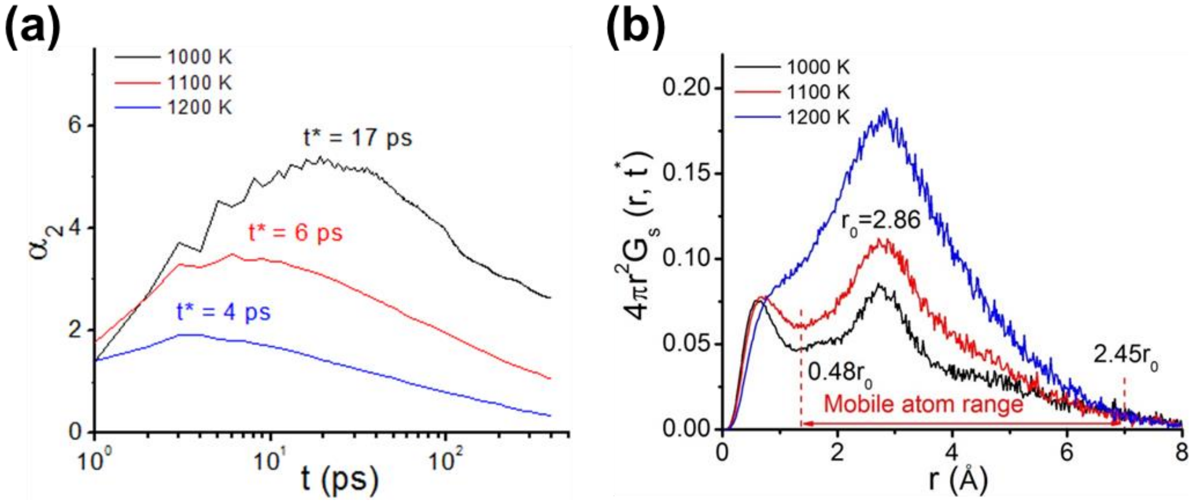

Figure 5.9 The non-Gaussian parameter and the van Hove function for the fixed *N369* with the substrate at different temperatures

In terms of the fixed *N369* with the substrate case, the related results are shown in Figure 5.9, where the t^* significantly decreases. And what's needed to point out is, the van Hove function for the temperature of 1200 K has superimposed peaks, which, according to

Figure 5.7c, would result from the average of the different starting and the latter regions for the HA curve at 1200 K.

5.3.4 String-like Collective Motion for the NP on the Substrate

The identification of correlated atom motion requires a consideration of the relative displacement of particles. Atomistic simulations of glass-forming liquids indicate that the distribution of string lengths $P(n)$ is an approximately exponential function of n. The detail of this analysis is included in Chapter 2. Figure 5.10 shows the distribution of string lengths at $\Delta t = t^*$, where the non-Gaussian parameter exhibits a maximum, at different temperatures for *N369* NP with the substrate as well as the center-fixed *N369* NP as the reference. The average string length $<n>$ is simply determined from the slopes of the curves by $\exp(-n/<n>) \sim P(n)$.

The curves don't show obvious temperature dependence for the string distribution. However, there is a general trend for the average string length to grow upon cooling. And compared with the NP without the chemical environment of the graphene sheet, the averaged string length gets shorter, which can be confirmed from the previous non-Gaussian parameter and the van Hove function that the NP with substrate is more mobile, therefore, should show shorter string length. It indicates that the NP is activated by the interaction of its underneath graphene substrate, even with its center being fixed.

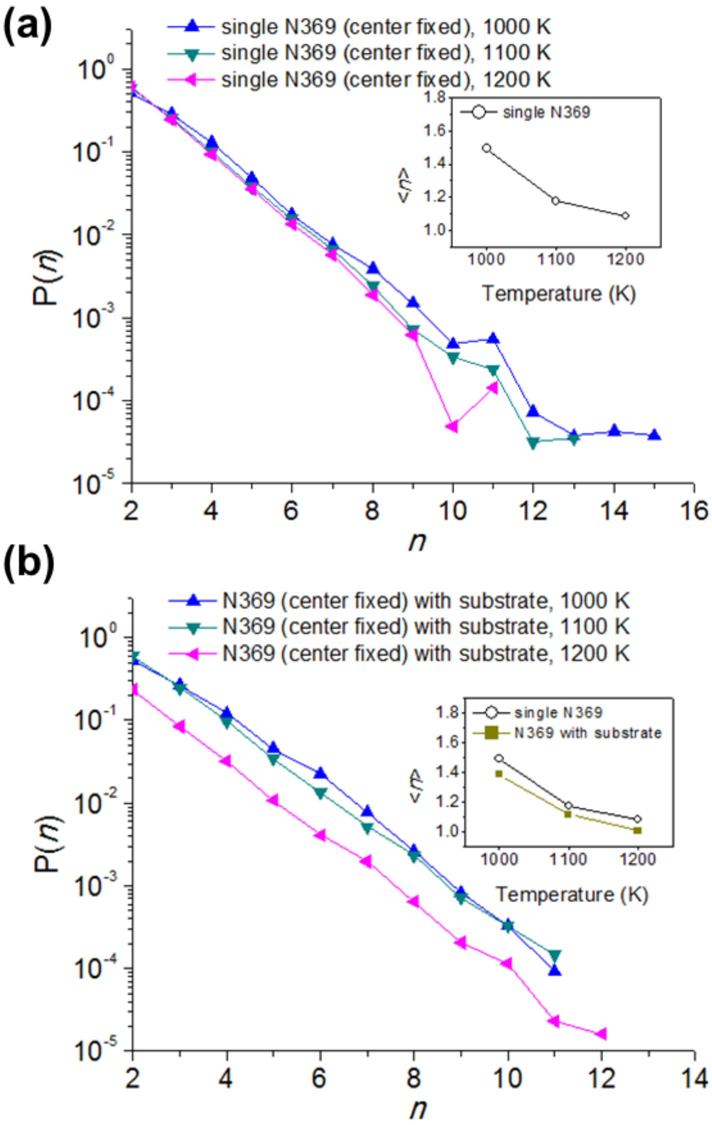

Figure 5.10 The size distribution and mean string length of the collective motion as a function of the temperature for (a) the single *N369* NP with the center fixed and (b) the NP with the substrate. Each inset shows the *T* dependence of the average string length <*n*>.

5.4 Conclusions

It is the first time that we try to investigate the dynamics of the Ni material with the constraint of the inorganic graphene material. We utilize the Reaxff force field potential however the factor affecting the atomic dynamics in terms of the NP shape anisotropy is negligible. The NP with the center fixed shows almost no difference compared to the real free NP.

While placing this center-fixed NP above the graphene sheet, the amount of fcc is less than the free NP. And the averaged string length is smaller which indicates the NP is more mobile on the graphene substrate. Meanwhile, there is not obvious temperature dependence for the string distribution however the average string length increases upon cooling, which is consistent with the study of NP melting and freezing of our previous work[170].

6 Conclusions and Suggestions for the Future Work

6.1 Summary of Main Conclusions

Our major work in the thesis is summarized in Figure 6.1 as shown below. The sphere represents the NP, which can vary with sizes and rotations as illustrated in the figure. The smallest one represents *N55* NP and the one on the substrate is that for the *N369* NP.

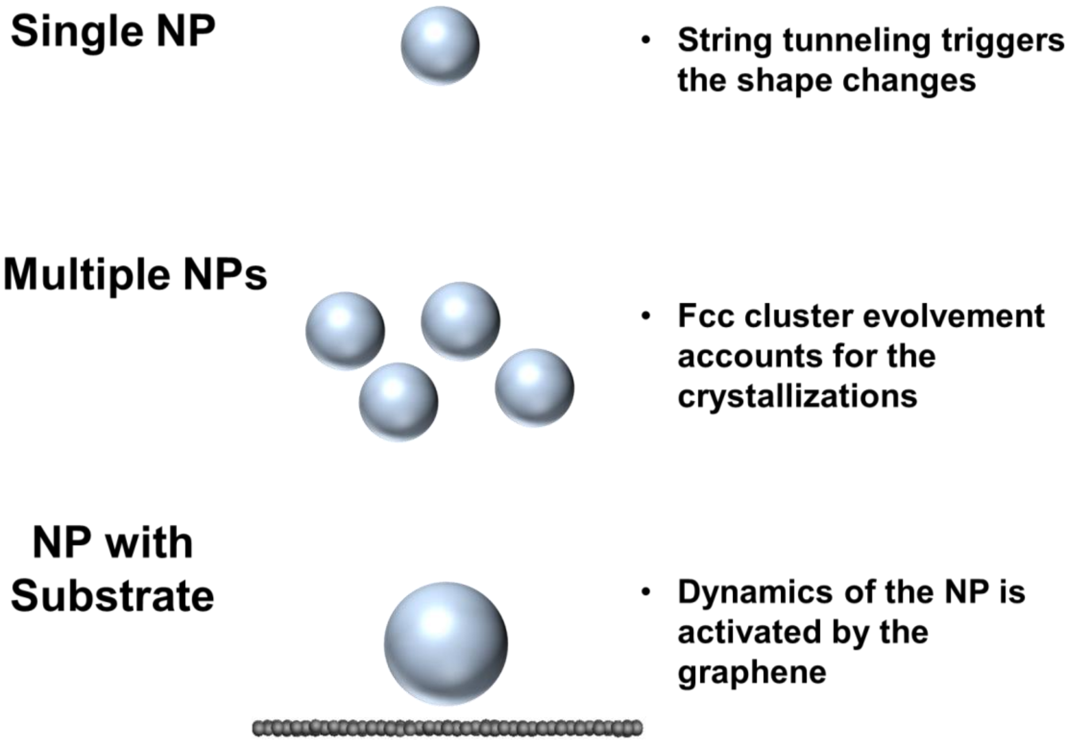

Figure 6.1 Summary of main conclusions in this thesis

According to the objectives we have listed In Chapter 1, now that we can conclude by completing the work in the thesis, we have understood and quantified the the atomic motions, especially the string-like atomic motions that govern the interfacial dynamics of NP during melting and crystallization, and the local structure changes for the single small NP, and the multiple small NP during the coalescence. What's more, we have explored and investigated the atomic motions and the interfacial dynamics for single NP under the constraint from the graphene substrate.

For the single ultra-small NP, we investigate the spontaneous shape changes of single N55 NP and revealed the mechanisms for its specific features of the large fluctuations and high atomic dynamics. It is found that the shape fluctuations are facilitated by the string-like collective motion taking a novel form, the tunnelling of atoms through the center of the NP which is highly disruptive to NP shape.

For the multiple NPs, we observe that the initial fcc cluster for each single *N55* NP breaks down upon coalescence, while the initial liquid-like surface atoms contribute the most for the final pure fcc structure. The phenomenon of the growing clusters gradually approaching the center results in the crystallization. It is the string-like atomic motion that accompanies the coalescence and the crystallization process, rather than the rotation of the NPs.

For the NP with the graphene substrate, we utilize another force field however the factor affecting the atomic dynamics in terms of the NP shape anisotropy is negligible. It shows the the variation for the local structure of the NP is much more temperature dependent using the HA index analysis while the graphene sheet has little temperature dependence regarding the configurations. the level crystallization of the NP affected by the substrate is always lower than the single NP indicating the substrate makes the NP more disordered and more active.

6.2 Contribution to Knowledge

Based on the MD simulation, the quantitative analyses and the results in this thesis and the related work of the atomic motions in Ni materials, the following papers have been published or are in preparation for submission,

a) **Y. Yang**, H. Zhang and J. Douglas, "Coalescence of Ultra Small Nanoparticles," in preparation for submitting.

b) H. Zhang, **Y. Yang** and J. Douglas, "Influence of String-like Cooperative Atomic Motion on Surface Diffusion in the (110) Interfacial Region of Crystalline Ni," *J. Chem. Phys.*, **142**, 084704 (2015).

c) **Y. Yang**, H. Zhang and J. Douglas, "Origin and Nature of Spontaneous Shape Fluctuations in 'Small' Nanoparticles," *ACS Nano*, **8**, 7465-7477 (2014).

Meanwhile, the work of the single NP has been presented in the session of “Computational Materials Science” in the 26th Canadian Materials Science Conference with the detail listed below,

Y. Yang, H. Zhang and J. Douglas, "Origin and Nature of Spontaneous Shape Fluctuations in Nanoparticles," 26th Canadian Materials Science Conference, Saskatoon, Canada, June 1-4, 2014.

6.3 Suggestions for the Future Work

6.3.1 Ni NPs using the Voter-Chen Potential

The shape fluctuations of the single small NP are evidently reminiscent of the shape fluctuations of proteins, organic nanoparticles, and these fluctuations could have important implications in relation to NP transport and the unique catalytic properties of nanoparticles. There is evidence that the interfacial mobility and large shape fluctuations of small NPs probably play a significant role in the formation of crystal nuclei through the fusion and structural rearrangement of the relatively disordered 'amorphous' pre-nucleation clusters[186, 187] and we expect an understanding of this type of fluctuating cluster to be essential for understanding the early stages of crystal growth that are not captured by classical nucleation theory. Such pre-nucleation 'amorphous' clusters have been shown to play an essential role in biomineralization processes in bones and teeth[188-192] where collagen and self-assembling proteins form scaffolds on which NPs are organized.

It also seems likely to us that the large shape fluctuations aid in the intrusion of these NPs into the small scaffold pore spaces into collagen and other organic self-assembled template materials.[193, 194] Large fluctuations in NP shape have also been suggested to contribute to the diffusion on small NPs.[195, 196] Clearly, small inorganic nanoparticles can exhibit large configuration fluctuations, and fluctuations in associated with chemical activity and properties, making these particles similar to proteins in many ways. This is natural given that proteins are just small *organic* nanoparticles. We plan to investigate the collective dynamics of folded globular proteins to see if they indeed exhibit a similar collective dynamics to that observed in our small Ni NPs. Previous work and the current study mainly focus on atomic species with simple London dispersion interactions and simple many body potentials for metallic atoms system such as Ni. These atomic potentials are isotropic in nature, raising interesting questions about how particles with strong cohesive and anisotropic interactions, such as charged and dipolar particle systems, might influence this NP shape fluctuation phenomenon. In order to address these questions, we must qualify our results as applying to interaction potentials of the type we study.

However, since the size and shape fluctuation are exhibited in variety of organic systems, we believe that materials exhibiting directional bonding should also exhibit such fluctuations in simulation. It is certainly true that simulations of atomics in charged glass-forming liquids exhibit string-like collective motion as we have found in the present work. On the other hand, we may generally expect that the critical particle NP size at which the NP size fluctuations arise should depend rather on the cohesive interaction strength and on the presence of directional interactions, a point highly relevant potentially in the context of NPs involved in biomineralization. Further study is needed to confirm these expectations for NPs with such interactions.

Finally, we point out that molecular dynamics simulations of water NPs having a size on the order of 1 nm[197] have indicated a large melting point suppression and dynamic coexistence between liquid and solid NP states, and we may naturally expect dynamic shape fluctuations in these NPs, a phenomenon of large potential relevance to the impact of these NPs on atmospheric chemistry.[197]

6.3.2 Graphene and Ni NP interactions using the Reaxff Reactive Force Field

Since in our metallic NP research this is the first time to introduce another type of inorganic specie (the graphene sheet) to the Ni NPs system, a lot of exploration challenges has been faced during the simulation model set up period. Apart from other statistical methods to identify and analyze the specific issues for the NP interacting with the substrate, we will also try to establish more inspirational scientific models in the future. NP coalescence is a major issue for NP catalysis. It has been attracting a lot of attention that by laying an array of nanoparticles on a graphene sheet[198, 199] and by applying surface X-ray crystallography, the atomic structure evolvement can accurately be determined. Questions remain that how many magnitude of the NP should be used to have the suitable catalysis effect and what's the suitable spatial distributions of the NPs as well as their orientaions. Also, the alloying for NPs is another vast research field for the catalysis applications, e.g. the ordered alloying and core-shell alloying. These have never been validated against experiment because of the lack of results from atomically resolved experiments such as this[199].

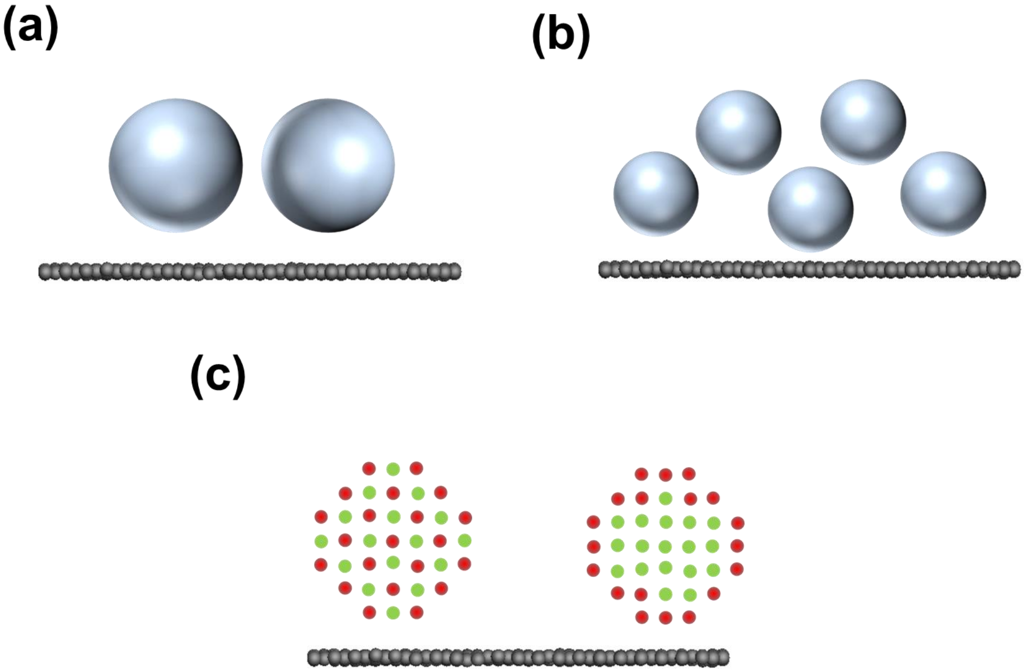

Figure 6.2 Scientific models for the graphene substrate supporting (a) the NPs with different orientations, (b) multiple NPs with different spatial arrangement and (c) NPs with ordered alloying and core-shell alloying

Consequently, we propose here for the future fundamental models when several examples are plotted. Figure 6.2a shows the graphene substrate supporting the NPs with different orientations, while Figure 6.2b represents multiple NPs with different spatial arrangement above the substrate; Last but not the least, Figure 6.2c gives insight into the NPs with ordered alloying and core-shell alloying while interacting with the graphene sheet. Furthermore, if the research moves on, it is also recommended to have a look at the rippled graphene sheet[200, 201] rather than the ideal flat one.

References

1. Li, Z. Y.; Young, N. P.; Di Vece, M.; Palomba, S.; Palmer, R. E.; Bleloch, a. L.; Curley, B. C.; Johnston, R. L.; Jiang, J.; Yuan, J. Three-Dimensional Atomic-Scale Structure of Size-Selected Gold Nanoclusters. *Nature* **2008**, 451, 46-48.
2. Xu, W.; Kong, J. S.; Chen, P. Probing the Catalytic Activity and Heterogeneity of Au-Nanoparticles at the Single-Molecule Level. *Phys. Chem. Chem. Phys.* **2009**, 11, 2767-2778.
3. Hughes, M. D.; Xu, Y.-J.; Jenkins, P.; McMorn, P.; Landon, P.; Enache, D. I.; Carley, A. F.; Attard, G. A.; Hutchings, G. J.; King, F.*, et al.* Tunable Gold Catalysts for Selective Hydrocarbon Oxidation under Mild Conditions. *Nature* **2005**, 437, 1132-1135.
4. Bovin, J.; Wallenberg, R.; Smith, D. J. Imaging of Atomic Clouds Outside the Surfaces of Gold Crystals by Electron Microscopy. *Nature* **1985**, 317, 47-49.
5. Marchak, D.; Glozman, D.; Vinshtein, Y.; Jarby, S.; Lereah, Y.; Cheshnovsky, O.; Selzer, Y. Large Anisotropic Conductance and Band Gap Fluctuations in Nearly Round-Shape Bismuth Nanoparticles. *Nano Lett.* **2012**, 12, 1087-1091.
6. Marchak, D.; Glozman, D.; Vinshtein, Y.; Jarby, S.; Lereah, Y.; Cheshnovsky, O.; Selzer, Y. Molecular Control of Structural Dynamics and Conductance Switching in Bismuth Nanoparticles. *J. Phys. Chem. C* **2013**, 117, 22218-22223.
7. Newton, M. A.; Belver-Coldeira, C.; Martínez-Arias, A.; Fernández-García, M. Dynamic in Situ Observation of Rapid Size and Shape Change of Supported Pd Nanoparticles During Co/No Cycling. *Nat. Mater.* **2007**, 6, 528-532.
8. Narayanan, R.; El-Sayed, M. A. Shape-Dependent Catalytic Activity of Platinum Nanoparticles in Colloidal Solution. *Nano Lett.* **2004**, 4, 1343-1348.
9. Yang, J.; Lee, J. Y.; Too, H.-P. Size Effect in Thiol and Amine Binding to Small Pt Nanoparticles. *Anal. Chim. Acta.* **2006**, 571, 206-210.

10. Hansen, P. L.; Wagner, J. B.; Helveg, S.; Rostrup-Nielsen, J. R.; Clausen, B. S.; Topsøe, H. Atom-Resolved Imaging of Dynamic Shape Changes in Supported Copper Nanocrystals. *Science* **2002**, 295, 2053-2055.

11. Helveg, S.; López-Cartes, C.; Sehested, J.; Hansen, P. L.; Clausen, B. S.; Rostrup-nielsen, J. R.; Abild-pedersen, F.; Nørskov, J. K. Atomic-Scale Imaging of Carbon Nanofibre Growth. *Nature* **2004**, 427, 426-429.

12. Feenstra, R. M.; Slavin, A. J.; Held, G. A.; Lutz, M. A. Edge Melting of the Ge(111) Surface Studied by Scanning Tunneling Microscopy. *Ultramicroscopy* **1992**, 42, 33-40.

13. Krakow, W.; Jóse-Yacamán, M.; Aragón, J. Observation of Quasimelting at the Atomic Level in Au Nanoclusters. *Phys. Rev. B* **1994**, 49, 10591-10596.

14. Ajayan, P.; Marks, L. Experimental Evidence for Quasimelting in Small Particles. *Phys. Rev. Lett.* **1989**, 63, 279-282.

15. Buffat, P.; Borel, J. P. Size Effect on Melting Temperature of Gold Particles. *Phys. Rev. A* **1976**, 13, 2287-2298.

16. Shvartsburg, A. A.; Jarrold, M. F. Solid Clusters above the Bulk Melting Point. *Phys. Rev. Lett.* **2000**, 85, 2530-2532.

17. Breaux, G. A.; Benirschke, R. C.; Sugai, T.; Kinnear, B. S.; Jarrold, M. F. Hot and Solid Gallium Clusters: Too Small to Melt. *Phys. Rev. Lett.* **2003**, 91.

18. Takagi, M. Electron-Diffraction Study of Liquid-Solid Transition of Thin Metal Films. *J. Phys. Soc. Jpn.* **1954**, 9, 359-363.

19. Coombes, C. J. Melting of Small Particles of Lead and Indium. *J Phys F Met Phys* **1972**, 2, 441-&.

20. Wronski, C. R. M. Size Dependence of Melting Point of Small Particles of Tin. *Brit J Appl Phys* **1967**, 18, 1731-&.

21. Peppiatt, S. J.; Sambles, J. R. Melting of Small Particles .1. Lead. *P Roy Soc Lond a Mat* **1975**, 345, 387-&.

22. Gladkich, N. T.; Niederma.R; Spiegel, K. Nachweis Grosser Schmelzpunktserniedrigungen Bei Dunnen Metallschichten. *Phys Status Solidi* **1966**, 15, 181-&.

23. SanchezLopez, J. C.; Fernandez, A.; Conde, C. F.; Conde, A.; Morant, C.; Sanz, J. M. The Melting Behavior of Passivated Nanocrystalline Aluminum. *Nanostruct Mater* **1996**, 7, 813-822.

24. Eckert, J.; Holzer, J.; Ahn, C.; Fu, Z.; Johnson, W. Melting Behavior of Nanocrystalline Aluminum Powders. **1993**, 2, 407-413.

25. Dippel, M.; Maier, A.; Gimple, V.; Wider, H.; Evenson, W. E.; Rasera, R. L.; Schatz, G. Size-Dependent Melting of Self-Assembled Indium Nanostructures. *Phys. Rev. Lett.* **2001**, 87, art. no.-095505.

26. Pocza, J. F.; Barna, A.; Barna, P. B. Formation Processes of Vacuum-Deposited Indium Films and Thermodynamical Properties of Submicroscopic Particles Observed by in Situ Electron Microscopy. *J Vac Sci Technol* **1969**, 6, 472-&.

27. Kofman, R.; Cheyssac, P.; Lereah, Y.; Stella, A. Melting of Clusters Approaching 0d. *Eur. Phys. J. D* **1999**, 9, 441-444.

28. Mei, Q. S.; Lu, K. Melting and Superheating of Crystalline Solids: From Bulk to Nanocrystals. *Prog Mater Sci* **2007**, 52, 1175-1262.

29. Allen, G. L.; Bayles, R. A.; Gile, W. W.; Jesser, W. A. Small Particle Melting of Pure Metals. *Thin Solid Films* **1986**, 144, 297-308.

30. Lai, S. L.; Guo, J. Y.; Petrova, V.; Ramanath, G.; Allen, L. H. Size-Dependent Melting Properties of Small Tin Particles: Nanocalorimetric Measurements. *Phys. Rev. Lett.* **1996**, 77, 99-102.

31. Peters, K. F.; Chung, Y. W.; Cohen, J. B. Surface Melting on Small Particles. *Appl. Phys. Lett.* **1997**, 71, 2391-2393.

32. Allen, G. L.; Gile, W. W.; Jesser, W. A. The Melting Temperature of Micro-Crystals Embedded in a Matrix. *Acta Metall. Mater.* **1980**, 28, 1695-1701.

33. Unruh, K. M.; Patterson, B. M.; Shah, S. I. Melting Behavior of Snx(Sio2)100-X Granular Metal-Films. *J. Mater. Res.* **1992**, 7, 214-218.

34. Sheng, H. W.; Lu, K.; Ma, E. Melting and Freezing Behavior of Embedded Nanoparticles in Ball-Milled Al-10 Wt% M (M = in, Sn, Bi, Cd, Pb) Mixtures. *Acta Mater.* **1998**, 46, 5195-5205.

35. Bhattacharya, P.; Chattopadhyay, K. Nano Al2o3-Pb and Sio2-Pb Cermets by Sol-Gel Technique and the Phase Transformation Study of the Embedded Pb Particles. *Nanostruct Mater* **1999**, 12, 1077-1080.

36. Lereah, Y.; Kofman, R.; Penisson, J. M.; Deutscher, G.; Cheyssac, P.; Ben David, T.; Bourret, A. Time-Resolved Electron Microscopy Studies of the Structure of Nanoparticles and Their Melting. *Philos. Mag. B* **2001**, 81, 1801-1819.

37. Qi, Y.; Cagin, T.; Johnson, W. L.; Goddard, W. A. Melting and Crystallization in Ni Nanoclusters: The Mesoscale Regime. *J. Chem. Phys.* **2001**, 115, 385-394.

38. Schebarchov, D.; Hendy, S. C. Static, Transient, and Dynamic Phase Coexistence in Metal Nanoclusters. *J. Chem. Phys.* **2005**, 123.

39. Yacaman, M. J.; Ascencio, J. A.; Liu, H. B.; Gardea-Torresdey, J. Structure Shape and Stability of Nanometric Sized Particles. *J Vac Sci Technol B* **2001**, 19, 1091-1103.

40. Sun, D. Y.; Gong, X. G. Structural Properties and Glass Transition in Al-N Clusters. *Phys. Rev. B* **1998**, 57, 4730-4735.

41. Cheng, H. P.; Berry, R. S. Surface Melting of Clusters and Implications for Bulk Matter. *Phys. Rev. A* **1992**, 45, 7969-7980.

42. Hu, W. Y.; Xiao, S. G.; Yang, J. Y.; Zhang, Z. Melting Evolution and Diffusion Behavior of Vanadium Nanoparticles. *Eur. Phys. J. B* **2005**, 45, 547-554.

43. Wang, N. Y.; Rokhlin, S. I.; Farson, D. F. Nonhomogeneous Surface Premelting of Au Nanoparticles. *Nanotechnology* **2008**, 19.

44. Alavi, S.; Thompson, D. L. Molecular Dynamics Simulations of the Melting of Aluminum Nanoparticles. *J. Phys. Chem. A* **2006**, 110, 1518-1523.

45. Cleveland, C. L.; Luedtke, W. D.; Landman, U. Melting of Gold Clusters. *Phys Rev B* **1999**, 60, 5065-5077.

46. Calvo, F.; Spiegelmann, F. Geometric Size Effects in the Melting of Sodium Clusters. *Phys. Rev. Lett.* **1999**, 82, 2270-2273.

47. Ding, F.; Bolton, K.; Rosen, A. Molecular Dynamics Study of the Surface Melting of Iron Clusters. *Eur. Phys. J. D* **2005**, 34, 275-277.

48. Atwater, H. A.; Yang, C. M. Island Growth and Coarsening in Thin-Films - Conservative and Nonconservative Systems. *J. Appl. Phys.* **1990**, 67, 6202-6213.

49. Petrov, I.; Barna, P. B.; Hultman, L.; Greene, J. E. Microstructural Evolution During Film Growth. *J Vac Sci Technol A* **2003**, 21, S117-S128.

50. Magnfalt, D.; Elofsson, V.; Abadias, G.; Helmersson, U.; Sarakinos, K. Time-Domain and Energetic Bombardment Effects on the Nucleation and Coalescence of Thin Metal Films on Amorphous Substrates. *J Phys D Appl Phys* **2013**, 46.

51. Lim, T. H.; McCarthy, D.; Hendy, S. C.; Stevens, K. J.; Brown, S. A.; Tilley, R. D. Real-Time Tem and Kinetic Monte Carlo Studies of the Coalescence of Decahedral Gold Nanoparticles. *ACS Nano* **2009**, 3, 3809-3813.

52. José-Yacaman, M.; Gutierrez-Wing, C.; Miki, M.; Yang, D. Q.; Piyakis, K. N.; Sacher, E. Surface Diffusion and Coalescence of Mobile Metal Nanoparticles. *J. Phys. Chem. B* **2005**, 109, 9703-9711.

53. Moon, Y. K.; Lee, J. K.; Kim, J. G.; Jung, M. Y.; Lee, J. B.; Kim, S. H. Sintering Kinetic Measurement of Nickel Nanoparticle Agglomerates by Electrical Mobility Classification. *Curr. Appl. Phys.* **2009**, 9, 928-932.

54. Niu, K. Y.; Liao, H. G.; Zheng, H. M. Visualization of the Coalescence of Bismuth Nanoparticles. *Microsc. Microanal.* **2014**, 20, 416-424.

55. Nakaso, K.; Shimada, M.; Okuyama, K.; Deppert, K. Evaluation of the Change in the Morphology of Gold Nanoparticles During Sintering. *J. Aerosol Sci.* **2002**, 33, 1061-1074.

56. Lewis, L. J.; Jensen, P.; Barrat, J. L. Melting, Freezing, and Coalescence of Gold Nanoclusters. *Phys. Rev. B* **1997**, 56, 2248-2257.

57. Arcidiacono, S.; Bieri, N. R.; Poulikakos, D.; Grigoropoulos, C. P. On the Coalescence of Gold Nanoparticles. *Int. J. Multiphas. Flow* **2004**, 30, 979-994.

58. Ding, F.; Rosen, A.; Bolton, K. Size Dependence of the Coalescence and Melting of Iron Clusters: A Molecular-Dynamics Study. *Phys. Rev. B* **2004**, 70, 075416.

59. Jiang, S.; Zhang, Y. W.; Gan, Y.; Chen, Z.; Peng, H. Molecular Dynamics Study of Neck Growth in Laser Sintering of Hollow Silver Nanoparticles with Different Heating Rates. *J. Phys. D Appl. Phys.* **2013**, 46, 335302.

60. Guo, J. Y.; Xu, C. X.; Hu, A. M.; Oakes, K. D.; Sheng, F. Y.; Shi, Z. L.; Dai, J.; Jin, Z. L. Sintering Dynamics and Thermal Stability of Novel Configurations of Ag Clusters. *J. Phys. Chem. Solids* **2012**, 73, 1350-1357.

61. Li, G. J.; Wang, Q.; Liu, T.; Wang, K.; He, J. C. Molecular Dynamics Simulation of the Melting and Coalescence in the Mixed Cu-Ni Nanoclusters. *J. Clust. Sci.* **2010**, 21, 45-55.

62. Subbaraman, R.; Sankaranarayanan, S. K. R. S. Momentum Induced Coalescence and Alloying of Fe-Ni Nanoclusters: A Molecular Dynamics Simulation Study. *Chem. Phys. Lett.* **2012**, 522, 56-61.

63. Grammatikopoulos, P.; Cassidy, C.; Singh, V.; Sowwan, M. Coalescence-Induced Crystallisation Wave in Pd Nanoparticles. *Sci. Rep.* **2014**, 4, 5779.

64. Hendy, S.; Brown, S. A.; Hyslop, M. Coalescence of Nanoscale Metal Clusters: Molecular-Dynamics Study. *Phys. Rev. B* **2003**, 68, 241403.

65. Cheng, B. Q.; Ngan, A. H. W. The Crystal Structures of Sintered Copper Nanoparticles: A Molecular Dynamics Study. *Int. J. Plasticity* **2013**, 47, 65-79.

66. Grammatikopoulos, P.; Cassidy, C.; Singh, V.; Benelmekki, M.; Sowwan, M. Coalescence Behaviour of Amorphous and Crystalline Tantalum Nanoparticles: A Molecular Dynamics Study. *J. Mater. Sci.* **2014**, 49, 3890-3897.

67. Liu, C. M.; Xu, C.; Cheng, Y.; Chen, X. R.; Cai, L. C. Size-Dependent Melting and Coalescence of Tungsten Nanoclusters Via Molecular Dynamics Simulation. *Phys. Chem. Chem. Phys.* **2013**, 15, 14069-14079.

68. Koparde, V. N.; Cummings, P. T. Phase Transformations During Sintering of Titania Nanoparticles. *ACS Nano* **2008**, 2, 1620-1624.

69. Koparde, V. N.; Cummings, P. T. Sintering of Titanium Dioxide Nanoparticles: A Comparison between Molecular Dynamics and Phenomenological Modeling. *J. Nanopart. Res.* **2008**, 10, 1169-1182.

70. Fang, Z. Z.; Wang, H. Densification and Grain Growth During Sintering of Nanosized Particles. *Int. Mater. Rev.* **2008**, 53, 326-352.

71. Ding, L. F.; Davidchack, R. L.; Pan, J. Z. A Molecular Dynamics Study of Sintering between Nanoparticles. *Comp. Mater. Sci.* **2009**, 45, 247-256.

72. Carrillo, J. M. Y.; Dobrynin, A. V. Contact Mechanics of Nanoparticles. *Langmuir* **2012**, 28, 10881-10890.

73. Koparde, V. N.; Cummings, P. T. Molecular Dynamics Simulation of Titanium Dioxide Nanoparticle Sintering. *J. Phys. Chem. B* **2005**, 109, 24280-24287.

74. Oliveira, M. M.; Ugarte, D.; Zanchet, D.; Zarbin, A. J. G. Influence of Synthetic Parameters on the Size, Structure, and Stability of Dodecanethiol-Stabilized Silver Nanoparticles. *J Colloid Interf Sci* **2005**, 292, 429-435.

75. Bai, J.; Li, Y.; Du, J.; Wang, S.; Zheng, J.; Yang, Q.; Chen, X. One-Pot Synthesis of Polyacrylamide-Gold Nanocomposite. *Mater. Chem. Phys.* **2007**, 106, 412-415.

76. Ding, M. Y.; Yang, Y.; Wu, B. S.; Wang, T. J.; Xiang, H. W.; Li, Y. W. Effect of Reducing Agents on Microstructure and Catalytic Performance of Precipitated Iron-Manganese Catalyst for Fischer-Tropsch Synthesis. *Fuel Process. Technol.* **2011**, 92, 2353-2359.

77. Richardson, Y.; Blin, J.; Volle, G.; Motuzas, J.; Julbe, A. In Situ Generation of Ni Metal Nanoparticles as Catalyst for H-2-Rich Syngas Production from Biomass Gasification. *Appl Catal a-Gen* **2010**, 382, 220-230.

78. Shen, Y. F.; Areeprasert, C.; Prabowo, B.; Takahashi, F.; Yoshikawa, K. Metal Nickel Nanoparticles in Situ Generated in Rice Husk Char for Catalytic Reformation of Tar and Syngas from Biomass Pyrolytic Gasification. *Rsc Adv* **2014**, 4, 40651-40664.

79. Somorjai, G. A.; Chaudret, B.; Serp, P.; Philippot, K. *Nanomaterials in Catalysis*. John Wiley & Sons: **2012**.

80. Simon, P.; Gogotsi, Y. Materials for Electrochemical Capacitors. *Nat Mater* **2008**, 7, 845-854.

81. Kato, T.; Hatakeyama, R. Site- and Alignment-Controlled Growth of Graphene Nanoribbons from Nickel Nanobars. *Nat. Nanotechnol.* **2012**, 7, 651-656.

82. Sun, Z. Z.; Yan, Z.; Yao, J.; Beitler, E.; Zhu, Y.; Tour, J. M. Growth of Graphene from Solid Carbon Sources. *Nature* **2010**, 468, 549-552.

83. Wang, H. L.; Robinson, J. T.; Diankov, G.; Dai, H. J. Nanocrystal Growth on Graphene with Various Degrees of Oxidation. *J Am Chem Soc* **2010**, 132, 3270.

84. Yamamoto, K.; Imaoka, T.; Chun, W. J.; Enoki, O.; Katoh, H.; Takenaga, M.; Sonoi, A. Size-Specific Catalytic Activity of Platinum Clusters Enhances Oxygen Reduction Reactions. *Nat Chem* **2009**, 1, 397-402.

85. Costamagna, P.; Srinivasan, S. Quantum Jumps in the Pemfc Science and Technology from the 1960s to the Year 2000 Part I. Fundamental Scientific Aspects. *J. Power Sources* **2001**, 102, 242-252.

86. Shao, Y. Y.; Yin, G. P.; Wang, Z. B.; Gao, Y. Z. Proton Exchange Membrane Fuel Cell from Low Temperature to High Temperature: Material Challenges. *J. Power Sources* **2007**, 167, 235-242.

87. Donati, C.; Douglas, J.; Kob, W.; Plimpton, S.; Poole, P.; Glotzer, S. Stringlike Cooperative Motion in a Supercooled Liquid. *Phys. Rev. Lett.* **1998**, 80, 2338-2341.

88. Zhang, H.; Kalvapalle, P.; Douglas, J. F. String-Like Collective Atomic Motion in the Interfacial Dynamics of Nanoparticles. *Soft Matter* **2010**, 6, 5944-5955.

89. Debenedetti, P. G.; Stillinger, F. H. Supercooled Liquids and the Glass Transition. *Nature* **2001**, 410, 259-267.

90. Angell, C. A.; Tucker, J. C. Heat-Capacities and Fusion Entropies of Tetrahydrates of Calcium Nitrate, Cadmium Nitrate, and Magnesium Acetate - Concordance of Calorimetric and Relaxational Ideal Glass-Transition Temperatures. *J Phys Chem-Us* **1974**, 78, 278-281.

91. Lubchenko, V.; Wolynes, P. G. Theory of Structural Glasses and Supercooled Liquids. *Annu. Rev. Phys. Chem.* **2007**, 58, 235-266.

92. Ediger, M. D.; Angell, C. A.; Nagel, S. R. Supercooled Liquids and Glasses. *J Phys Chem-Us* **1996**, 100, 13200-13212.

93. Berthier, L.; Biroli, G. Theoretical Perspective on the Glass Transition and Amorphous Materials. *Rev Mod Phys* **2011**, 83, 587-645.

94. Adam, G.; Gibbs, J. H. On Temperature Dependence of Cooperative Relaxation Properties in Glass-Forming Liquids. *J. Chem. Phys.* **1965**, 43, 139-146.

95. Besenbacher, F.; Chorkendorff, I.; Clausen, B. S.; Hammer, B.; Molenbroek, A. M.; Norskov, J. K.; Stensgaard, I. Design of a Surface Alloy Catalyst for Steam Reforming. *Science* **1998**, 279, 1913-1915.

96. Chen, D.; Liu, S.; Li, J. J.; Zhao, N. Q.; Shi, C. S.; Du, X. W.; Sheng, J. Nanometre Ni and Core/Shell Ni/Au Nanoparticles with Controllable Dimensions Synthesized in Reverse Microemulsion. *J Alloy Compd* **2009**, 475, 494-500.

97. Dipti, S. S.; Chung, U. C.; Kim, J. P.; Chung, W. S. Different Nanostructure Cathode Catalysts Application for Direct Methanol Fuel Cell. *Phys. Status Solidi A* **2007**, 204, 4174-4177.

98. Vang, R. T.; Honkala, K.; Dahl, S.; Vestergaard, E. K.; Schnadt, J.; Laegsgaard, E.; Clausen, B. S.; Norskov, J. K.; Besenbacher, F. Controlling the Catalytic Bond-Breaking Selectivity of Ni Surfaces by Step Blocking. *Nat Mater* **2005**, 4, 160-162.

99. Park, K. W.; Choi, J. H.; Kwon, B. K.; Lee, S. A.; Sung, Y. E.; Ha, H. Y.; Hong, S. A.; Kim, H.; Wieckowski, A. Chemical and Electronic Effects of Ni in Pt/Ni and Pt/Ru/Ni Alloy Nanoparticles in Methanol Electrooxidation. *J. Phys. Chem. B* **2002**, 106, 1869-1877.

100. Zhang, H.; Srolovitz, D. J.; Douglas, J. F.; Warren, J. A. Grain Boundaries Exhibit the Dynamics of Glass-Forming Liquids. *Proc. Natl. Acad. Sci. U.S.A.* **2009**, 106, 7735-7740.

101. Kang, J.; Kim, Y. H. Half-Solidity of Tetrahedral-Like Al-55 Clusters. *ACS Nano* **2010**, 4, 1092-1098.

102. Zhang, Z.; Hu, W.; Xiao, S. Melting, Melting Competition, and Structural Transitions between Shell-Closed Icosahedral and Octahedral Nickel Nanoclusters. *Phys. Rev. B* **2006**, 73, 125443.

103. Uppenbrink, J.; Wales, D. J. Packing Schemes for Lennard-Jones Clusters of 13 to 150 Atoms: Minima, Transition-States and Rearrangement Mechanisms. *J. Chem. Soc. Faraday T.* **1991**, 87, 215-222.

104. Wales, D. J.; Munro, L. J. Changes of Morphology and Capping of Model Transition Metal Clusters. *J. Phys. Chem.* **1996**, 100, 2053-2061.

105. Wales, D. J.; Munro, L. J.; Doye, J. P. K. What Can Calculations Employing Empirical Potentials Teach Us About Bare Transition-Metal Clusters? *J. Chem. Soc. Dalton Trans.* **1996**, 611-623.

106. Calvo, F.; Doye, J. P. K.; Wales, D. J. Energy Landscapes of Colloidal Clusters: Thermodynamics and Rearrangement Mechanisms. *Nanoscale* **2012**, 4, 1085-1100.

107. Neyts, E. C.; Bogaerts, A. Numerical Study of the Size-Dependent Melting Mechanisms of Nickel Nanoclusters. *J. Phys. Chem. C* **2009**, 113, 2771-2776.

108. Daw, M. S.; Baskes, M. I. Embedded-Atom Method - Derivation and Application to Impurities, Surfaces, and Other Defects in Metals. *Phys Rev B* **1984**, 29, 6443-6453.

109. Voter, A. F.; Chen, S. P. In *Accurate Interatomic Potentials for Ni, Al and Ni3al*, MRS Proceedings, Cambridge Univ Press: **1986**.

110. Mishin, Y.; Mehl, M. J.; Papaconstantopoulos, D. A. Embedded-Atom Potential for B2-Nial. *Phys Rev B* **2002**, 65.

111. Tadmor, E. B.; Miller, R. E. *Modeling Materials: Continuum, Atomistic and Multiscale Techniques*. Cambridge University Press: **2011**.

112. van Duin, A. C. T.; Dasgupta, S.; Lorant, F.; Goddard, W. A. Reaxff: A Reactive Force Field for Hydrocarbons. *J. Phys. Chem. A* **2001**, 105, 9396-9409.

113. Buehler, M. J.; Tang, H.; van Duin, A. C. T.; Goddard, W. A. Threshold Crack Speed Controls Dynamical Fracture of Silicon Single Crystals. *Phys. Rev. Lett.* **2007**, 99.

114. Zhang, Q.; Cagin, T.; van Duin, A.; Goddard, W. A.; Qi, Y.; Hector, L. G. Adhesion and Nonwetting-Wetting Transition in the Al/Alpha-Al2o3 Interface. *Phys Rev B* **2004**, 69.

115. Ludwig, J.; Vlachos, D. G.; van Duin, A. C. T.; Goddard, W. A. Dynamics of the Dissociation of Hydrogen on Stepped Platinum Surfaces Using the Reaxff Reactive Force Field. *J. Phys. Chem. B* **2006**, 110, 4274-4282.

116. Sanz-Navarro, C. F.; Astrand, P. O.; Chen, D.; Ronning, M.; van Duin, A. C. T.; Jacob, T.; Goddard, W. A. Molecular Dynamics Simulations of the Interactions between Platinum Clusters and Carbon Platelets. *J. Phys. Chem. A* **2008**, 112, 1392-1402.

117. Han, S. S.; Kang, J. K.; Lee, H. M.; van Duin, A. C. T.; Goddard, W. A. The Theoretical Study on Interaction of Hydrogen with Single-Walled Boron Nitride Nanotubes. I. The Reactive Force Field Reaxff(Hbn) Development. *J. Chem. Phys.* **2005**, 123.

118. van Duin, A. C. T.; Merinov, B. V.; Jang, S. S.; Goddard, W. A. Reaxff Reactive Force Field for Solid Oxide Fuel Cell Systems with Application to Oxygen Ion Transport in Yttria-Stabilized Zirconia. *J. Phys. Chem. A* **2008**, 112, 3133-3140.

119. Su, H. B.; Nielsen, R. J.; van Duin, A. C. T.; Goddard, W. A. Simulations on the Effects of Confinement and Ni-Catalysis on the Formation of Tubular Fullerene Structures from Peapod Precursors. *Phys Rev B* **2007**, 75.

120. Sanz-Navarro, C. F.; Astrand, P. O.; Chen, D.; Ronning, M.; van Duin, A. C. T.; Mueller, J. E.; Goddard, W. A. Molecular Dynamics Simulations of Carbon-Supported Ni Clusters Using the Reax Reactive Force Field. *J. Phys. Chem. C* **2008**, 112, 12663-12668.

121. Sanz-Navarro, C. F.; Astrand, P. O.; Chen, D.; Ronning, M.; van Duin, A. C. T.; Goddard, W. A. Molecular Dynamics Simulations of Metal Clusters Supported on Fishbone Carbon Nanofibers. *J. Phys. Chem. C* **2010**, 114, 3522-3530.

122. Neyts, E. C.; van Duin, A. C. T.; Bogaerts, A. Formation of Single Layer Graphene on Nickel under Far-from-Equilibrium High Flux Conditions. *Nanoscale* **2013**, 5, 7250-7255.

123. Nielson, K. D.; van Duin, A. C. T.; Oxgaard, J.; Deng, W. Q.; Goddard, W. A. Development of the Reaxff Reactive Force Field for Describing Transition Metal Catalyzed Reactions, with Application to the Initial Stages of the Catalytic Formation of Carbon Nanotubes. *J. Phys. Chem. A* **2005**, 109, 493-499.

124. Nose, S. A Unified Formulation of the Constant Temperature Molecular-Dynamics Methods. *J. Chem. Phys.* **1984**, 81, 511-519.

125. Hoover, W. G. Canonical Dynamics - Equilibrium Phase-Space Distributions. *Phys. Rev. A* **1985**, 31, 1695-1697.

126. Berendsen, H. J. C.; Postma, J. P. M.; Vangunsteren, W. F.; Dinola, A.; Haak, J. R. Molecular-Dynamics with Coupling to an External Bath. *J. Chem. Phys.* **1984**, 81, 3684-3690.

127. Morishita, T. Fluctuation Formulas in Molecular-Dynamics Simulations with the Weak Coupling Heat Bath. *J. Chem. Phys.* **2000**, 113, 2976-2982.

128. Šolc, K. Shape of a Random Flight Chain. *J. Chem. Phys.* **1971**, 55, 335-344.

129. Šolc, K.; Stockmayer, W. H. Shape of a Random ‐ Flight Chain. *J. Chem. Phys.* **1971**, 54, 2756-2757.

130. Šolc, K. Statistical Mechanics of Random-Flight Chains. Iv. Size and Shape Parameters of Cyclic, Star-Like, and Comb-Like Chains. *Macromol.* **1973**, 6, 378-385.

131. Flory, P. *Principles of Polymer Chemistry*. Cornell Univ Press: Ithaca, N. Y., **1953**.

132. Flory, P.; Volkenstein, M. *Statistical Mechanics of Chain Molecules*. Interscience: N. Y., **1969**.

133. Simmons, D. S.; Cicerone, M. T.; Zhong, Q.; Tyagi, M.; Douglas, J. F. Generalized Localization Model of Relaxation in Glass-Forming Liquids. *Soft Matter* **2012**, 8, 11455-11461.

134. Honeycutt, J. D.; Andersen, H. C. Molecular-Dynamics Study of Melting and Freezing of Small Lennard-Jones Clusters. *J. Phys. Chem.* **1987**, 91, 4950-4963.

135. Xiong, L. H.; Lou, H. B.; Wang, X. D.; Debela, T. T.; Cao, Q. P.; Zhang, D. X.; Wang, S. Y.; Wang, C. Z.; Jiang, J. Z. Evolution of Local Atomic Structure During Solidification of Al2au Liquid: An Ab Initio Study. *Acta Mater.* **2014**, 68, 1-8.

136. Chen, S. D.; Soh, A. K.; Ke, F. J. Molecular Dynamics Modeling of Diffusion Bonding. *Scripta Mater.* **2005**, 52, 1135-1140.

137. Ganesh, P.; Widom, M. Signature of Nearly Icosahedral Structures in Liquid and Supercooled Liquid Copper. *Phys. Rev. B* **2006**, 74, 134205.

138. https://www.icts.res.in/.../1267683658Walter-Kob-5Jan-Lecture1.pdf (Date Accessed 30/09/2015)

139. Starr, F. W.; Douglas, J. F.; Sastry, S. The Relationship of Dynamical Heterogeneity to the Adam-Gibbs and Random First-Order Transition Theories of Glass Formation. *J. Chem. Phys.* **2013**, 138, 12A541.

140. Hanakata, P. Z.; Douglas, J. F.; Starr, F. W. Local Variation of Fragility and Glass Transition Temperature of Ultra-Thin Supported Polymer Films. *J. Chem. Phys.* **2012**, 137, 244901.

141. Zhang, H.; Khalkhali, M.; Liu, Q. X.; Douglas, J. F. String-Like Cooperative Motion in Homogeneous Melting. *J. Chem. Phys.* **2013**, 138, 12A538.

142. Zhang, H.; Douglas, J. F. Glassy Interfacial Dynamics of Ni Nanoparticles: Part Ii Discrete Breathers as an Explanation of Two-Level Energy Fluctuations. *Soft Matter* **2013**, 9, 1266-1280.

143. Zhang, H.; Douglas, J. F. Glassy Interfacial Dynamics of Ni Nanoparticles: Part I Colored Noise, Dynamic Heterogeneity and Collective Atomic Motion. *Soft Matter* **2013**, 9, 1254-1265.

144. Donati, C.; Glotzer, S. C.; Poole, P. H.; Kob, W.; Plimpton, S. J. Spatial Correlations of Mobility and Immobility in a Glass-Forming Lennard-Jones Liquid. *Phys. Rev. E* **1999**, 60, 3107-3119.

145. Riggleman, R.; Yoshimoto, K.; Douglas, J.; de Pablo, J. Influence of Confinement on the Fragility of Antiplasticized and Pure Polymer Films. *Phys. Rev. Lett.* **2006**, 97, 045502.

146. Starr, F. W.; Hartmann, B.; Douglas, J. F. Dynamical Clustering and a Mechanism for Raft-Like Structures in a Model Lipid Membrane. *Soft Matter* **2014**, 10, 3036-3047.

147. Wales, D. J.; Doye, J. P. K. Dynamics and Thermodynamics of Supercooled Liquids and Glasses from a Model Energy Landscape. *Phys. Rev. B* **2001**, 63, 214204.

148. Keys, A. S.; Abate, A. R.; Glotzer, S. C.; Durian, D. J. Measurement of Growing Dynamical Length Scales and Prediction of the Jamming Transition in a Granular Material. *Nat. Phys.* **2007**, 3, 260-264.

149. Dudowicz, J.; Freed, K. F.; Douglas, J. F. Fragility of Glass-Forming Polymer Liquids. *J. Phys. Chem. B* **2005**, 109, 21350-21356.

150. Wales, D. J.; McKay, H.; Altschuler, E. L. Defect Motifs for Spherical Topologies. *Phys. Rev. B* **2009**, 79, 224115.

151. Zhang, H.; Srolovitz, D. J.; Douglas, J. F.; Warren, J. A. Characterization of Atomic Motion Governing Grain Boundary Migration. *Phys. Rev. B* **2006**, 74, 115404.

152. Lee, S. G.; Chung, Y. C. Atomic-Level Investigation of Al and Ni Thin Film Growth on Ni(111) Surface: Molecular Dynamics Simulation. *Appl. Surf. Sci.* **2007**, 253, 8896-8900.

153. Mishin, Y.; Farkas, D.; Mehl, M. J.; Papaconstantopoulos, D. A. Interatomic Potentials for Monoatomic Metals from Experimental Data and Ab Initio Calculations. *Phys. Rev. B* **1999**, 59, 3393-3407.

154. Chen, S. P.; Voter, A. F.; Srolovitz, D. J. Oscillatory Surface Relaxations in Ni, Al, and Their Ordered Alloys. *Phys. Rev. Lett.* **1986**, 57, 1308-1311.

155. Doye, J. P. K.; Wales, D. J. Global Minima for Transition Metal Clusters Described by Sutton-Chen Potentials. *New J. Chem.* **1998**, 22, 733-744.

156. Chamati, H.; Gaminchev, K. Crystallization of Nickel Nanoclusters by Molecular Dynamics. *J. Phys. Conf. Ser.* **2012**, 398.

157. Parks, E. K.; Zhu, L.; Ho, J.; Riley, S. J. The Structure of Small Nickel Clusters. Ii. Ni-16-Ni-28. *J. Chem. Phys.* **1995**, 102, 7377-7389.

158. Parks, E. K.; Riley, S. J. Nickel Cluster Structure Determined from the Adsorption of Molecular Nitrogen - Ni-49-Ni-71. *Z. Phys. D Atom. Mol. Cl.* **1995**, 33, 59-70.

159. Mendelev, M. I.; Zhang, H.; Srolovitz, D. J. Grain Boundary Self-Diffusion in Ni: Effect of Boundary Inclination. *J. Mater. Res.* **2005**, 20, 1146-1153.

160. Wales, D. J.; Berry, R. S. Coexistence in Finite Systems. *Phys. Rev. Lett.* **1994**, 73, 2875-2878.

161. Wales, D. J.; Berry, R. S. Melting and Freezing of Small Argon Clusters. *J. Chem. Phys.* **1990**, 92, 4283-4295.

162. Wales, D. J. Transition States for Ar55. *Chem. Phys. Lett.* **1990**, 166, 419-424.

163. Davis, H. L.; Jellinek, J.; Berry, R. S. Melting and Freezing in Isothermal Ar13 Clusters. *J. Chem. Phys.* **1987**, 86, 6456-6464.

164. Wales, D. J. Instantaneous Normal Mode Analysis and Coexistence Phenomena in Small Clusters. *J. Chem. Soc. Faraday T.* **1991**, 87, 2399-2405.

165. Kunz, R. E.; Berry, R. S. Coexistence of Multiple Phases in Finite Systems. *Phys. Rev. Lett.* **1993**, 71, 3987-3990.

166. Berry, R. S. Melting and Freezing Phenomena. *Microscale Therm. Eng.* **1997**, 1, 1-18.

167. Berry, R. S.; Smirnov, B. A. Observability of Coexisting Phases of Clusters. *Int. J. Mass Spectrom.* **2009**, 280, 204-208.

168. Berry, R. S.; Smirnov, B. M. Bridging the Macro and Micro. *Chem. Phys. Lett.* **2013**, 573, 1-4.

169. Wales, D. J.; Doye, J. P. K. Coexistence and Phase-Separation in Clusters - from the Small to the Not-So-Small Regime. *J. Chem. Phys.* **1995**, 103, 3061-3070.

170. Zhang, H.; Kalvapalle, P.; Douglas, J. F. String-Like Collective Atomic Motion in the Melting and Freezing of Nanoparticles. *J. Phys. Chem. B* **2011**, 115, 14068-14076.

171. Zhang, Z.; Li, J. C.; Jiang, Q. Modelling for Size-Dependent and Dimension-Dependent Melting of Nanocrystals. *J. Phys. D: Appl. Phys.* **2000**, 33, 2653-2656.

172. Aguado, A.; Jarrold, M. F. Melting and Freezing of Metal Clusters. *Annu. Rev. Phys. Chem.* **2011**, 62, 151-172.

173. Joshi, K.; Krishnamurty, S.; Kanhere, D. G. "Magic Melters" Have Geometrical Origin. *Phys. Rev. Lett.* **2006**, 96, 135703.

174. Schmidt, M.; Kusche, R.; von Issendorff, B.; Haberland, H. Irregular Variations in the Melting Point of Size-Selected Atomic Clusters. *Nature* **1998**, 393, 238-240.

175. Noya, E. G.; Doye, J. P. K.; Wales, D. J.; Aguado, A. Geometric Magic Numbers of Sodium Clusters: Interpretation of the Melting Behaviour. *Eur. Phys. J. D* **2007**, 43, 57-60.

176. Jellinek, J.; Beck, T. L.; Berry, R. S. Solid–Liquid Phase Changes in Simulated Isoenergetic Ar13. *J. Chem. Phys.* **1986**, 84, 2783-2794.

177. Jellinek, J.; Goldberg, A. On the Temperature, Equipartition, Degrees of Freedom, and Finite Size Effects: Application to Aluminum Clusters. *J. Chem. Phys.* **2000**, 113, 2570-2582.

178. Trygubenko, S. A.; Wales, D. J. Analysis of Cooperativity and Localization for Atomic Rearrangements. *J. Chem. Phys.* **2004**, 121, 6689-6697.

179. de Souza, V. K.; Wales, D. J. Energy Landscapes for Diffusion: Analysis of Cage-Breaking Processes. *J. Chem. Phys.* **2008**, 129, 164507.

180. Yang, Y.; Zhang, H.; Douglas, J. F. Origin and Nature of Spontaneous Shape Fluctuations in "Small" Nanoparticles. *ACS Nano* **2014**, 8, 7465-7477.

181. The Rise and Rise of Graphene. *Nat. Nanotechnol.* **2010**, 5, 755-755.

182. Geim, A. K.; Novoselov, K. S. The Rise of Graphene. *Nat Mater* **2007**, 6, 183-191.

183. Kim, Y.; Lee, J.; Yeom, M. S.; Shin, J. W.; Kim, H.; Cui, Y.; Kysar, J. W.; Hone, J.; Jung, Y.; Jeon, S.*, et al.* Strengthening Effect of Single-Atomic-Layer Graphene in Metal-Graphene Nanolayered Composites. *Nat Commun* **2013**, 4.

184. Sinitsa, A. S.; Lebedeva, I. V.; Knizhnik, A. A.; Popov, A. M.; Skowron, S. T.; Bichoutskaia, E. Formation of Nickel-Carbon Heterofullerenes under Electron Irradiation. *Dalton T* **2014**, 43, 7499-7513.

185. http://www.jcrystal.com/products/wincnt/ (Date Accessed 30/09/2015)

186. Wang, L.; Peng, C.; Wang, Y.; Zhang, Y. Relating Nucleation to Dynamical and Structural Heterogeneity in Supercooled Liquid Metal. *Phys. Lett. A* **2006**, 350, 69-74.

187. Zhang, T. H.; Liu, X. Y. How Does a Transient Amorphous Precursor Template Crystallization. *J. Am. Chem. Soc.* **2007**, 129, 13520-13526.

188. Posner, A. S.; Betts, F. Synthetic Amorphous Calcium Phosphate and Its Relation to Bone Mineral Structure. *Acc. Chem. Res.* **1975**, 8, 273-281.

189. Deshpande, A. S.; Fang, P.-A.; Simmer, J. P.; Margolis, H. C.; Beniash, E. Amelogenin-Collagen Interactions Regulate Calcium Phosphate Mineralization in Vitro. *J. Biol. Chem.* **2010**, 285, 19277-19287.

190. Dey, A.; Bomans, P. H.; Müller, F. A.; Will, J.; Frederik, P. M.; de With, G.; Sommerdijk, N. A. The Role of Prenucleation Clusters in Surface-Induced Calcium Phosphate Crystallization. *Nat. Mater.* **2010**, 9, 1010-1014.

191. Fang, P.-A.; Conway, J. F.; Margolis, H. C.; Simmer, J. P.; Beniash, E. Hierarchical Self-Assembly of Amelogenin and the Regulation of Biomineralization at the Nanoscale. *Proc. Natl. Acad. Sci. U.S.A.* **2011**, 108, 14097-14102.

192. Vidavsky, N.; Addadi, S.; Mahamid, J.; Shimoni, E.; Ben-Ezra, D.; Shpigel, M.; Weiner, S.; Addadi, L. Initial Stages of Calcium Uptake and Mineral Deposition in Sea Urchin Embryos. *Proc. Natl. Acad. Sci. U.S.A.* **2014**, 111, 39-44.

193. Gower, L. B. Biomimetic Model Systems for Investigating the Amorphous Precursor Pathway and Its Role in Biomineralization. *Chem. Rev.* **2008**, 108, 4551-4627.

194. Liu, Y.; Kim, Y. K.; Dai, L.; Li, N.; Khan, S. O.; Pashley, D. H.; Tay, F. R. Hierarchical and Non-Hierarchical Mineralisation of Collagen. *Biomaterials* **2011**, 32, 1291-1300.

195. Jung, H. Y.; Chun, H.; Park, S.; Kang, S. H.; Ahn, C. W.; Kwon, Y. K.; Upmanyu, M.; Ajayan, P. M.; Jung, Y. J. Liquid Metal Nanodroplet Dynamics inside Nanocontainers. *Sci. Rep.* **2013**, 3, 1-5.

196. Jose-Yacaman, M.; Gutierrez-Wing, C.; Miki, M.; Yang, D. Q.; Piyakis, K. N.; Sacher, E. Surface Diffusion and Coalescence of Mobile Metal Nanoparticles. *J. Phys. Chem. B* **2005**, 109, 9703-9711.

197. Johnston, J. C.; Molinero, V. Crystallization, Melting, and Structure of Water Nanoparticles at Atmospherically Relevant Temperatures. *J. Am. Chem. Soc.* **2012**, 134, 6650-6659.

198. Billinge, S. Materials Science Nanoparticle Structures Served up on a Tray. *Nature* **2013**, 495, 453-454.

199. Franz, D.; Runte, S.; Busse, C.; Schumacher, S.; Gerber, T.; Michely, T.; Mantilla, M.; Kilic, V.; Zegenhagen, J.; Stierle, A. Atomic Structure and Crystalline Order of Graphene-Supported Ir Nanoparticle Lattices. *Phys. Rev. Lett.* **2013**, 110.

200. Park, Y.; Choi, J. S.; Choi, T.; Lee, M. J.; Jia, Q.; Park, M.; Lee, H.; Park, B. H. Configuration of Ripple Domains and Their Topological Defects Formed under Local Mechanical Stress on Hexagonal Monolayer Graphene. *Sci Rep-Uk* **2015**, 5.

201. Zhang, Z. P.; Zhang, J.; Chen, N.; Qu, L. T. Graphene Quantum Dots: An Emerging Material for Energy-Related Applications and Beyond. *Energ Environ Sci* **2012**, 5, 8869-8890.